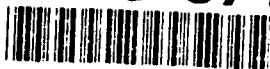


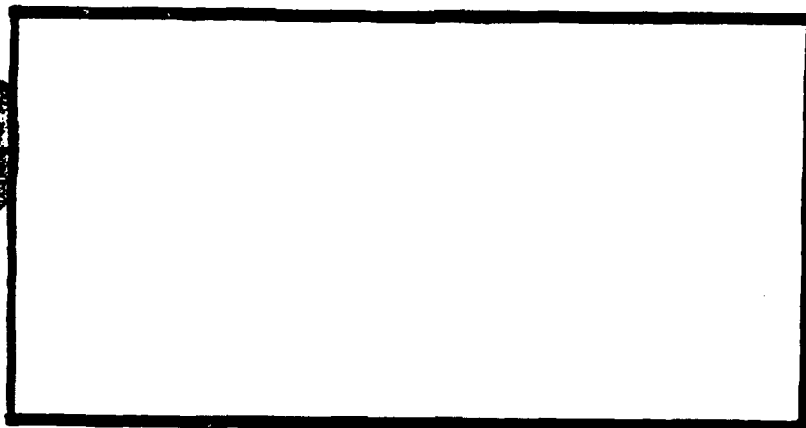
AD-A243 871



4



DTIC
ELECTE
JAN 06 1992
S D



92-00192



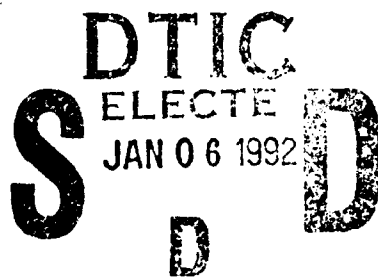
This document has been approved
for public release and sale; its
distribution is unlimited.

DEPARTMENT OF THE AIR FORCE
AIR UNIVERSITY
AIR FORCE INSTITUTE OF TECHNOLOGY

Wright-Patterson Air Force Base, Ohio

AFIT/GAE/ENY/91D-21

1



THERMOMECHANICAL FATIGUE
CHARACTERIZATION OF AN ANGLE PLY
METAL MATRIX COMPOSITE

THESIS

Wade H. Vaught, First Lieutenant, USAF

AFIT/GAE/ENY/91D-21

Approved for public release; distribution unlimited

AFIT/GAE/ENY/91D-21

**THERMOMECHANICAL FATIGUE CHARACTERIZATION OF AN ANGLE PLY
METAL MATRIX COMPOSITE**

THESIS

**Presented to the Faculty of the School of Engineering
of the Air Force Institute of Technology**

Air University

**In Partial Fulfillment of the
Requirements for the Degree of
Master of Science in Aeronautical Engineering**

**Wade H. Vaught, B.S.
First Lieutenant, USAF**

December 1991

Accession For	
NTIS CRA&I	<input checked="" type="checkbox"/>
DTIC TAB	<input type="checkbox"/>
Unannounced	<input type="checkbox"/>
Justification	
By	
Distribution	
Availability	
Dist	
A-1	

Approved for public release; distribution unlimited

Preface

The intended purpose of this investigation was to fully characterize the fatigue response of a $[\pm 45]_2$ angle ply SCS-6/TI-15-3 metal matrix composite laminate due to in-phase and out-of-phase thermomechanical fatigue and isothermal fatigue. However, due to the numerous difficulties to be expected during an experimental study, only the in-phase characterization was completed. These other areas not investigated should be pursued to continue the interesting research performed thus far.

To personally thank everyone by name who was involved in the experimentation and thesis preparation is not possible on a single page. Let it be said that many very talented people both at AFIT and at the Materials Laboratory were involved with this thesis. In particular, I would like to thank Mark Derriso, Brian Sanders and Bob Lewis for their patience and invaluable assistance. Also, I wish to thank Karen for her love and support throughout this program and especially over the last six months. Finally, I wish to thank my thesis advisor, Dr. Shankar Mall, for his timely guidance and assistance from beginning to end.

Wade H. Vaught

Table of Contents

	Page
Preface	ii
List of Figures	v
List of Tables	viii
Abstract	ix
I. Introduction	1
II. Background	10
General	10
Recent Advances in Metal Matrix Composite Testing	12
Damage in Metal Matrix Composites	16
Metal Matrix Composite Modeling - AGLPLY	21
III. Equipment and Test Procedures	25
Test Material	25
Specimen Preparation	26
Test Conditions	26
Test Equipment	28
Computer Control System	30
Load and Displacement Components	32
Thermal Control Components	33
Test Procedures	37
IV. Results	42
Test Results Summary	42
Strain Measurements	47
Isothermal Fatigue Test	47
Thermomechanical Fatigue Tests	48
Modulii Measurements	61
Isothermal Fatigue Test	63
Thermomechanical Fatigue Tests	65
Damage Analysis	71
Isothermal Fatigue Test	73
Thermomechanical Fatigue Tests	77

	Page
Edge Replicating	77
Fracture Analysis	82
Composite Microstructure	94
V. Discussion and Analysis	99
Stiffness Analysis	102
Fatigue Life	107
VI. Conclusions and Recommendations	110
Appendix A: Logarithmic Modulii Plots	113
Appendix B: WDS Analysis	117
Bibliography.	118
Vita.	121

List of Figures

Figure		Page
1.	Typical SCS-6 Fiber	2
2.	Typical Stress-Strain Curve for a $[\pm 45]_{2s}$ Laminate	5
3.	Triaxial State of Stress at the Fiber-Matrix Interface	6
4.	AGLPLY Fiber-Matrix Model	22
5.	Typical Specimen Edge Before Testing	27
6.	Ideal Load and Temperature Profiles	28
7.	Experimental Test Set-Up	31
8.	Mounted Test Specimen	33
9.	Actual Test Cycle Data	36
10.	Test Specimen Configuration	38
11.	In-Phase Fatigue Life	44
12.	Fatigue Stress Range vs. Total Failure Strain .	46
13.	Strain Data for 450 MPa Test	50
14.	Strain Data for 400 MPa Test	51
15.	Strain Data for 350 MPa Test	52
16.	Strain Data for 320 MPa Test	53
17.	Strain Data for 220 MPa Test	54
18.	450 MPa Strain Progression	56
19.	400 MPa Strain Progression	57
20.	350 MPa Strain Progression	58

Figure		Page
21.	320 MPa Strain Progression	59
22.	220 MPa Strain Progression	60
23.	Idealized Schematic of a Typical Stress-Strain Curve	62
24.	Stress-Strain Data for IF Test Specimen	64
25.	Modulii for 450 MPa Test	66
26.	Modulii for 400 MPa Test	67
27.	Modulii for 350 MPa Test	68
28.	Modulii for 320 MPa Test	69
29.	Modulii for 220 MPa Test	70
30.	Schematic of Sectioned Specimen	72
31.	X-Ray from IF Test Specimen	74
32.	Face Section of the IF Test Specimen	75
33.	Matrix Cracking in the IF Test Specimen	76
34.	Intersecting Slip Bands in the IF Test Specimen	77
35.	Ductile Fracture Surface of the IF Test Specimen	78
36.	Edge Replica with Debonded Fibers	79
37.	Edge Replica with Recessed Fibers in a Ply	80
38.	Edge Replica with Transverse Matrix Cracking	81
39.	Edge Replica with Longitudinal Matrix Cracking	82
40.	Degraded Reaction Zone	84
41.	Typical Transverse Matrix Cracking	85
42.	Typical Transverse Matrix Cracks Emanating from Damaged Reaction Zones	86

Figure		Page
43.	Typical Longitudinal Matrix Cracking along a Ply Boundary	87
44.	Typical Fiber Cracking	88
45.	Typical Matrix Necking along Debonded Fibers .	89
46.	Intersecting Slip Bands within a Grain from the 350 MPa Test Specimen	90
47.	Slip Bands from the 320 MPa Test Specimen . . .	91
48.	Typical Ductile Fracture Surfaces from the 450 MPa and 400 MPa Test Specimens	92
49.	Typical Cleavage Fracture Surfaces from the 450 MPa and 320 MPa Test Specimens	93
50.	Fracture Surface with Mixed Brittle and Ductile Failure Regions	94
51.	Matrix Microstructure after TMF Testing	96
52.	Matrix Microstructure after Heat Treatment and after Thermal Cycling	98
53.	Fatigue Life Comparison between TMF Test and IF Test	108
54.	Modulii with Logarithmic Cycle Axis for 400 MPa Test	113
55.	Modulii with Logarithmic Cycle Axis for 350 MPa Test	114
56.	Modulii with Logarithmic Cycle Axis for 320 MPa Test	115
57.	Modulii with Logarithmic Cycle Axis for 220 MPa Test	116
58.	WDS Analysis of Uncycled Ti-15-3	117

List of Tables

Table		Page
1	Constituent Properties of SCS-6/Ti-15-3	4
2	Test Matrix	29
3	Specimen Properties	43
4	Isothermal Fatigue Test Mechanical Strains . .	48
5	Failure Strain Summary	49
6	Isothermal Fatigue Cycle Modulii	63
7	AGLPLY Predicted Modulus Change	104

Abstract

An investigation was conducted to study the thermomechanical fatigue (TMF) response of a $[\pm 45]_2$ angle ply SCS-6/TI-15-3 metal matrix composite (MMC). Load controlled in-phase TMF experiments were performed over the temperature range 149-427 C, with a cycle frequency of .02 Hz. Test equipment included a high temperature extensometer, quartz lamp radiative heaters controlled by a Micricon thermal control unit and TMF test control software, MATE263. Stress and strain hysteresis, total strain and stiffness were monitored to characterize material behavior. Large plastic deformations were observed in all specimens, with total failure strains ranging from 7 to 13 percent. It was observed that the total strain to failure was proportional to the maximum applied cycle stress. Damage mechanisms, studied using edge replication and optical and scanning electron microscopy, showed transverse microcracks originating at the fiber-matrix interface and slip bands and fiber sliding in the matrix. Three phases during fatigue life were observed in the tested specimens: 1) interface damage, 2) matrix hardening and 3) matrix damage. Cold working of the matrix was a probable factor in the matrix hardening. The fibers did not affect the fatigue behavior which was dominated by matrix response.

THERMOMECHANICAL FATIGUE CHARACTERIZATION OF AN ANGLE PLY METAL MATRIX COMPOSITE

I. Introduction

Metal matrix composites (MMCs) are being considered for high temperature applications where the need for a high strength, low density material is paramount. Projects such as the National Aerospace Plane (NASP), Advanced Tactical Fighter (ATF) and the Integrated High Performance Turbine Engine Technologies (IHPTET) program would all directly benefit from the development of such a material.

These potential applications require a material capable of enduring repeated mechanical and thermal cycling (8:1). Titanium-alloy matrix composites reinforced with continuous silicon carbide fibers are being developed to meet these requirements. Although titanium alloys are not usually considered for high temperature applications, these matrix systems are thought to possess some characteristics required in future high temperature materials (13:1). Such titanium metal matrix composites would offer better resistance to thermal and oxidation effects at elevated temperatures than conventional monolithic engineering metals (21:1).

A material system considered a forerunner of more advanced titanium-based metal matrix composites is SCS-6/Ti-15V-3Cr-3Al-3Sn (commonly referred to as Ti-15-3) (20:2).

Ti-15-3 is a metastable beta strip alloy which is weldable, ageable and resistant to corrosive environments (24:1), though susceptible to oxidation effects at high temperatures (20:2). The SiC fiber in this study is a complex, multilayered structure. It is 142 μm in diameter and consists of a carbon monofilament core, surrounded by silicon carbide with a 3 μm double pass carbon coating on the outer surface (13:4-5). The industry designator for this fiber is SCS-6. Figure 1 shows a typical SCS-6 fiber from a $[\pm 45]$ laminate.

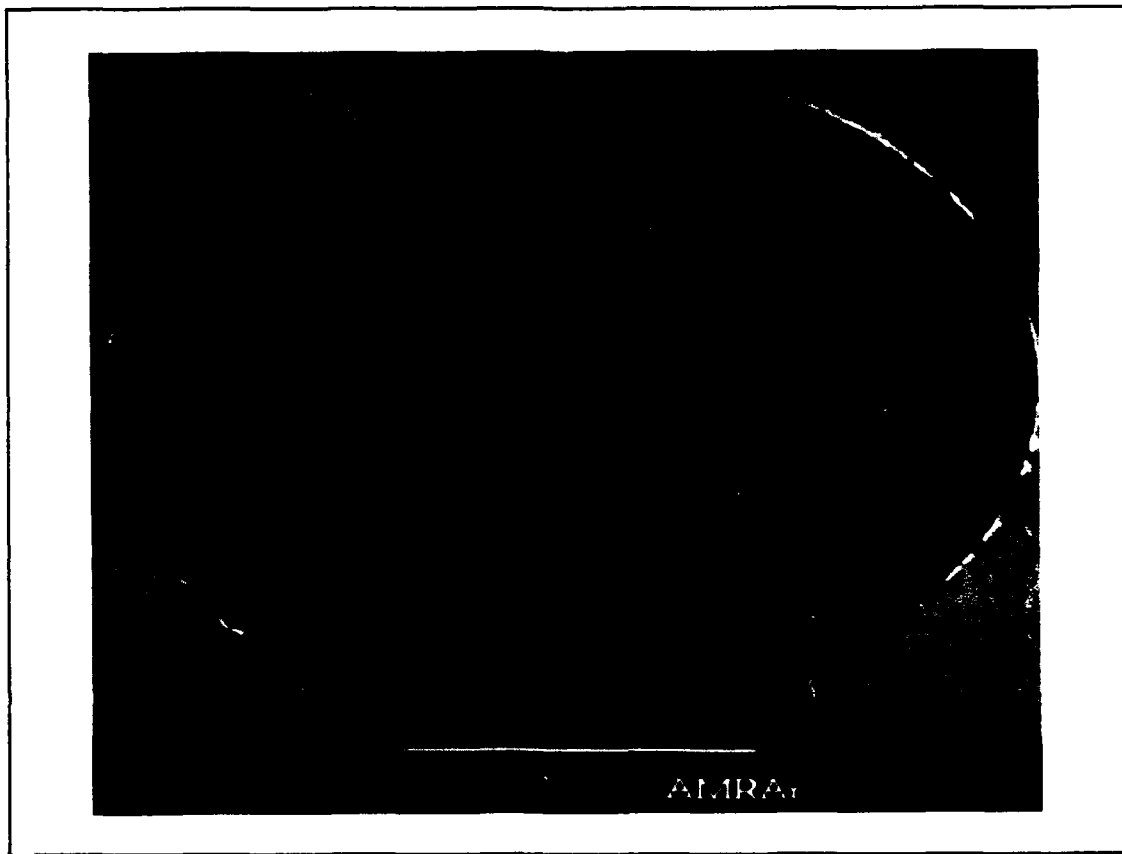


Figure 1. Typical SCS-6 Fiber

Although Ti-15-3 is a model alloy for more advanced composites, fully characterizing it is the important first step in developing more advanced matrix systems for use in the advanced aerospace applications mentioned earlier. Much research has been completed on the SCS-6/Ti-15-3 system. Previous efforts consisted of characterizing the physical metallurgy of the composite, characterizing tensile behavior at ambient and elevated temperatures and investigating damage due to thermal, isothermal and thermomechanical fatigue. This study continues the research in this direction by investigating thermomechanical fatigue in a $[\pm 45]$ angle ply laminate.

Characterization of titanium-based metal matrix composites exposed to high temperature static and cyclic loading is important because of the unique response such composites exhibit in high temperature environments and their likely operational requirements. Predicted temperatures of structural components of the NASP exceed 1100 C (26:1), which is well into the creep range of the titanium matrix (21:2). The cause of the complex thermal and mechanical response of any metal matrix composite is attributed to the use of two distinctly different fiber and matrix materials. Table 1 lists room temperature mechanical properties for the SCS-6/Ti-15-3 fiber and matrix materials (6:33-7). These varying properties are commonly combined according to simple rules of mixture to give overall laminate properties.

Table 1. Constituent Properties of SCS-6/Ti-15-3

<u>Property</u>	<u>Fiber</u>	<u>Matrix</u>
E (GPa)	427	60-100
G (GPa)	179	22.7-37.8
ν	.19	.32
ρ (gm/cc)	2.99	4.76
α ($^{\circ}\text{C}^{-1}$)	4.9×10^{-6}	8.5×10^{-6}

Due to the mismatch in coefficient of thermal expansion (CTE), the fiber and matrix will expand and contract at different rates when exposed to temperature changes. Thus, mechanical strains can be induced in a metal matrix composite merely by varying temperature. This unique thermal response coupled with different strengths and failure modes in the fiber, matrix and fiber-matrix interface create very complex material behavior in thermal and mechanical fatigue. Added to this complexity is the effect of matrix and fiber-matrix interface damage experienced during cycling on the laminate properties.

A unique characteristic of titanium-based metal matrix composites containing off-axis plies (plies with fibers oriented other than zero degrees) is the bi-linear stress-strain response (10:203). Figure 2 shows this bi-linear region in a typical stress-strain curve for a $[\pm 45]_2$ SCS-6/Ti-15-3 laminate.

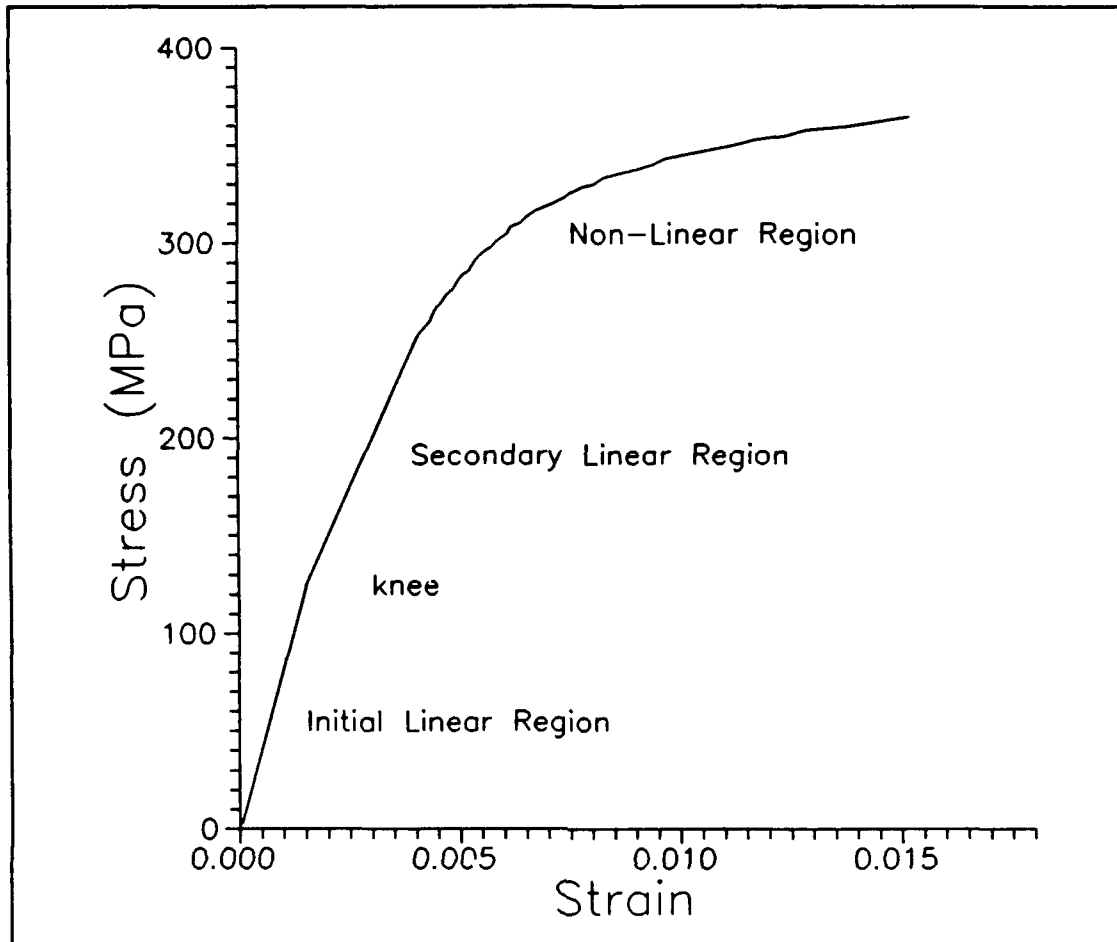


Figure 2. Typical Stress-Strain Curve for $[\pm 45]_{2s}$ Laminate

The "knee" between linear regions, shown in Figure 2, occurs well below the matrix yield stress of 690 MPa (10:204).

Johnson has shown that the knee corresponds to fiber-matrix separation due to releasing of residual stresses in the matrix around the fiber formed during composite processing (10:205). These residual stresses arise due to the coefficient of thermal expansion mismatch mentioned earlier.

Large compressive radial stresses build up at the fiber-matrix interface during cooldown from processing

temperature, while the axial and tangential components of the residual stress remain tensile; thus, the matrix is effectively choking the fiber (23:400). Figure 3 shows the triaxial state of stress at the fiber-matrix interface.

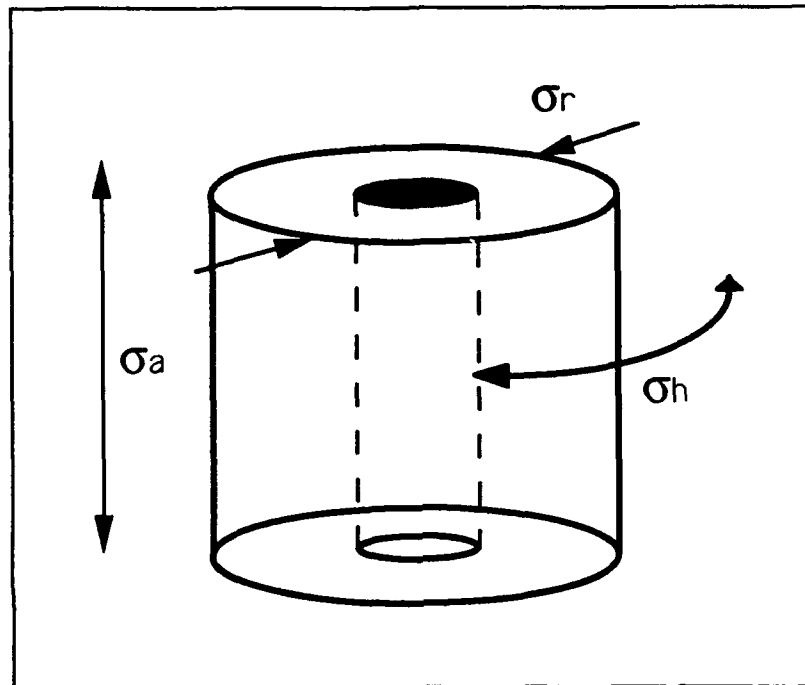


Figure 3. Triaxial State of Stress at the Fiber-Matrix Interface

This triaxial state of stress results in yielding or near yielding in the matrix adjacent to the fiber-matrix interface (19:1).

Hence, the knee is thought to correspond to the applied stress required to overcome the residual stresses and the strength of the fiber-matrix bond. The residual stresses, however, are recovered during unloading. The net result is a continuous opening and closing of the fiber-matrix interface during cyclic loading. The effect continues even after

interface failure since the compressive radial stress and tensile tangential stress will cause the matrix and fiber to recontact upon unloading (10:205).

Obviously, the fiber-matrix bond and interface zone are major factors in understanding the mechanical behavior in titanium-based metal matrix composites. Johnson has shown the bond between the SiC fiber and Ti-15-3 matrix to be weak and that a stronger bond is required in titanium-based matrix composites than in aluminum-based matrix composites. A stronger bond is needed since the titanium matrix is stronger and better able to transfer load to off-axis fibers (9:19).

Adding to the complexity of the fiber-matrix interface is the presence of a reaction zone created during consolidation when the fiber coating reacts with the matrix. In Figure 1, the reaction zone at the fiber-matrix interface can be seen. Lerch has investigated the microstructure of as-received SCS-6/Ti-15-3 in detail in Reference 13. This reaction product transfers load from the matrix to the fiber. The quality of the bond between the reaction zone and the fiber and the matrix ultimately determines the properties of the composite (13:9-10). The primary constituents of the reaction zone are small crystallites of TiC. The outlying portion of the reaction zone is composed of fine equiaxed grains which could pose problems at high temperatures. Small grains permit higher creep rates and additional paths for oxygen diffusion and embrittling of the

interface. This weakened area, coupled with a state of stress at or near yielding, make the interface the weak link in the composite (13:1).

The microscopic and macroscopic effects of heat treatment on Ti-15-3 have been investigated by Lerch and others (15). Their findings include the formation of a thick surface oxide layer at temperatures above 550 C and variation of elastic modulus, ultimate tensile strength and ductility with aging treatment (15:1). The Ti-15-3 system is very sensitive to thermal effects since it is not stable.

These general characteristics of the titanium-based metal matrix composites make predicting and modeling of composite behavior impossible without empirical support. This is especially true for the fatigue properties of such composites. Therefore, characterization of damage modes and failure prediction under various fatigue conditions requires experimental investigation.

Future aerospace vehicles incorporating metal matrix composites as structural materials will experience a wide range of operational temperatures and loading conditions. The need exists, then, to fully characterize and understand the thermomechanical fatigue (TMF) response of titanium-matrix composites such as SCS-6/Ti-15-3. No study has been reported to investigate the [± 45] angle ply laminate under thermomechanical fatigue conditions.

This study addresses the in-phase thermomechanical response of a [± 45]₂, SCS-6/Ti-15-3 laminate. The test

techniques used were identical to that used by Schubbe (26) in a similar thermomechanical fatigue investigation. Stress and strain hysteresis, total strains and stiffness measurements were recorded during testing for analysis, and damage progression was also monitored during testing using edge replica techniques. Fractography and scanning electron microscope analysis allowed examination of damage and reaction zones in failed specimens.

II. BACKGROUND

General

Thermomechanical fatigue (TMF) involves cycling both mechanical loads and temperature in a well controlled manner, while minimizing temperature gradients through the test section. Usually the load and temperature are programmed to follow a specific profile such as triangular, sinusoidal or square, with a fixed phase relation between the two.

In-phase thermomechanical fatigue requires the maximum mechanical load to occur at the same instant as the maximum temperature. Out-of-phase thermomechanical fatigue exhibits the opposite relation between load and temperature. Another more complicated cycle is the faithful cycle. This involves subjecting the specimen to a strain-time and temperature-time history that faithfully duplicates the actual cycle for a structural component. In-phase and out-of-phase cycling, however, are more simple and more useful when characterizing general material response under thermomechanical fatigue (7:28). Halford (7) provides an excellent review of thermal and thermomechanical fatigue test techniques.

The most critical aspect of thermomechanical fatigue testing is the synchronization of temperature and load phase angles. Improper phasing can cause distorted hysteresis loops and make analysis of test data difficult (2:3). For load-controlled TMF testing, continuous adjustments to the

phase angle are often required. Control over the phase angle requires two major test components: a mechanical holder/loading mechanism and a temperature control system. Castelli and others (2) achieved control of these subtle phase shifts by prematurely reversing the temperature command so the temperature profile would reverse simultaneously with the mechanical load during cycling (2:1-2). Alternatively, the load can be held or advanced to the appropriate time in the TMF cycle, without interrupting the stable temperature profile, to achieve the desired synchronization between phase angles. This is the method employed in this study.

Obviously, two other important components are the heat source and displacement measurement system. To minimize temperature gradients in the specimen during testing, effective and uniform heat transfer must be accomplished. To achieve this, there are five basic heating methods: 1) hot gas flow, 2) fluidized bed, 3) radiation, 4) resistance heating and 5) radio frequency induction (7:24). Hot gas flow was probably the first method employed for thermal fatigue testing and is still used. It involves alternate impingement of hot combustion gases from a high velocity nozzle and cold compressed air. In the late 1950's, a technique was developed wherein specimens were alternately immersed in hot and cold fluidized beds. Rapid heat transfer was achieved using this technique (7:24). Radiation heating involves high intensity quartz lamps and cold

compressed air; this is the technique used in this study. Two methods of resistance heating are currently in use. The first uses a molybdenum rod coiled around cylindrical specimens; the second method passes high electric current directly through a metallic specimen (26:10). Lastly, high and low frequency induction is commonly used in isothermal and TMF studies (5:25).

Various high temperature displacement measurement techniques have been employed for elevated temperature testing. These include laser extensometers, a high temperature extensometer and a strain gauge type extensometer which uses ceramic probes to isolate it from the heat zone (26:12). In this study, a high temperature extensometer was employed to measure displacement.

Recent Advances in Metal Matrix Composite Testing

Extensive testing of static strengths and mechanical properties of the SCS-6/Ti-15-3 system have been conducted. Zero and 90 degree laminates have been the focus of much of the research, to include ambient and elevated tensile tests, isothermal fatigue tests, thermal fatigue tests and limited thermomechanical fatigue tests. In addition, many of these tests were repeated in a vacuum environment to isolate oxidation effects. As yet, comparatively few studies have been reported to characterize the $[\pm 45]$ layup as thoroughly as 0 and 90 degree laminates. Lerch and Saltsman (17) investigated the tensile deformation damage in various

layups of a Ti-15-3 laminate, including $[\pm 45]_{2s}$ specimens which were heat treated for 24 hours at 700 C in vacuum and pulled in tension to failure at room temperature and 427 C. The $[\pm 45]_{2s}$ laminate exhibited a difference in tensile behavior at 427 C when compared to room temperature, unlike the other tested layups. The laminate was less stiff and weaker and failed at a strain greater than seven percent. In addition, some strain rate dependent behavior was noted in the stress-strain curve and believed to be a consequence of dynamic strain aging. Room temperature fracture was characterized by extensive fiber cracking and debonding and no matrix cracking below the first fiber row. Elevated temperature fracture was characterized by several different damage modes. Fibers were extensively cracked, even far from the fracture surface. Large gaps in the matrix between fibers associated with debonding were present, along with extensive matrix cracking and necking between fibers. Slip bands were also observed in the matrix.

Lerch (14) has also conducted isothermal fatigue tests at 427 C of a $[\pm 45]_{2s}$ Ti-15-3 laminate in laboratory air and in vacuum. Stress and strain hysteresis loops remained open during testing, indicating non-reversible deformation. Specimens also ratcheted to failure, achieving strains up to two percent. At low stress ranges, strain ratchetting decreased at higher cycle numbers, resulting in higher strains at failure for higher stress ranges. The maximum and minimum strains grew rapidly in the first few cycles,

then continued to grow to failure at a slower rate. Fractographs revealed a difference in surface morphology between specimens tested at low stress ranges and high stress ranges. At low stress ranges the fracture surface was smooth and the fatigue crack encompassed almost the entire fracture surface. At high stress ranges the fracture surface was rougher and contained more fiber pullout. Tensile overload failure in the matrix was also observed. The damage involved both matrix and fiber cracking and interfacial debonding.

Johnson and others (8) investigated the fatigue response of several Ti-15-3 laminates at room temperature and at 650 C. Though the $[\pm 45]_2$ layup was not included, the study characterized $[0/\pm 45/90/]$, and $[0_2/\pm 45]$, laminates. Damage initiated at the fiber-matrix interface in off-axis plies which resulted in stiffness loss early in the fatigue life. Fatigue life was shown to be a function of the stress in the 0 degree fibers both at room and elevated temperatures.

Several tests have been conducted to quantify the effects of thermal cycling on the Ti-15-3 system, though none directly for the $[\pm 45]_2$ laminate. MacKay observed internal damage concentrated near fiber-matrix interfaces in a unidirectional specimen thermally cycled between 300 C and 550 C (18:170). Ermer found similar damage over the temperature ranges of 149 C - 427 C and 149 C - 649 C (3:59). Majumdar and Newaz observed interfacial debonding and

delamination in a quasi-isotropic laminate cycled in a vacuum-like environment between 315 C and 649 C (20:12). Schubbe noted longitudinal edge cracking in a cross-ply laminate after 10,000 thermal cycles over the range of 149 C to 649 C (26:55). All of these investigations reported no loss of strength or stiffness due to thermal cycling.

Load-controlled thermomechanical fatigue and isothermal fatigue tests were conducted by Majumdar and Newaz (20) on a quasi-isotropic ($[0/\pm 45/90]_s$) layup of SCS-6/Ti-15-3. In-phase TMF tests were conducted over a 315 C - 650 C temperature range in a sealed argon environment to reduce oxidation effects. The total strain range stabilized to a constant value within a short number of cycles and provided good correlation with thermomechanical fatigue life. Thermomechanical fatigue specimens showed significant delamination cracking between plies oriented parallel to the loading axis and transverse microcracking originating from the reaction zone or fiber-matrix interface. Major microcracks seemed to initiate at the fiber-matrix interface of off-axis plies.

Schubbe (26) conducted in-phase and out-of-phase thermomechanical fatigue tests on a Ti-15-3 cross-ply laminate over a 149 C - 427 C temperature range. The fatigue damage threshold limit correlated with the off-axis matrix stress independent of frequency, temperature or phasing conditions. The fiber-matrix interface was a major factor in fatigue initiation and progression. The primary fatigue damage

mechanism was transverse cracking originating in the 90 degree ply reaction zones growing outward to the surface. The instantaneous secant modulus was effectively used as a consistent damage parameter in fatigue life predictions.

Damage in Metal Matrix Composites

Johnson (9) describes how fatigue damage can initiate and grow in various metal matrix composites, including the Ti-15-3 system. Depending on the relative fatigue behavior of the fiber and matrix and the interfacial properties, damage can be categorized as matrix dominated, fiber dominated, self-similar or fiber-matrix interface dominated. Matrix dominated damage was found in boron/aluminum composites in which the fibers are very fatigue resistant and virtually elastic until fracture and the matrix yields at a relatively low strain (.1 - .2 percent). Under cyclic loading, the matrix continuously yields while the fiber is unaffected. Fatigue damage accumulates in the matrix but not in the fibers; hence, the damage is matrix dominated. A $[\pm 45]_{2s}$ SCS-2/Al specimen fatigued below the shakedown stress range experienced large plastic deformation (up to eight percent), a fourfold increase in yield stress and an increase in elastic and secant modulus due to fiber rotation. Below the shakedown stress range, no significant fatigue damage was noticed. Above the shakedown stress range, the laminate experienced fiber rotation and matrix cracking which grew to failure since there were no 0 degree

fibers to which the load from the damaged matrix could be transferred. The shakedown stress range was used as an estimate of the fatigue limit in laminates containing no 0 degree fibers. In composite systems with relatively weak, small fibers and a strong fiber-matrix interface, fiber dominated fatigue cracking can occur. Cracks propagating across fibers give a flat fracture surface in fiber-dominated failure. Conversely, large, strong fibers have better crack resistance and tend to deflect cracks along the interface, thus giving a very erratic crack path. It is noted that in the SCS-6/Ti-5-13 system fiber failure is not the first fatigue damage to occur, but is preceded by failure of the fiber-matrix interface in off-axis plies. Self-similar fatigue damage has been observed in titanium-based metal matrix composites, including the Ti-15-3 system. When fatigue endurance strain ranges for the fiber and matrix are nearly equal, crack growth can be self-similar as in homogeneous materials. This type of damage requires a high strength matrix (such as titanium) capable of creating a high stress concentration in fibers across the interface and a strong interface to transfer crack tip strains from the matrix. Fiber-matrix interface failures are common in laminates with a high strength matrix material and off-axis plies. Interfaces tend to fail if they are weaker than the transverse strength of the fiber and matrix. Interface damage occurring in off-axis plies can significantly reduce laminate stiffness during the first fatigue cycle. Fiber-

matrix interfaces in the Ti-15-3 system are known to be weak and such failures in off-axis plies manifest themselves in the bi-linear stress-strain response discussed earlier.

Majumdar and Newaz (19) have attempted to quantify the inelastic deformation mechanisms in a 90° SCS-6/Ti-15-3 laminate during cyclic loading by evaluating the loading-unloading response, monitoring Poisson's ratio and through post-test optical microscopy. Specifically, the authors attempted to distinguish between plasticity and damage as the cause of deformations. One powerful method they utilized was unloading the laminate from the non-linear region and observing changes in stiffness. If plasticity was the deformation mechanism, the material would unload with the same stiffness as the loading stiffness and would experience a permanent strain offset from the origin. Conversely if deformation was due to damage alone, the unloading stiffness would be less than the loading stiffness, and there would be no accumulated plastic strain at the origin. A significant change in Poisson's ratio and the presence of slip bands in the deformed matrix are also indications of plasticity. Using these three methods, the empirical stress-strain curve of the 90 degree laminate was analyzed and categorized into three stages. In the first stage, the composite behaved essentially as a linear-elastic solid and all strain was recoverable. Stage two contained deformation dominated by damage, though slight plasticity was also present. The third stage contained both plasticity and damage mechanisms

but was dominated by plasticity. The authors also noted that the knee between the bi-linear regions occurred at a lower stress level with each successive cycle. Microscopic evaluations revealed significant fiber-matrix debonding, radial cracking in the brittle reaction zone and slip bands nucleating preferentially at reaction zone cracks. In the 90 degree laminate, the reaction zone cracks started forming at strains between .4 and .5 percent and were caused by preliminary fiber-matrix debonding occurring at .2 percent strain.

Lerch (16) has investigated in more detail the plasticity associated with damage in the Ti-15-3 system. Specimens of various fiber layups, including $[\pm 45]_{2s}$, were heat treated for 24 hours at 700 C in vacuum and tested in tension at room temperature. Heavy concentrations of slip bands were observed at matrix crack tips, near fibers and in areas of matrix necking between fibers. One unreinforced matrix specimen experienced 20 percent failure strain.

Oxidation effects on the fatigue life of a unidirectional Ti-15-3 laminate were investigated by Gayda and others (4). Isothermal and simplified out-of-phase TMF tests were conducted in vacuum and compared to similar tests in air. Specimens were heat treated at 593 C for 24 hours. The fatigue life of the composite experienced significant degradation for the thermomechanical fatigue test, which became more severe as the temperature range increased. Environmental effects were proven to reduce fatigue life

under non-isothermal conditions when maximum temperature approached 550 C; fatigue life was five times greater in vacuum than in air. The likely source of environmental degradation was rapid diffusion of oxygen through the titanium matrix and surface oxidation, the latter being more important in non-isothermal tests. Surface oxidation causes oxide spikes to form at the specimen surface and which crack under load. Enhanced surface crack initiation becomes the dominant fatigue failure mode under non-isothermal conditions.

Recently, the molybdenum crossweave has been identified as another likely source of embrittling and cracking in the matrix besides the fiber-matrix interface. The crossweave wire is woven between fibers in a ply and helps to maintain good fiber spacing and alignment. Khobaib (11) and Kortyna and Ashbaugh (12) have investigated crossweave effects on damage in intermetallic titanium-based metal matrix composites. Khobaib conducted creep tests on a unidirectional Ti-24Al-11Nb laminate in air and vacuum environments. The molybdenum crossweave oxidized over time and embrittled the matrix surrounding it. These weakened regions were associated with a stepped fracture surface. In most cases the crossweave was found to be a crack initiation site for the fiber and may have also contributed to debonding. The evidence suggested stress assisted environmental degradation of the carbon layers of the SCS-6 fiber, which may have been promoted by the molybdenum crossweave. Kortyna and Ashbaugh

conducted isothermal fatigue tests on a unidirectional Ti-24-11 laminate and observed surface edge damage in the heat zone occurring in a uniform spacing which corresponded to the crossweave spacing. Again, the molybdenum crossweave was severely oxidized and reacted with the surrounding matrix. It was observed that the molybdenum wires were compressed onto the fibers of the outermost plies during consolidation, which was thought to result in a stress concentration at each wire/fiber crossing in these plies. As a result, the crossweave sites nearest the surface edges were the locations of the earliest and most pronounced damage initiation. The crossweave provided the primary initiation sites for fatigue damage at 815 C. Newaz and Majumdar also observed fiber fracture aided by crossweave in a Ti-15-3 laminate (22:4).

Metal Matrix Composite Modeling - AGLPLY

AGLPLY is a computer code designed to perform global linear and non-linear analysis of fiber reinforced metal matrix composites. It predicts laminate properties and behavior only in an average sense. It is not designed to calculate accurately the fiber and matrix stresses, though values are predicted. Further, AGLPLY cannot model an interface layer between the fiber and matrix. Despite these limitations, AGLPLY has been shown to predict with reasonable accuracy the laminate properties and stress-strain behavior based on constituent property input (1:27).

Bigelow (1:21-22,26) summarizes the AGLPLY program and the Vanishing Fiber Diameter model upon which it is based. The AGLPLY program is based on the constituent properties of the fiber and matrix. The model assumes a regular square array of fibers, that all fibers are identical, continuous and parallel and that the bond between the fiber and matrix is perfect. Figure 4 shows the two-dimensional fiber-matrix model used in AGLPLY. While the fiber is assumed to be perfectly elastic, the matrix may have elastic-plastic properties. The material properties of both the fiber and matrix are input as a function of temperature. The interpolated

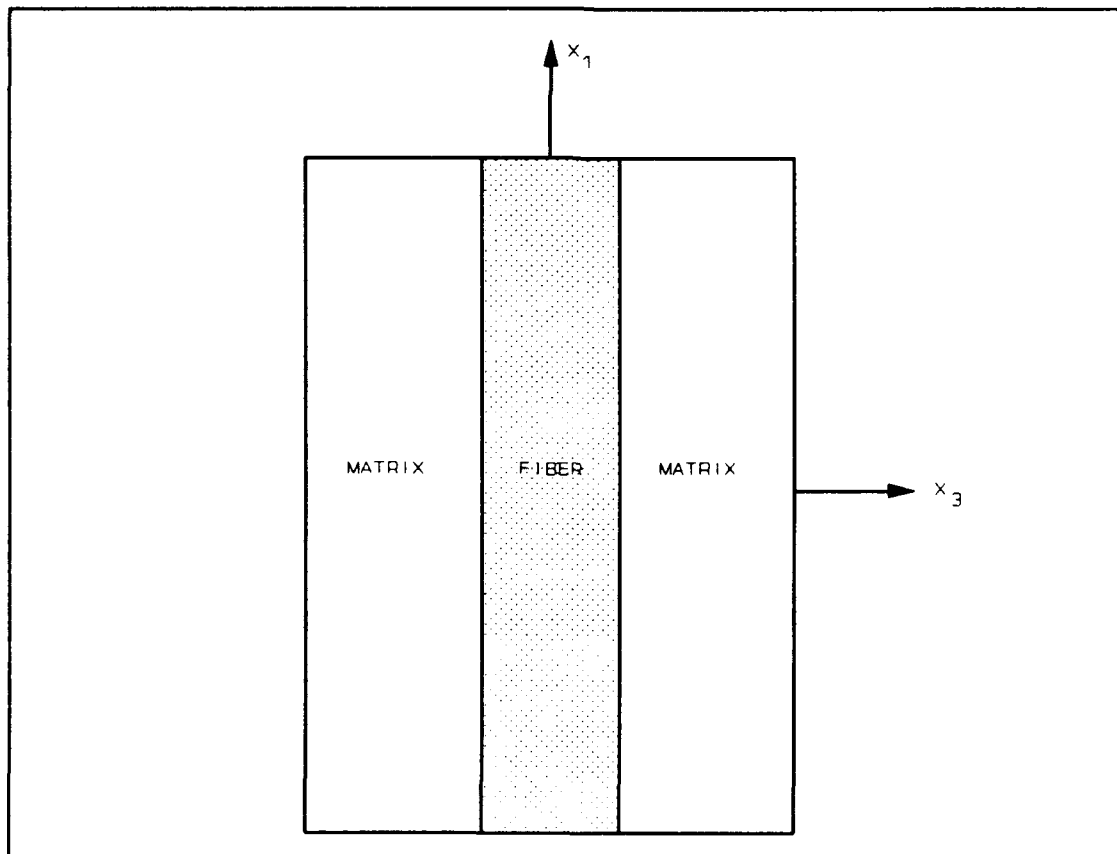


Figure 4. AGLPLY Fiber-Matrix Model

temperature-dependent response of the laminate is used to predict overall elastic laminate properties and average stresses and strains for the fiber and matrix. Any combination of in-plane loads and temperature profiles can be used for this analysis.

The Vanishing Fiber Diameter Model was first suggested by Dvorak and Bahei-El-Din as a micromechanics model for metal matrix composites. It is designed to predict average laminate properties and stress-strain behavior. It consists of an elastic-plastic matrix unidirectionally reinforced by continuous elastic fibers. The fibers are assumed to have a very small diameter such that they do not interface with matrix deformation in the transverse and thickness directions but do have an effect in the longitudinal (fiber) direction. This model imposes several requirements to satisfy the equilibrium and compatibility relations. If Cartesian coordinates are chosen with x_1 along the fiber axis, (refer to Figure 3) the overall composite stress, σ^c , can be related to the average constituent stresses. The overall stress in the fiber direction is given in Equation 1:

$$\sigma_{11}^c = V_f \sigma_{11}^f + V_m \sigma_{11}^m \quad (1)$$

where σ^c , σ^f , σ^m = axial stress in the fiber direction of the composite, fiber and matrix, respectively

V_f , V_m = volume fraction for the fiber and matrix

The remaining stress components in each constituent are assumed to be uniform and are expressed in Equation 2:

$$\sigma_{ij}^c = \sigma_{ij}^f = \sigma_{ij}^m \quad (2)$$

where $ij \neq 11$.

The only constraint in the model is that the fiber and matrix must deform equally in the x_1 (fiber) direction. This is expressed in Equation 3:

$$\epsilon_{11}^c = \epsilon_{11}^f = \epsilon_{11}^m \quad (3)$$

where, ϵ^c , ϵ^f , ϵ^m are the axial strains in the composite, fiber and matrix, respectively.

The other strain components are related to the overall strain through the tensorial relation given in Equation 4:

$$\epsilon_{ij}^c = V_f \epsilon_{ij}^f + V_m \epsilon_{ij}^m \quad (4)$$

where $ij \neq 11$.

Since this model allows for no local constraint in the matrix transverse to the fiber, it predicts only longitudinal stresses in the fiber and matrix when a unidirectional laminate is loaded along its fiber axis. Off-axis plies added to a unidirectional laminate somewhat compensate for the deficiencies in the Vanishing Fiber Diameter model by providing stiffness transverse to the fiber axis.

III. Equipment and Test Procedures

In order to characterize the effects of thermo-mechanical fatigue on a metal matrix composite angle ply laminate, rectangular tensile specimens of SCS-6/Ti-15-3 were subjected to thermomechanical cycling using test apparatus modified by Schubbe and described in detail in Reference 26. This chapter discusses the test material, test conditions, test equipment and test procedures.

Test Material

The test material in this study was a silicon carbide continuous fiber reinforced titanium metal matrix composite, designated SCS-6/Ti-15-3. The matrix material is a Ti-15V-3Al-3Sn-3Cr alloy, designated Ti-15-3, which is a β -Ti alloy with a body-centered-cubic crystal structure. The alloy is slightly metastable and α -phase precipitates when exposed to temperatures above 482 C for extended time periods (20:4). The fiber, designated SCS-6, is a beta silicon carbide monofilament produced by Textron Specialty Materials Division. The SiC is chemical vapor deposited onto a 40 μ m carbon core, and contains a double pass carbon rich outer coating designed for use with titanium based matrices (25:433). The composite is formed by hot isostatic pressing of Ti-15-3 foils between layers of SiC fibers at high temperature. A molybdenum crossweave wire is included during consolidation to ensure proper fiber alignment. All

test specimens came from a single eight ply [± 45] panel manufactured by AVCO Specialty Metals, Textron Corporation. The average plate thickness was 1.7 mm and the nominal fiber volume fraction was 35 percent. Material properties of composite constituents are given in Table 1 (see Chapter I).

Specimen Preparation. All test specimens were cut from a single panel into 165 mm by 12.7 mm rectangular specimens with a diamond cut-off wheel. Specimens were aged prior to grinding for 24 hours at 700 C in an argon vacuum environment to stabilize the α - β Ti structure. Specimen edges were ground until flat to remove irregularities and machining damage using 45 micron diamond suspension on a Maximet grinding platen. Finer grinding was continued on one edge down to the 3 or 1 micron level to provide a polished surface from which edge replicas could be taken during testing. After grinding, the specimens were visually inspected for edge damage. There was no significant damage to any specimen that could cause unwanted cracks to initiate during testing. Minor surface chipping of fibers was typical of all specimens. Figure 5 shows an optical photograph of a typical specimen after grinding and before testing.

Test Conditions

To characterize the material response to thermomechanical fatigue, five [± 45]₂ specimens were subjected to in-phase thermomechanical conditions. Tests were conducted over a 149 C - 427 C temperature range. The mechanical and

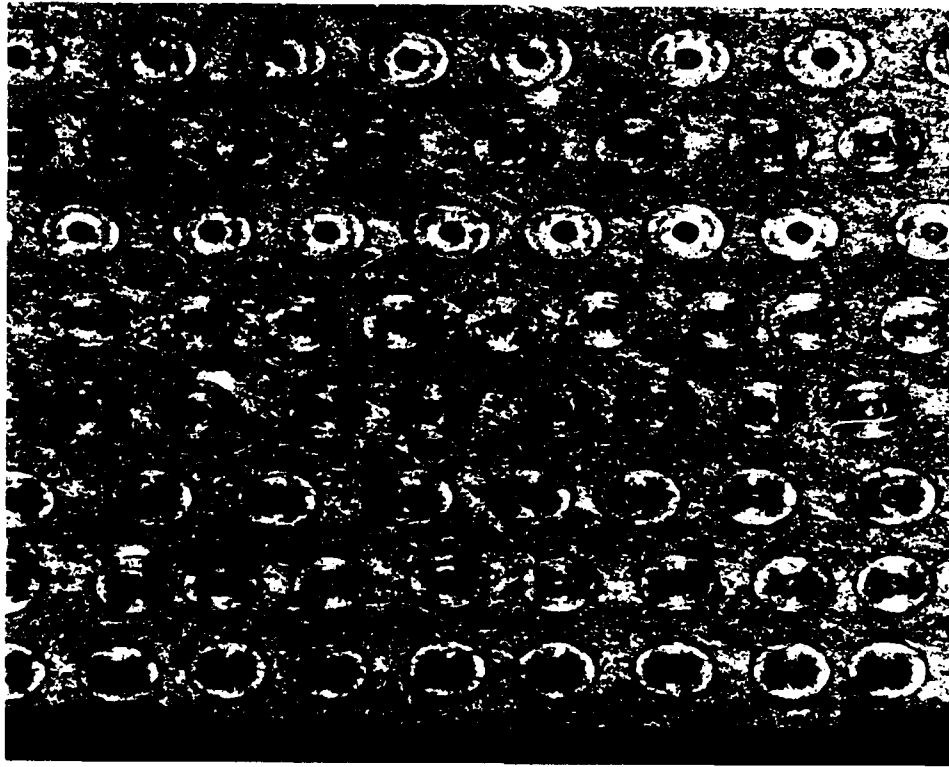


Figure 5. Typical Specimen Edge Before Testing

thermal profiles were both triangular, with the maximum applied load and maximum temperature occurring at the same time. Figure 6 illustrates ideal load and temperature profiles with no phase error. All tests were conducted under load control at minimum to maximum load ratio of 0.1 with a cycle period of 48 seconds (.021 Hz). Stress, strain and temperature data for selected cycles was recorded during testing. In addition to the TMF tests, one other specimen was mechanically cycled three times and then failed in tension at 427 C. The objective of this test was to

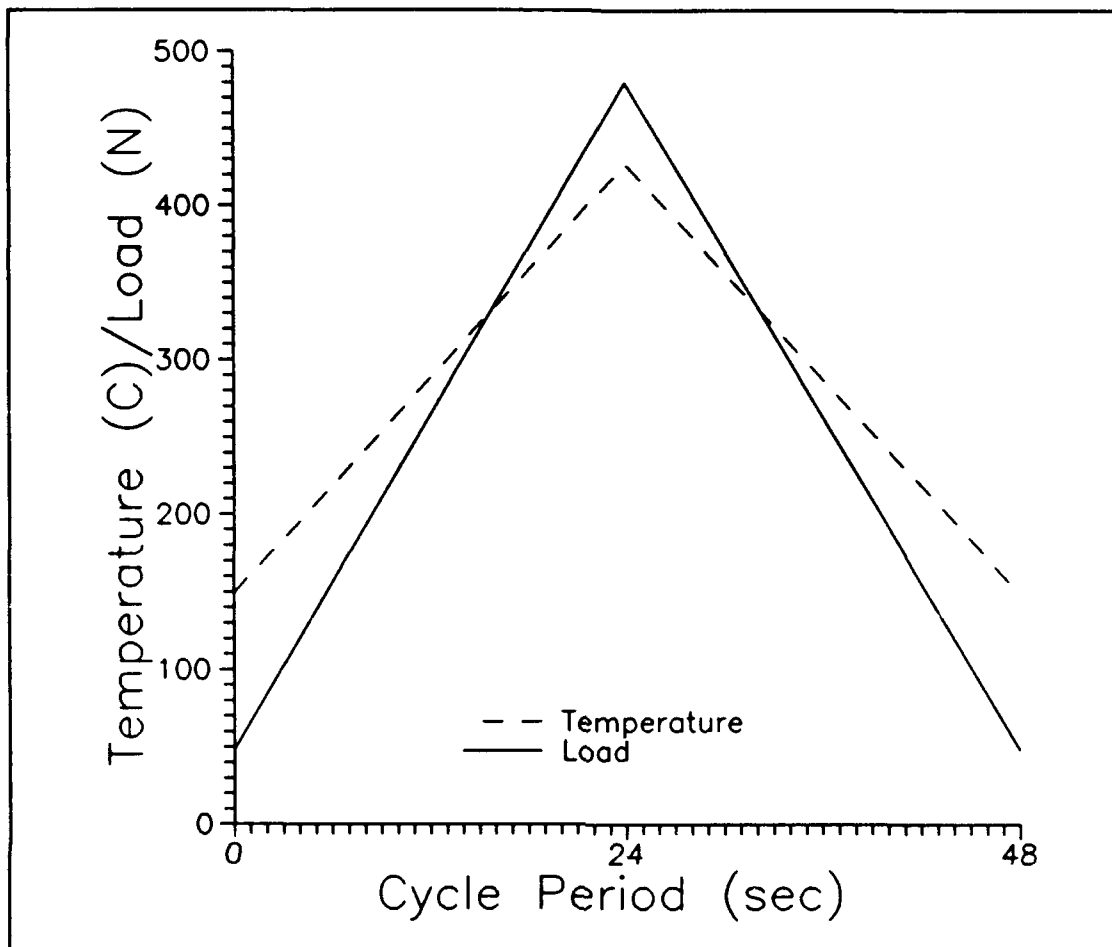


Figure 6. Ideal Load and Temperature Profiles

investigate initial stress-strain response for consecutive cycles at elevated temperature. The test matrix performed for this study is given in Table 2.

Test Equipment

The general test set-up used in this study includes six major components: 1) a 20 Kip Material Testing System (MTS) screw-driven test stand, 2) a MTS Microconsole, 3) a Wavetek waveform generator, 4) a MTS high temperature extensometer 5) a Micricon thermal control unit and 6) a Zenith 248

Table 2. Test Matrix

<u>Specimen</u>	<u>Maximum Stress</u> <u>(MPa)</u>	<u>Temperature Range</u> <u>C</u>	<u>Stress</u> <u>Ratio</u>
90 - 07*	325	427	0.05
90 - 08	450	149 - 427	0.1
90 - 05	400	149 - 427	0.1
90 - 06	350	149 - 427	0.1
90 - 10	320	149 - 427	0.2
90 - 14	220	149 - 427	0.1

* isothermal fatigue test

personal computer with data acquisition capability.

Specimens were placed in the test stand and held in tension using high temperature hydraulic grips, through which mechanical loading was applied. Load control during cycling was accomplished through the MTS Microconsole receiving commands from the test control software, MATE263, channeled through the Wavetek waveform generator. A high temperature extensometer with a gauge length of 25.4 mm was placed along the specimen edge to measure average longitudinal displacement. Thermal profiles were maintained for the specimen via two quartz lamp heaters placed on either side of the heat zone and controlled by the Micricon thermal control unit receiving feedback through thermocouples spot-welded in the heat zone. The length of the heat zone where the desired temperature gradient was controlled was 40 mm. The Micricon unit received its waveform commands as

programmed input directly from the MATE263 program. The MATE263 program managed the entire TMF test. It provided periodic updates to the Micricon unit for optimum thermal profiles and corrected phase error through input to the MTS Microconsole. Additionally, MATE263 managed data acquisition by recording test data for selected cycles and maintaining a test history log. Figure 7 shows the actual test set-up used in this study.

Computer Control System. As mentioned earlier, MATE263 run on a Zenith 248 personal computer was the test software used for overall test conduct and control. MATE263 was specifically designed for load-controlled thermomechanical fatigue testing using the test set-up described here. It was developed in 1990 by Mr. George Hartman of the University of Dayton Research Institute. The program allows for TMF testing over any range of load and temperature, with any phase relation between the two. Inputs into the program include test specific parameters such as specimen dimensions, maximum stress, load ratio, temperature range and cycle time and system specific parameters such as maximum load range and extensometer gauge length and displacement range. Once the thermomechanical cycling begins, the program simultaneously monitors temperature, load and displacement readings from the various components and calculates stress and total strain. At selected cycle intervals, stress, total strain and temperature are recorded for each data point acquired in the cycle and saved in a data file.

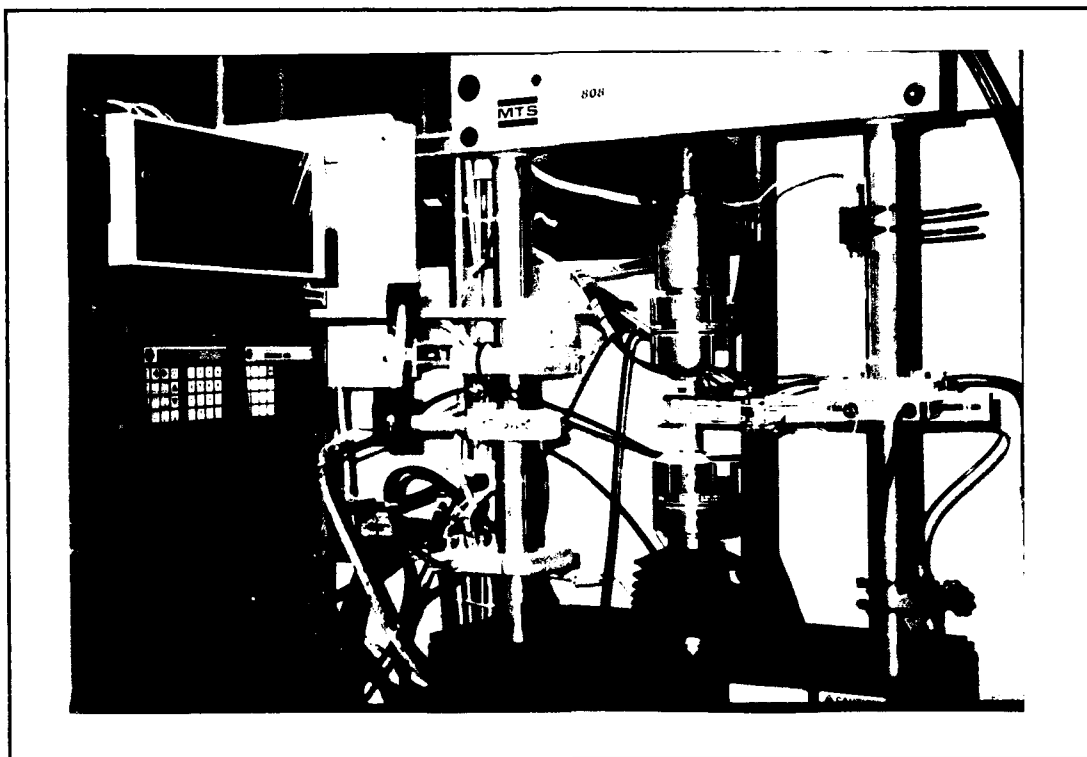


Figure 7. Experimental Test Set-Up

Each time cycle data is recorded, MATE263 updates a test history data file with data from that cycle which includes cycle count, maximum applied load, actual load ratio and maximum and minimum total strain. During each data acquisition cycle, the phase angle between selected points in the load and temperature waveforms are compared for error. If there has been any drift, the program corrects the profile by adjusting the load waveform by holding or advancing it as necessary. This method efficiently controls the phase angle between the two waveforms since the load actuator response is faster than the thermal response and it avoids upsetting a stabilized thermal profile.

Load and Displacement Components. A MTS 20 Kip model 808 screw driven test stand supported the load application during TMF cycling and was controlled by the MTS Microconsole model 485.20. The test stand was equipped with high temperature hydraulic wedge grips cooled using forced distilled water from a cooling pump. Tests were completed using a 2 Kip or 4 Kip maximum load range depending on the required maximum stress. Control commands for the load profile during cycling were sent from the MATE263 program through the waveform generator to the Microconsole.

Displacement was measured using a MTS high temperature air cooled extensometer. The extensometer measured longitudinal strains over a 25.4 mm gauge section on the edge of the specimen. The extensometer was equipped with conical tip quartz rods that were held against the specimen edge by lateral pressure from a spring-like holding mechanism; the rods were not constrained in the other degrees of freedom. Actual displacement in the specimen caused movement in the quartz rods from the static position. This displacement of the rods caused a voltage differential proportional to the axial displacement in the specimen gauge length. The displacement reading was in the form of voltages in a linear ± 10.0 volt range. Calibration of the extensometer prior to use allows the voltage output to be related to the rod displacement. The MATE263 program was given the calibration factor and gauge length which it used to calculate total strain from the extensometer output voltage. Figure 8 shows

a test specimen mounted in the grips with the extensometer in position.

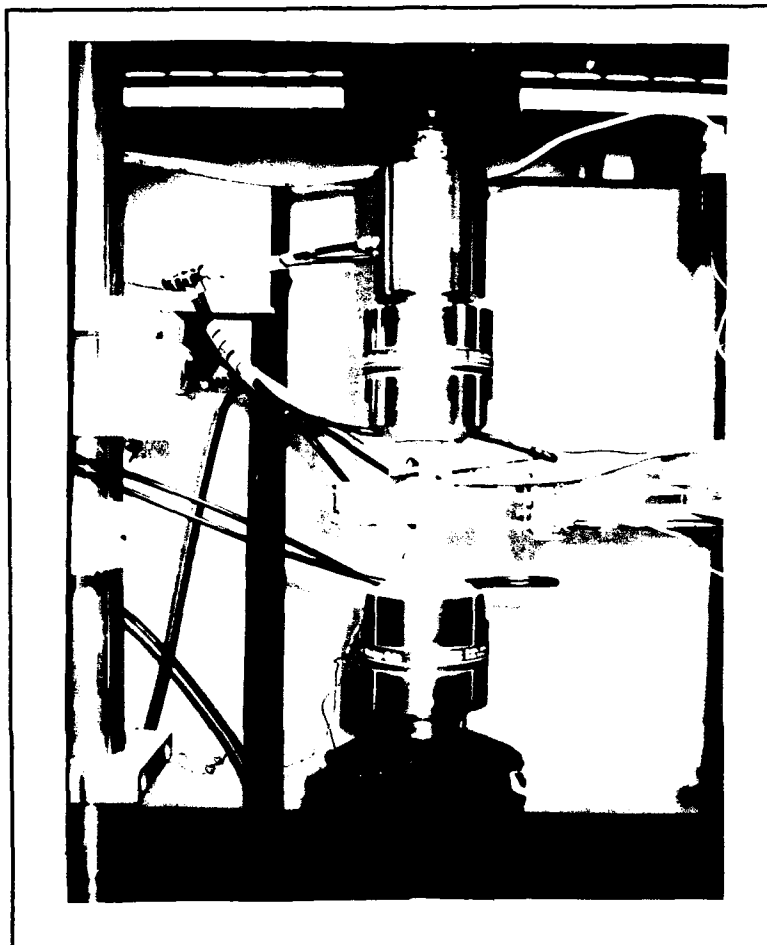


Figure 8. Mounted Test Specimen

Thermal Control Components. Direct thermal control of the test system was accomplished through a Micricon 823 process control system with two feedback channels. The other components of the thermal control system included two quartz lamp heaters, the cooling system and two type-K thermocouples.

Thermal profile control was managed by the MATE263 program during testing through the Micricon unit. MATE263 initially programmed the Micricon with the desired temperature profiles and then continuously monitored and corrected the profiles with data provided by the thermocouples. Two Chromel-Alumel (type-k) thermocouples were spot-welded on opposite sides of the specimen in the heat zone to provide this temperature feedback information. The Micricon uses three-mode proportional, integral, derivative (PID) feedback control for the temperature profiles. Values for the three modes, alternatively the gain, reset and rate, must be programmed into the Micricon to achieve smooth and steady temperature profiles free from erratic oscillations.

To achieve the actual temperature cycling between 149 C and 427 C every 48 seconds in a steady and symmetric fashion, quartz lamps were used in combination with an active air cooling system. The quartz lamps were parabolic strip type heaters employing 1000 watt tungsten-filament quartz lamps which reflected radiant energy off the parabolic surface onto the specimen heat zone. The radiant energy passed quickly to the specimen resulting in very little energy loss in transit. The lamp heaters were mounted to the test stand with an adjustable rod and knuckle arrangement. The mount allowed the lamp to be easily positioned for optimal heating during testing, yet allowed quick access to the specimen for edge replicating by simply swinging the

lamp out. One lamp was positioned on each side of the specimen to uniformly heat the gauge length section. The lamp heaters were cooled by pumping refrigerated distilled water through the lamp cases. A central pump circulated the water through both the lamps and hydraulic grips.

The air cooling system was split into three lines. The first line went to the extensometer cooling vent. The remaining air was split into two lines, one controlled by a manual valve and the other controlled by electrical servo-valve operated by the Micricon control unit. The manual valve line allowed low level bleed air to constantly flow onto the specimen. This was necessary for a constant heating slope in the temperature profile. The servovalve line was opened by Micricon command during the cooling slope of the profile to rapidly cool the specimen from 427 C - 149 C in 24 seconds. Figure 8 shows the lamp heaters, cooling air tubes and thermocouples attached in the heat zone.

The cooling air flow was directed onto the specimen heat zone by two independently adjustable perforated copper tubes connected in parallel. One tube was on either side of the heat zone and positioned such that the air would symmetrically cool the specimen with a downward airflow. Schubbe found this arrangement reduced the temperature variation in a 12.85 mm gauge section to five percent and provided a more localized heat zone (26:34).

The combination of quartz lamp heaters and active air cooling provided good control of the temperature profiles

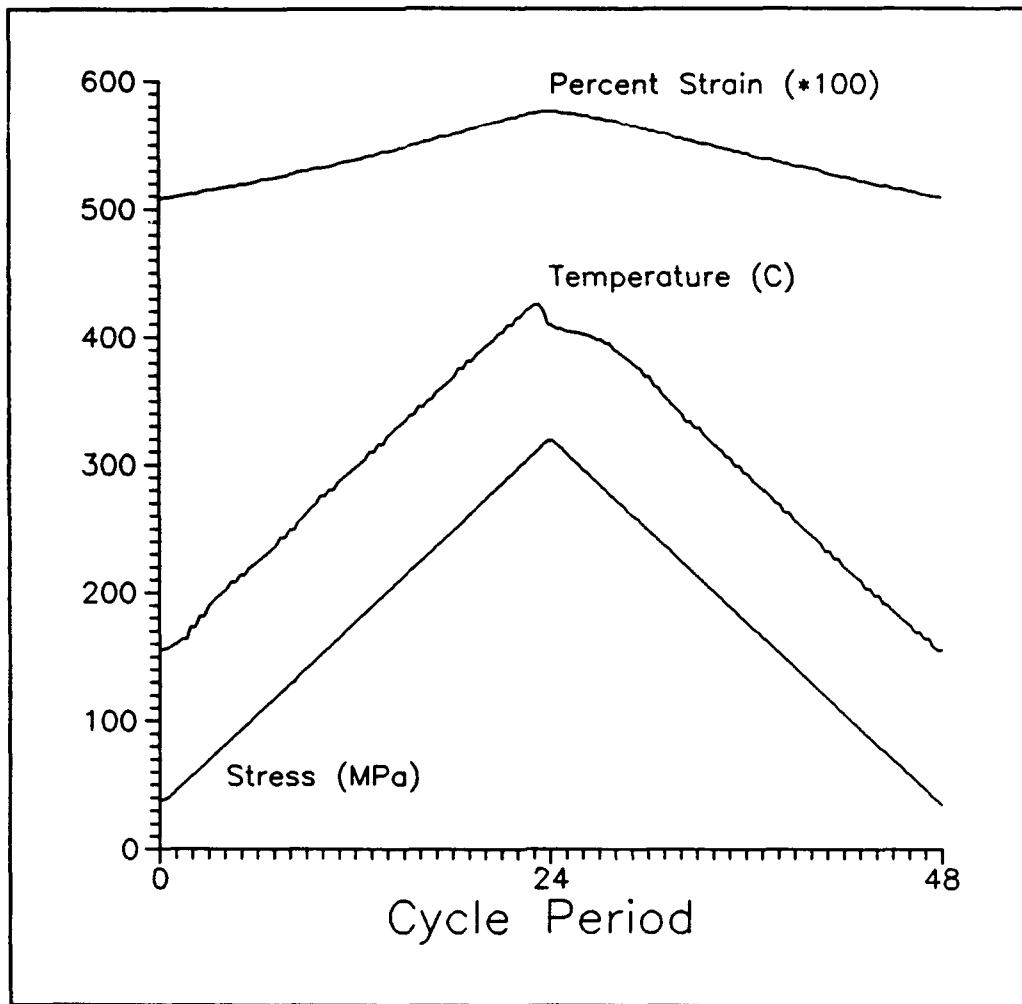


Figure 9. Actual Test Cycle Data

during testing, while minimizing temperature gradients through the thickness. The only exception was the initial cooling slope, where the cooling air quickly dropped the temperature before the Micricon could make the necessary adjustments. Figure 9 shows an actual temperature profile from test cycle data and the corresponding phase relation between the stress and total strain.

Test Procedures

After specimens were cut, aged and polished as described previously, thickness and width measurements were taken to obtain average dimensions for the specimen. The heat zone, gauge length and thermocouple positions were carefully measured and marked. The heat zone was extended beyond the gauge length of the extensometer, ensuring that axial displacement was measured over the heated region. The test specimen was next aligned and mounted in the MTS test stand and thermocouples welded in the heat zone. One thermocouple was spot-welded on each side of the specimen, one offset 6.35 mm above the center line and the other, on the opposite side, offset 6.35 mm below. In this way, the two thermocouples would measure average temperature over the entire gauge length. Figure 10 shows a schematic of a typical test specimen with thermocouple locations. Next, the extensometer was adjusted and mounted against the edge of the specimen at a 25.4 mm gauge length. The extensometer was calibrated and zeroed prior to use. This procedure was repeated several times due to strains exceeding the maximum calibrated displacement of the extensometer. For optimum accuracy, the extensometer should be calibrated just higher than the expected failure strain. Once the extensometer was zeroed and stable, the two lamp heaters were positioned to heat the thermocouple sections on their respective sides. Care was taken to align the lamps horizontally so the heat was transmitted directly to the heat zone and did not

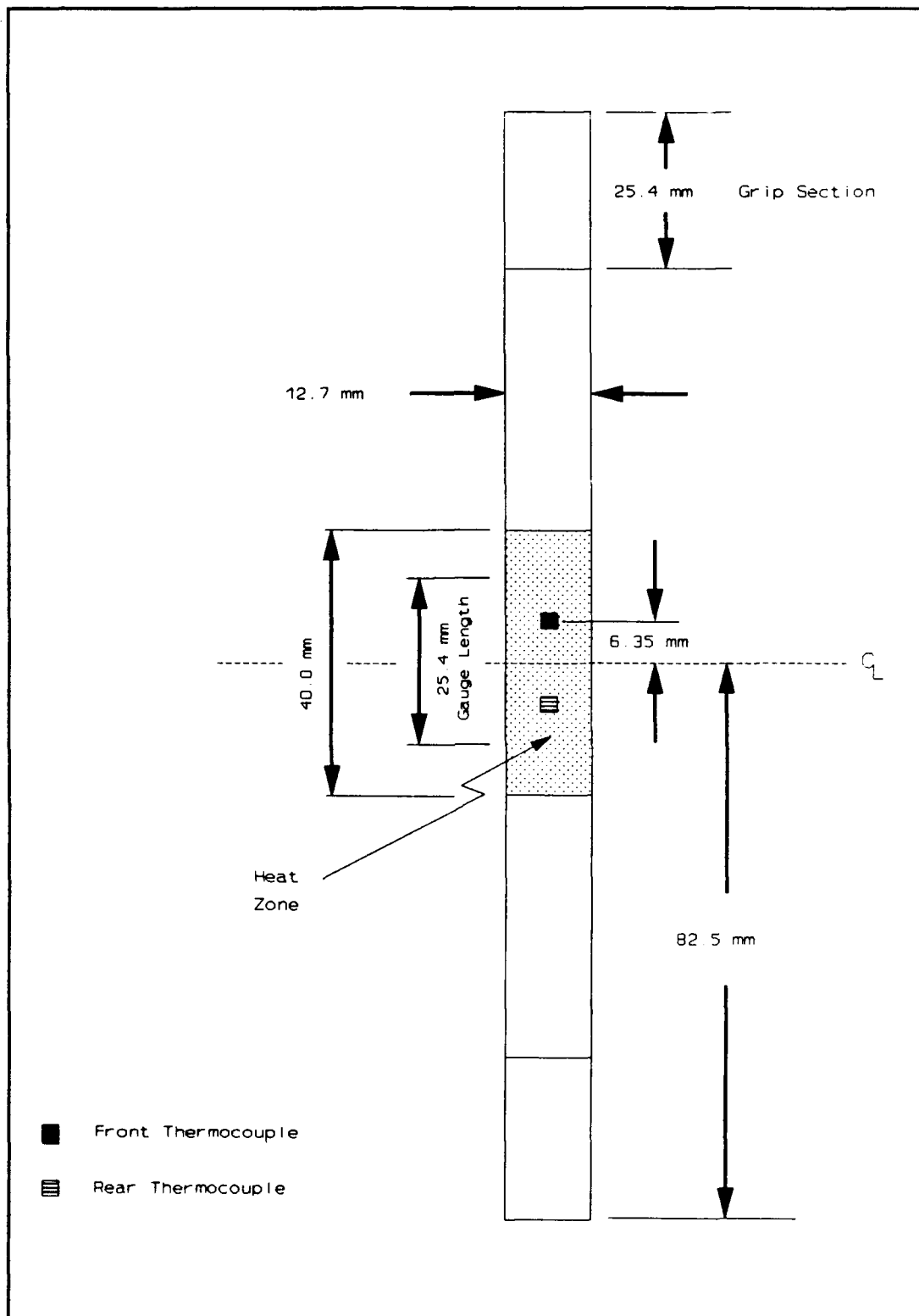


Figure 10. Test Specimen Configuration

intersect the surface at an angle. An incident angle made thermal profiles difficult to establish and maintain since heat from one lamp would be transmitted to the zone on the opposite side, thus upsetting the feedback control loop as it attempted to adjust the thermal profiles.

Before thermomechanical cycling, three preliminary tests were conducted. The first was a room temperature modulus test with the maximum applied load well below the bi-linear knee point so there would be no interface damage. Next, a modulus test at 427 C was conducted, again with a low maximum applied load. For both modulus tests, a computer program specifically designed to record stress-strain data and linearly fit the data was used. The last preliminary was a coefficient of thermal expansion (CTE) test. Here, the specimen was allowed to expand as it was slowly heated from room temperature to 427 C. The temperature and strain ranges were used to calculate a specimen CTE.

Before MATE263 could be started, the gain, reset and rate for each lamp had to be entered into the Micricon. Generally, gains were set between 23 and 28 depending on heating effectiveness of the lamp; resets were set at 20 and rates set to zero. MATE263 was then started and test data was entered into the program. Once test control was turned over to the program, thermal cycling over the requested range began while the load remained constant. The lamps and air flow were adjusted to achieve identical thermal profiles for both thermocouple regions. Once the desired thermal

cycle stabilized, mechanical cycling was initiated. There was usually a significant phase error (approximately 15 degrees) during the first five to eight cycles which disappeared in subsequent cycles. Collecting cycle data for each of the first ten cycles was attempted, however, the current version of MATE263 can acquire only every third cycle. Therefore, only data from the second, fifth, eighth and eleventh cycles was recorded. Also forcing data acquisition cycles (DACs) as often as possible allowed the program to adjust the phase error quickly, since phase adjustments are made only after a DAC.

After the first eleven cycles, the test was put on hold to permit an edge replica and ambient modulus test. Edge replicating involved allowing the temperature and strain to settle to ambient values, applying a low tensile load and placing a thin acetate film against the polished edge of the specimen. Acetone was applied directly to the specimen edge and the acetate film pressed onto the edge before the acetone evaporated. The film became viscous enough to flow into the microstructural cavities present on the edge. After the acetate film dried, it was peeled away from the edge and a detailed impression of the edge remained on the film. Replicas revealed fiber-matrix debonding, reaction zone changes and matrix cracking. In this way, progression of damage during the test was recorded without disturbing the specimen in the test stand. Ambient modulus gave an accurate and simple preview of the effect of accumulated damage

on material stiffness. TMF cycling was resumed with DAC intervals every 10 to 15 cycles (this DAC interval was required for phase corrections). Subsequent replica/modulus stops were made at cycles 100, 250, 500, 1000, 1500, 2000 and every 1000 cycles thereafter. Specimens were thermomechanically cycled to failure.

After failure, the specimen and fracture surfaces were visually and microscopically examined for detail. The specimen was then sectioned, mounted, polished and etched and examined using a optical and scanning electron microscopy, as will be described in Chapter IV.

IV. Results

Test Results Summary

Six $[\pm 45]_2$ SCS-6/Ti-15-3 specimens were tested under fatigue conditions. One specimen was tested under isothermal conditions and the remaining five were tested under in-phase thermomechanical fatigue conditions. The isothermal fatigue test was conducted at 427 C with a maximum applied stress of 360 MPa; three cycles were performed and then the specimen was loaded until failure. This test allowed the stress-strain response of the laminate to be recorded for the first three fatigue cycles, since similar data was not recorded by the MATE263 program. A single TMF test was performed at each stress level. Each TMF test was conducted with a load ratio of 0.1 over a temperature range of 149 C to 427 C.

The pseudo-isothermal fatigue test data was used in determining the maximum applied stress levels for the TMF tests. The first cycle data revealed the knee between the bi-linear regions occurred at 130 MPa and non-linear behavior occurred above 230 MPa. The ultimate strength after three cycles was 510 MPa and total strain at failure was approximately 9.5 percent.

Before fatigue cycling, the initial loading modulus at room temperature and 427 C was measured along with the

coefficient of thermal expansion. Table 3 gives the values of these properties for each specimen.

Table 3. Specimen Properties

<u>Specimen</u>	<u>Ambient Modulus (GPa)</u>	<u>Elevated Modulus (GPa)</u>	<u>CTE (/C)</u>
90 - 07*	104	87	3.62E-6
90 - 08	99	91	3.61E-6
90 - 05	103	86	3.53E-6
90 - 06	101	84	4.11E-6
90 - 10	121	102	3.66E-6
90 - 14	130	112	3.68E-6

* isothermal fatigue test

The five TMF tests were conducted at maximum applied stress levels of 450 MPa, 400 MPa, 350 MPa, 320 MPa and 220 MPa. The first four tests failed at 33, 4345, 3890 and 8690 cycles, respectively. The 220 MPa test was stopped after 21,000 cycles due to time constraints. It is likely the 220 MPa stress was below the fatigue threshold level for this layup. Figure 11 presents the cycles to failure versus maximum applied stress data generated in this study.

Both the isothermal fatigue test and the TMF tests specimens exhibited open stress-strain hysteresis behavior during fatigue cycling. Though the stress-strain response stabilized during TMF testing, the open hysteresis behavior continued until failure. This finite hysteresis for each cycle resulted in a gradual, yet constant, accumulation of

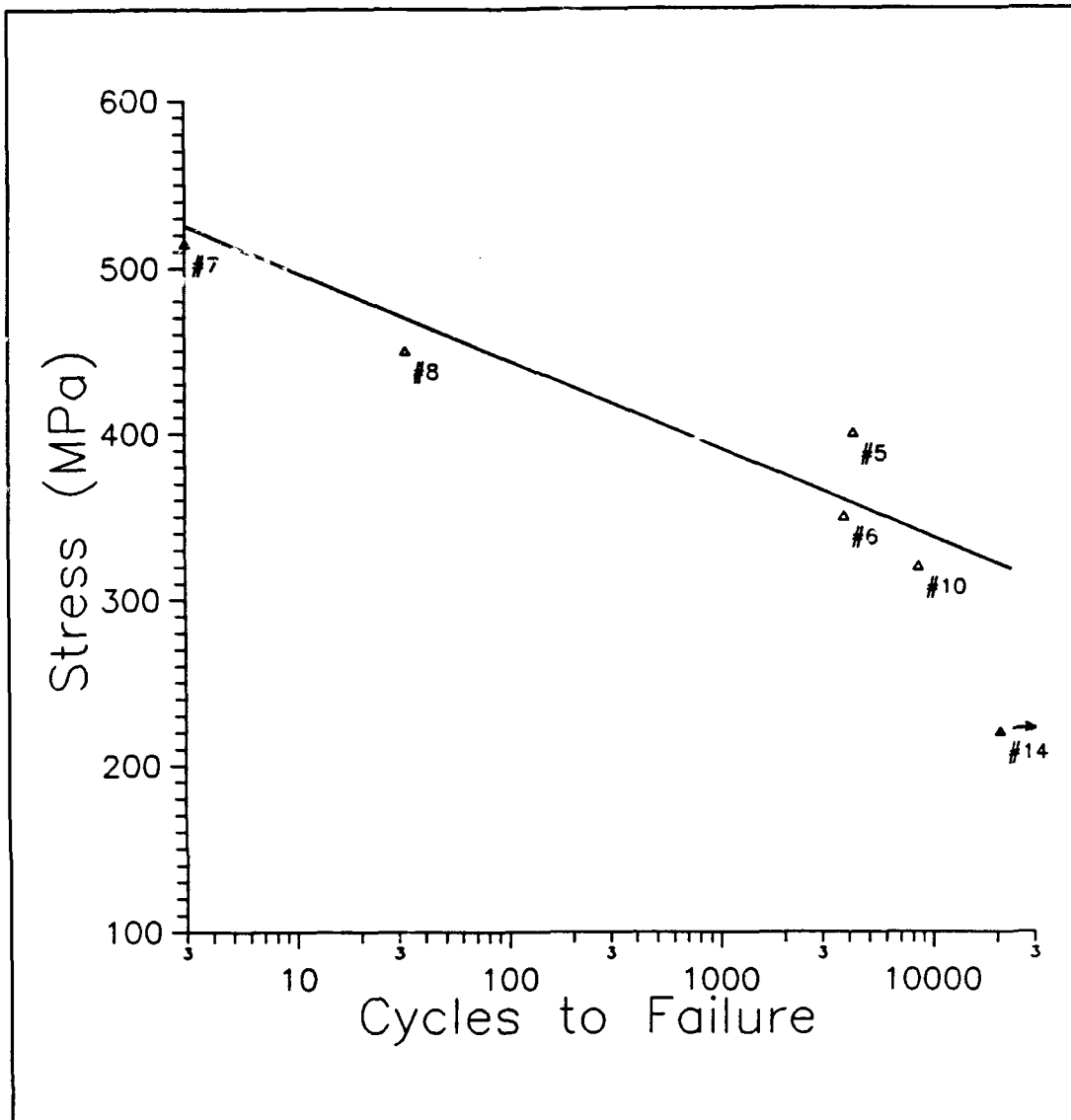


Figure 11. In-Phase Fatigue Life

plastic strain during fatigue testing; this is known as strain ratchetting. The 220 MPa test specimen exhibited open hysteresis behavior for early TMF cycles as it accumulated plastic strain, however, the stress-strain hysteresis almost collapsed as the strain stabilized.

An effect related to the strain ratchetting is the difference in specimen failure strains. Each specimen failed at a total strain that was proportional to the maximum applied stress. In contrast, Schubbe found a critical failure strain in a similar TMF study of $[0/90]_2$, SCS-6/Ti-15-3 (26:113). Figure 12 shows the proportional relationship between the fatigue stress range and total strain at failure for each specimen.

A common characteristic of all fatigue specimens was the continued bi-linear stress-strain response during fatigue cycling. The knee between the two linear regions decreased initially but stabilized and remained essentially constant until failure. The unloading portion generally did not show two distinct linear regions, though the subsequent loading portion did exhibit the typical bi-linear response.

The failure in the TMF specimens was characterized by matrix cracking and plasticity and extensive fiber-matrix debonding, regardless of the maximum cycle stress. The dominant role of the matrix in failure was also revealed by the high failure strains (over 12 percent in one test). The impact of applied cycle stress was seen primarily when comparing the extent of fatigue crack progression and the extent of tensile overload damage in the matrix. Lower cycle stress levels provided increased cycle life which allowed fatigue damage to progress further through the matrix.

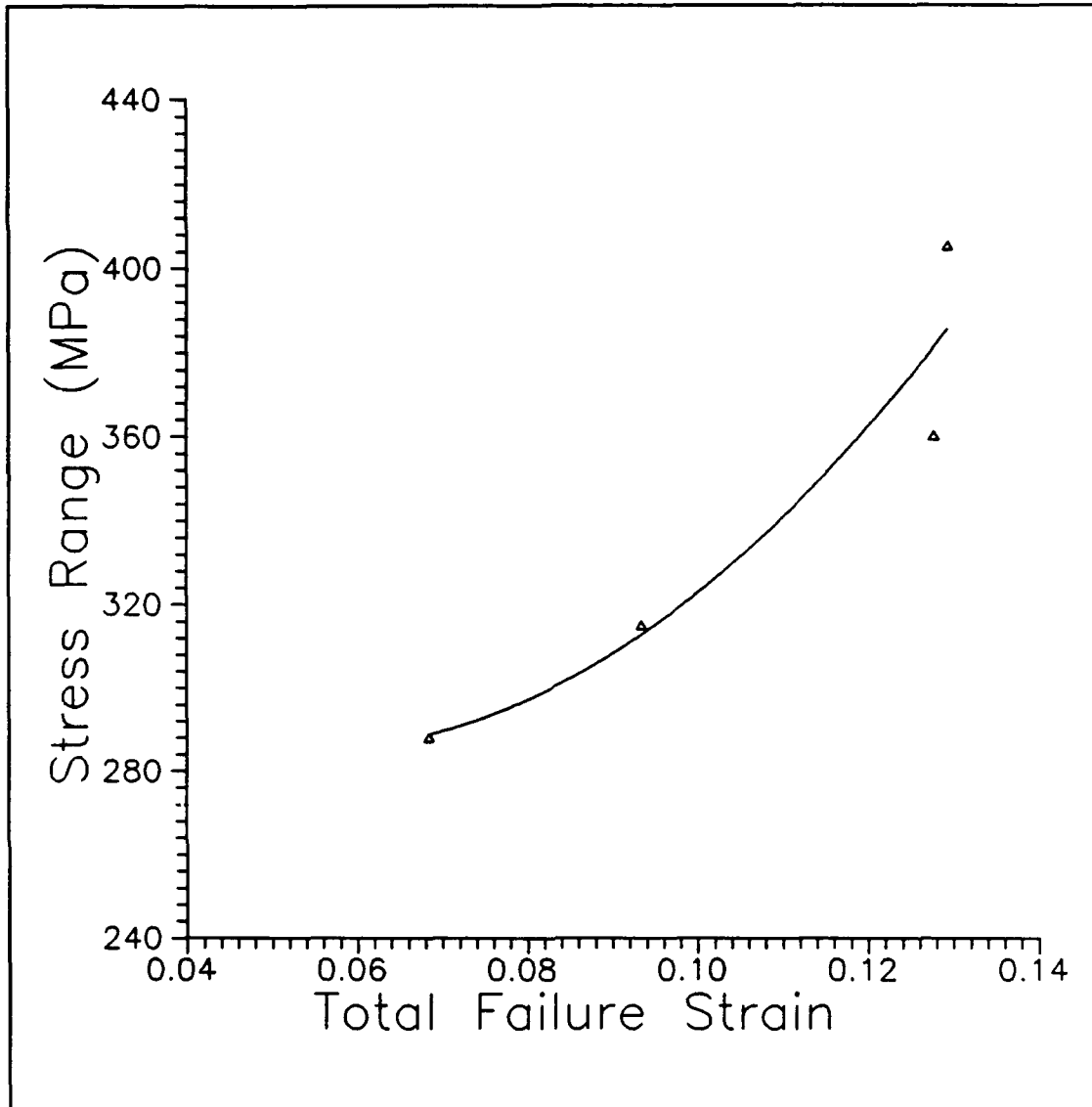


Figure 12. Fatigue Stress Range vs. Total Failure Strain

This chapter will concentrate on the TMF test results, but will use the simpler case of the isothermal fatigue (IF) test to introduce each result section and to provide a basis for comparison between tensile overload failure and thermo-mechanical fatigue failure. Strain measurements, modulii

measurements and damage analysis for the IF and TMF tests are discussed.

Strain Measurements.

Total strains were recorded periodically during testing for the TMF specimens. Mechanical strains obtained from the total strains were used in data analysis. The assumed relation between the total strain and the mechanical strain is given in Equation 5:

$$\epsilon_T = \epsilon_M + \epsilon_\alpha \quad (5)$$

where ϵ_T , ϵ_M and ϵ_α are the total, mechanical and thermal strains, respectively. For in-phase cycling, the thermal strain is simply subtracted from the total strain to yield the mechanical strain. The relation in Equation 5 is not exact for metal matrix composites since there is some associated mechanical strain induced by the CTE mismatch at the fiber-matrix interfaces due to thermal expansion. However, in this study due to the large failure strains, the magnitude of the thermal strains is sufficiently small compared to that of the mechanical strains and Equation 5 can be used to calculate mechanical strains.

Isothermal Fatigue Test. Table 4 presents the maximum mechanical strain and the permanent plastic strain offset upon unloading for the three fatigue cycles. The majority of the permanent plastic strain accumulated in the first

cycle, with continued but smaller accumulation in subsequent cycles. The progression of the strain by cycle shows the strain ratchetting typical for this layup during fatigue cycling.

Table 4. Isothermal Fatigue Test Mechanical Strains

<u>Cycle</u>	<u>Max e_M (%)</u>	<u>Strain Offset (%)</u>
1	1.7	1.0
2	1.86	1.1
3	2.12	1.35
4	9.5	Failure

From this data, it is evident that during the first cycles plastic strain accumulated rapidly, with the first cycle being the most significant. Also, it should be noted that the strain at failure was greater than 9.5 percent, well above the one percent failure strain for the fibers. This large plastic deformation occurs since there are no 0 degree fibers to limit longitudinal strain and suggests the important role of the matrix in the [± 45] layup in carrying load at high strain levels. Similar trends can be expected in the TMF specimens -- a rapid accumulation of plastic strain during the early fatigue cycles, strain ratchetting as the plastic strain continues to accumulate and large strains at failure.

Thermomechanical Fatigue Tests. Table 5 summarizes the total strain at failure and the associated mechanical strain

for the four specimens which failed. The test which was stopped at 21,000 cycles (220 MPa test) is also included.

Table 5. Failure Strain Summary

<u>Test</u>	<u>Cycles to Failure</u>	<u>Total Strain (%)</u>	<u>Mechanical Strain (%)</u>
450 MPa	33	13	12.73
400 MPa	4345	12.77	12.51
350 MPa	3890	9.35	9.05
320 MPa	8690	6.84	6.57
220 MPa	--	2.33	2.06

The strain histories for each fatigue test are presented in Figures 13 through 17. The maximum and minimum mechanical strain and the difference between the two is shown as a function of cycle life. There are general trends common to all test specimens, independent of the maximum cycle stress. First, there is an immediate and rapid accumulation of strain during approximately the first ten percent of the specimen cycle life. In the case of the 450 MPa and 400 MPa tests, over 80 percent of the mechanical strain at failure was accumulated in the first 30 percent of cycling. The lower stress tests did not exhibit as rapid strain growth during the early cycles, but still showed this to be the fastest period of growth. After this period of rapid strain accumulation, the majority of fatigue life was marked by a slower and very stable growth of the strain. This steady period of strain progression continued until failure. Specimens did not exhibit a rapid and dramatic increase in

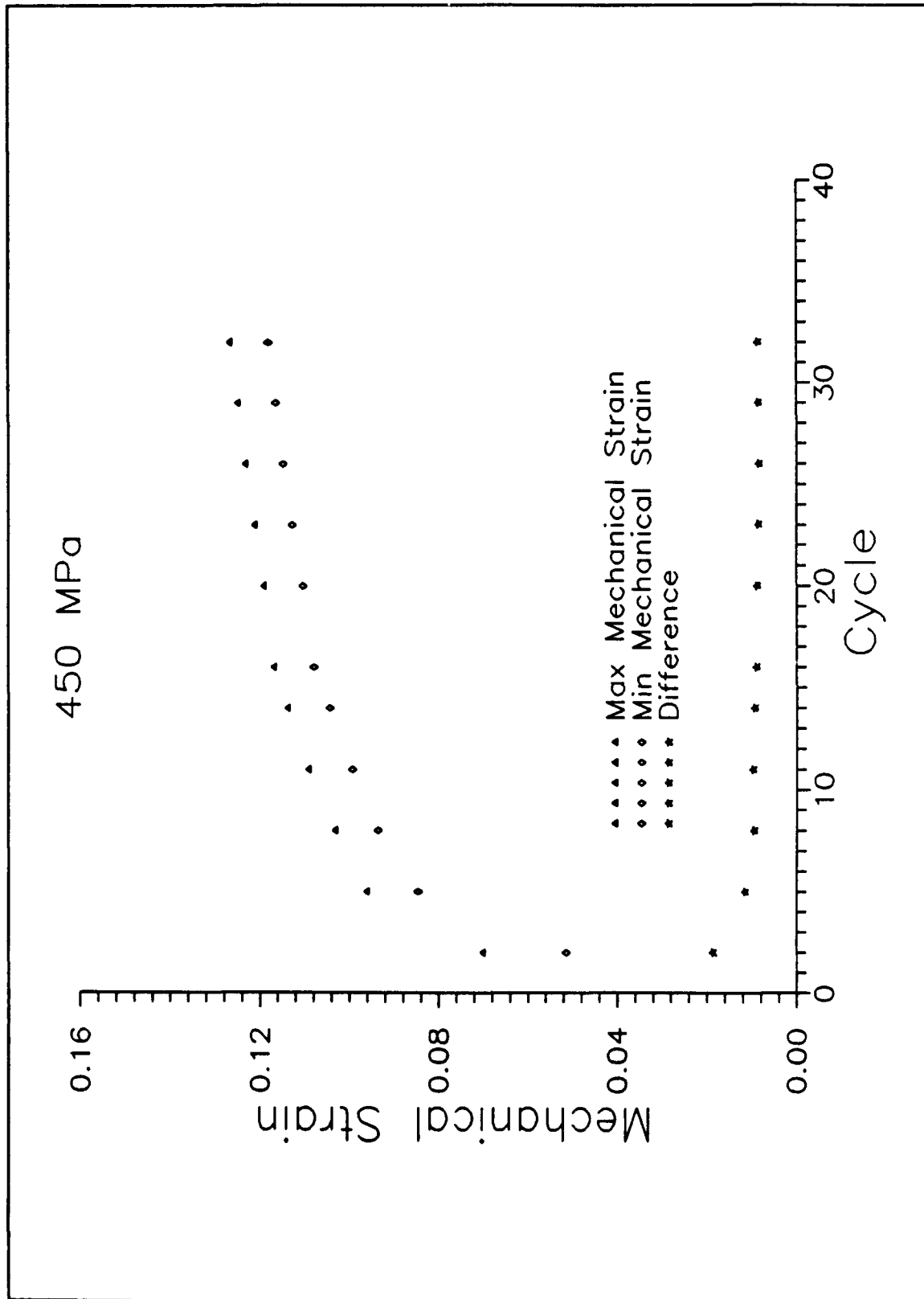


Figure 13. Strain Data for 450 MPa Test

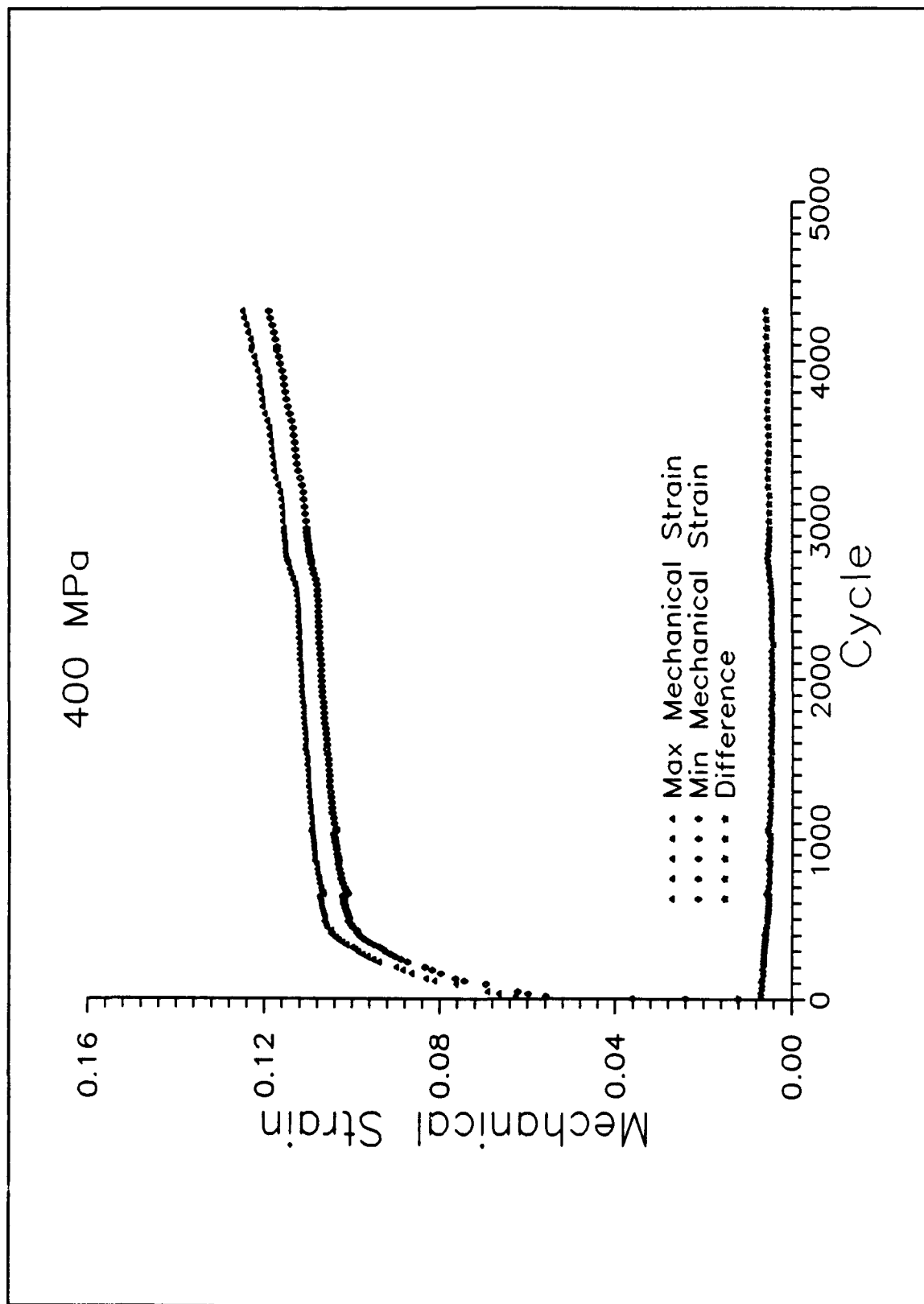


Figure 14. Strain Data for 400 MPa Test

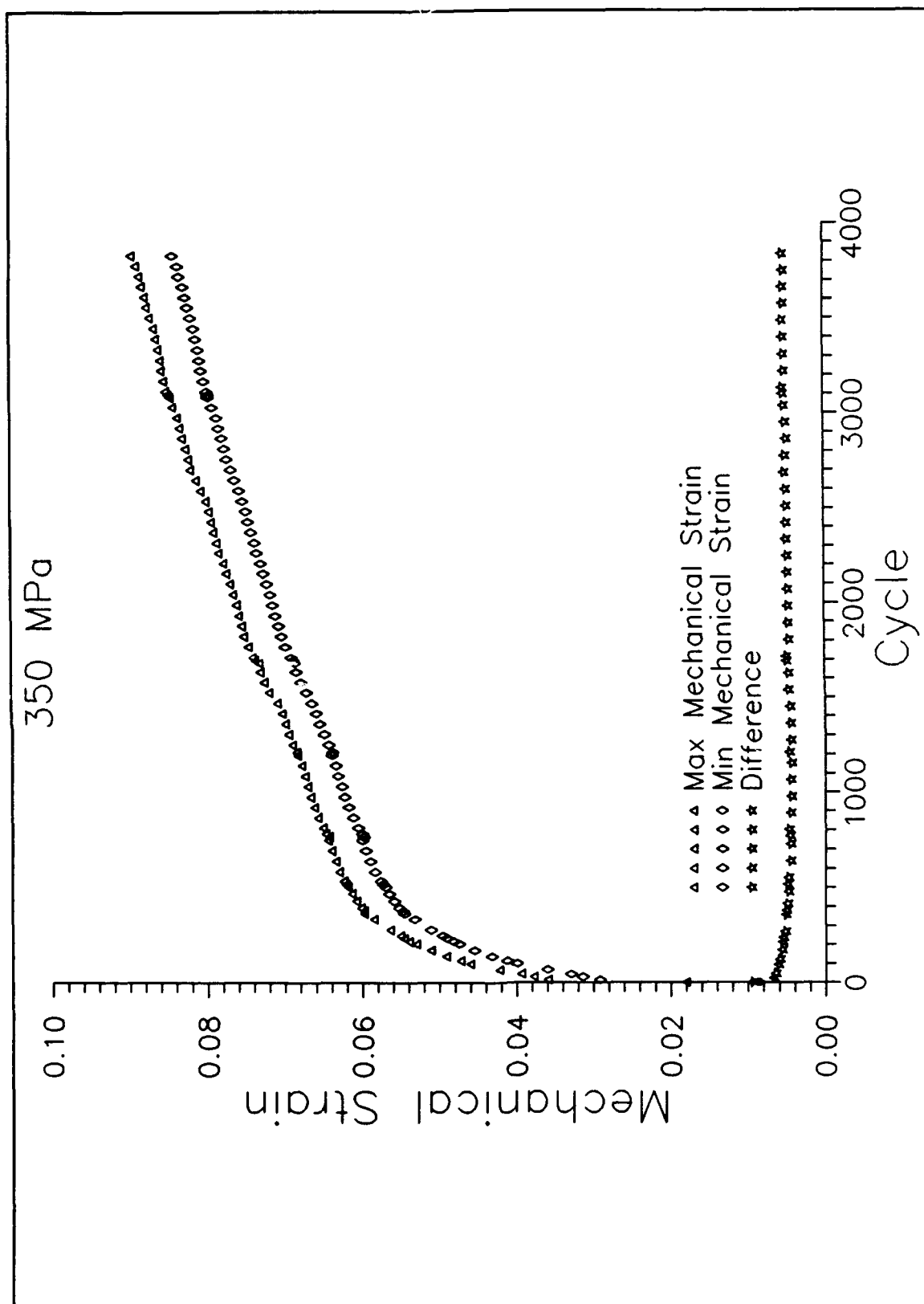


Figure 15. Strain Data for 350 MPa Test

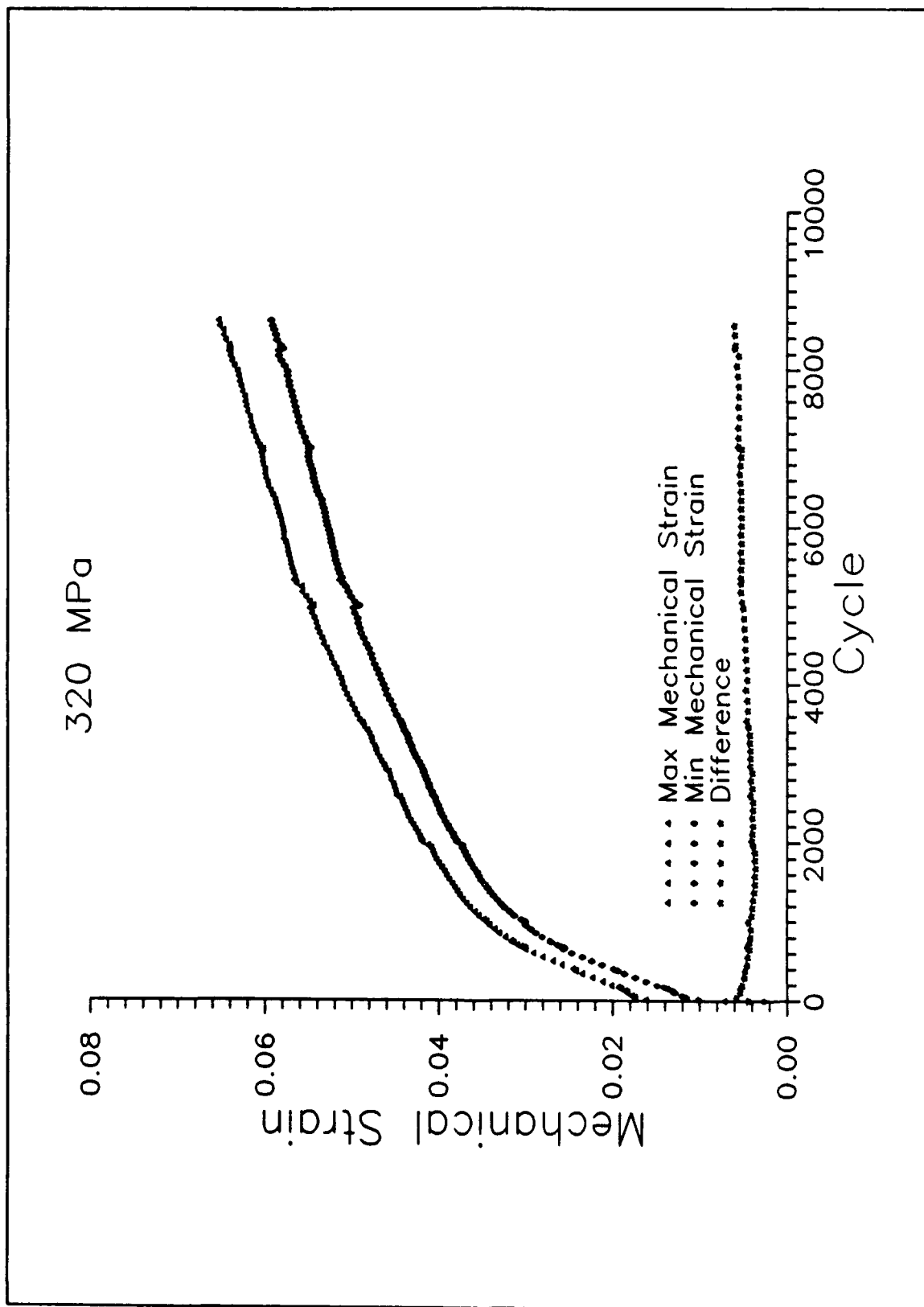


Figure 16. Strain Data for 320 MPa Test

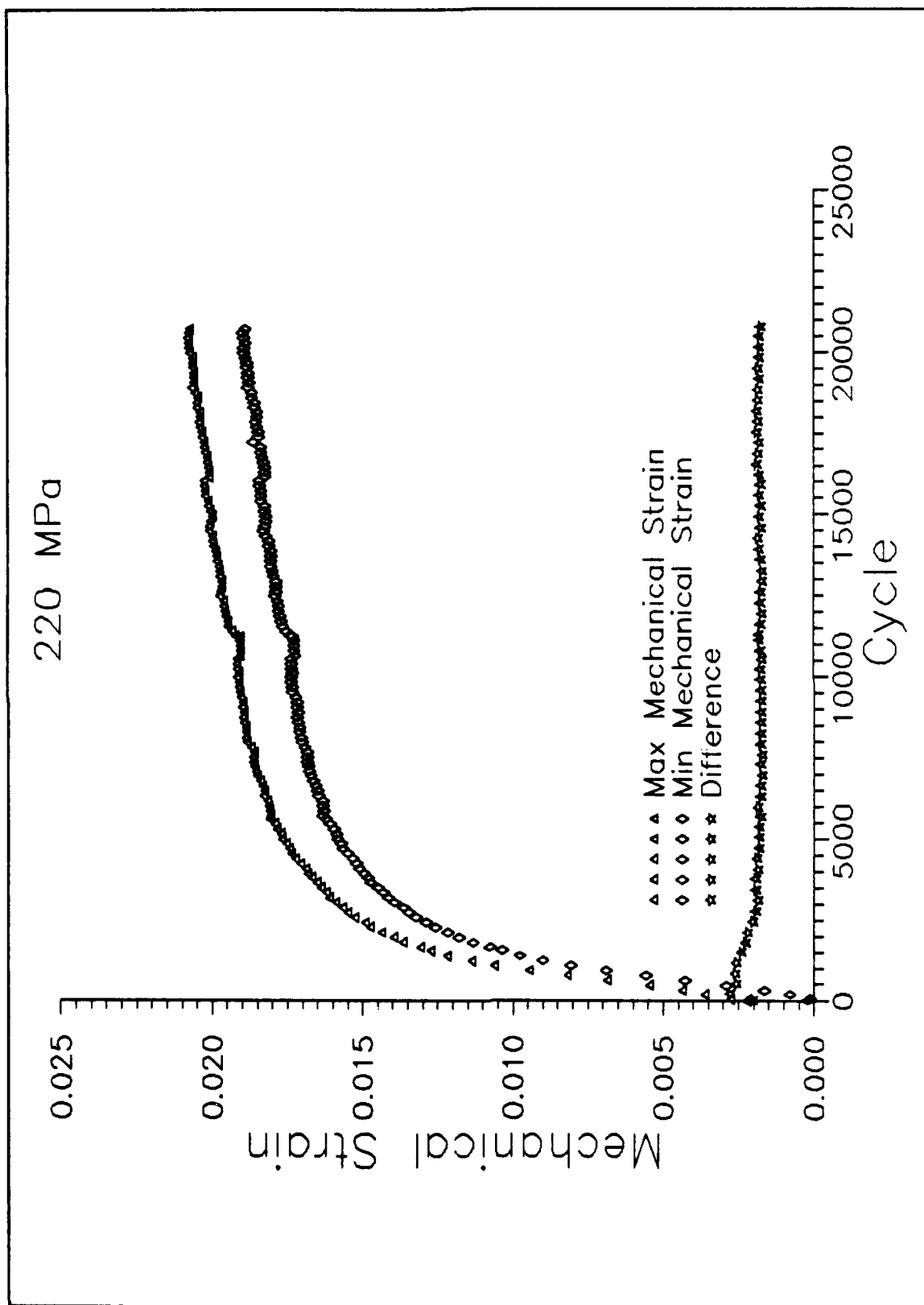


Figure 17. Strain Data for 220 MPa Test

strain near failure, but continued to plastically deform at a steady rate. This indicates a brittle fracture at failure, since the laminate did not yield dramatically which would occur in a ductile failure.

Another trend shared by all test specimens is found in the change in the difference between the maximum and minimum mechanical strains during fatigue cycling. From the first cycle, the difference decreases initially, reaches a minimum value and then remains essentially stable with a slight upward trend for the remainder of the cycle life. The initial period of declining strain difference corresponds to the period of rapid strain accumulation. As the strain progression stabilizes, the strain difference also stabilizes.

Figures 18 through 22 show the strain progression for selected cycles for all specimens tested. The figures show graphically the strain ratchetting occurring in each test. Here again the disproportionate amount of strain accumulation in the early cycles is evident. The second cycle for the 450 MPa, 400 MPa and 350 MPa tests shows extensive plastic yielding. It can be assumed from the isothermal fatigue data that similar, if not greater, plastic deformation occurred during the first cycle of these tests. Each test revealed stress-strain hysteresis which continued to failure. The width of the hysteresis was greatest during the first twelve cycles, but rapidly decreased after that and remained relatively stable for the remainder of the

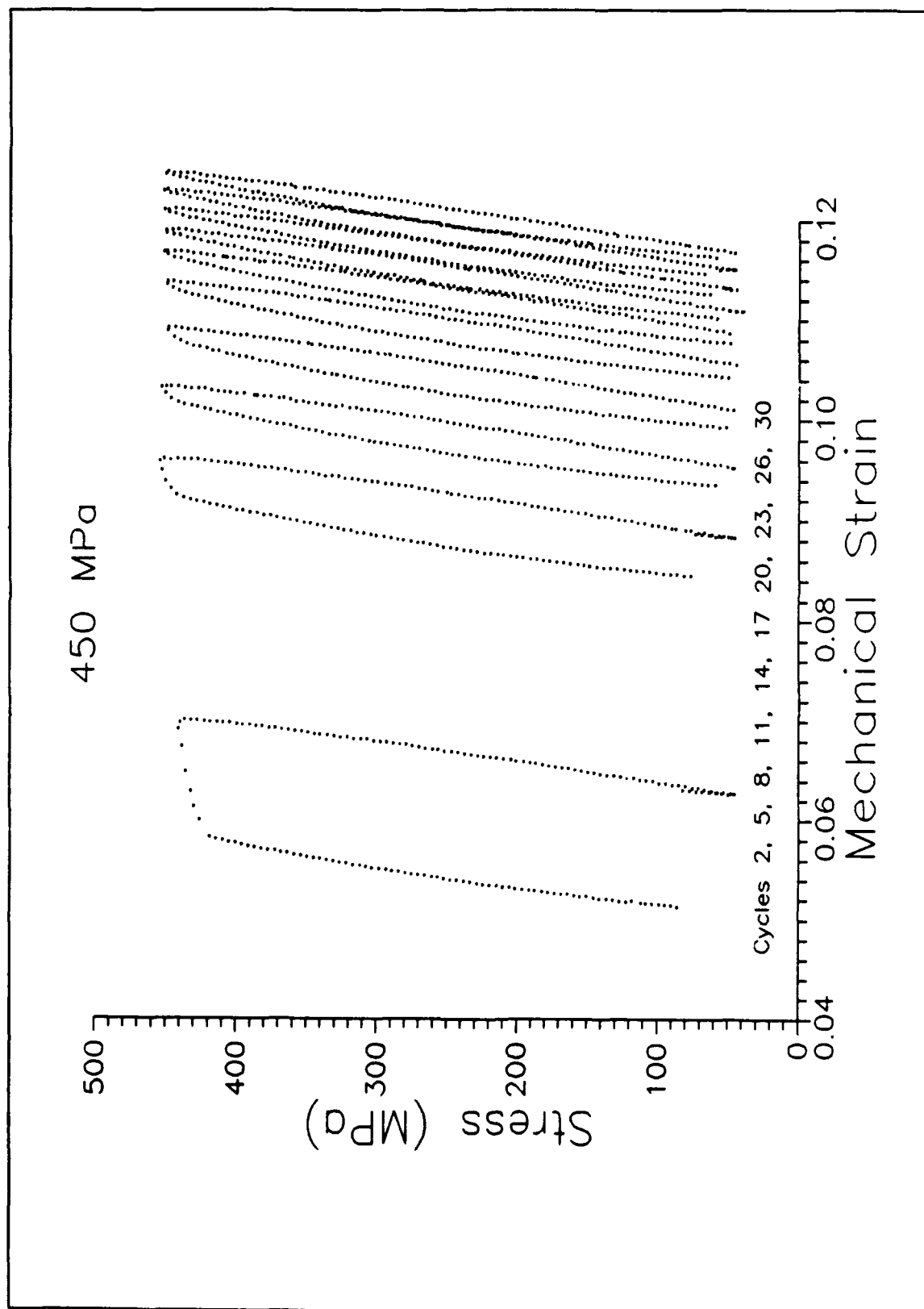


Figure 18. 450 MPa Strain Progression

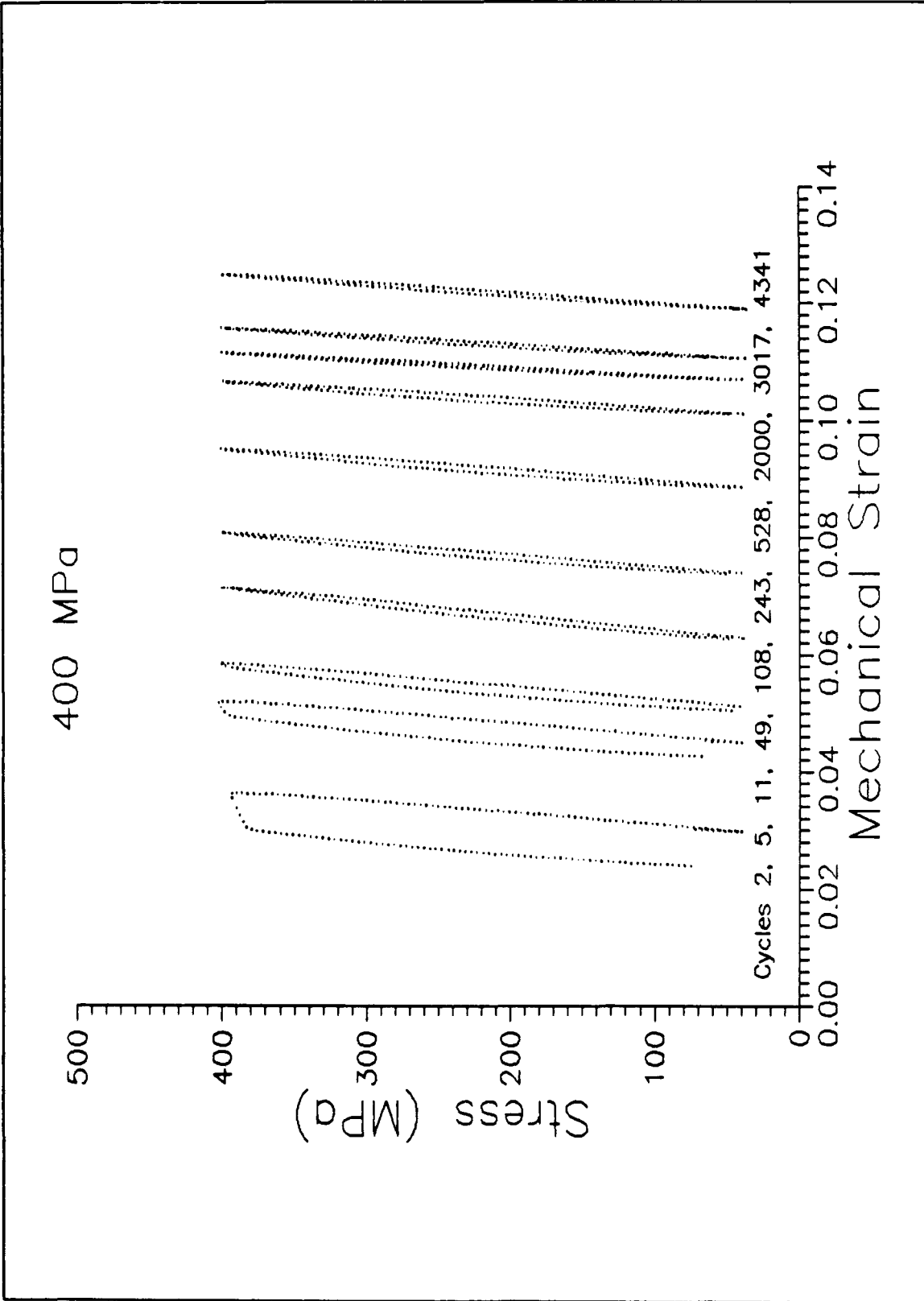


Figure 19. 400 MPa Strain Progression

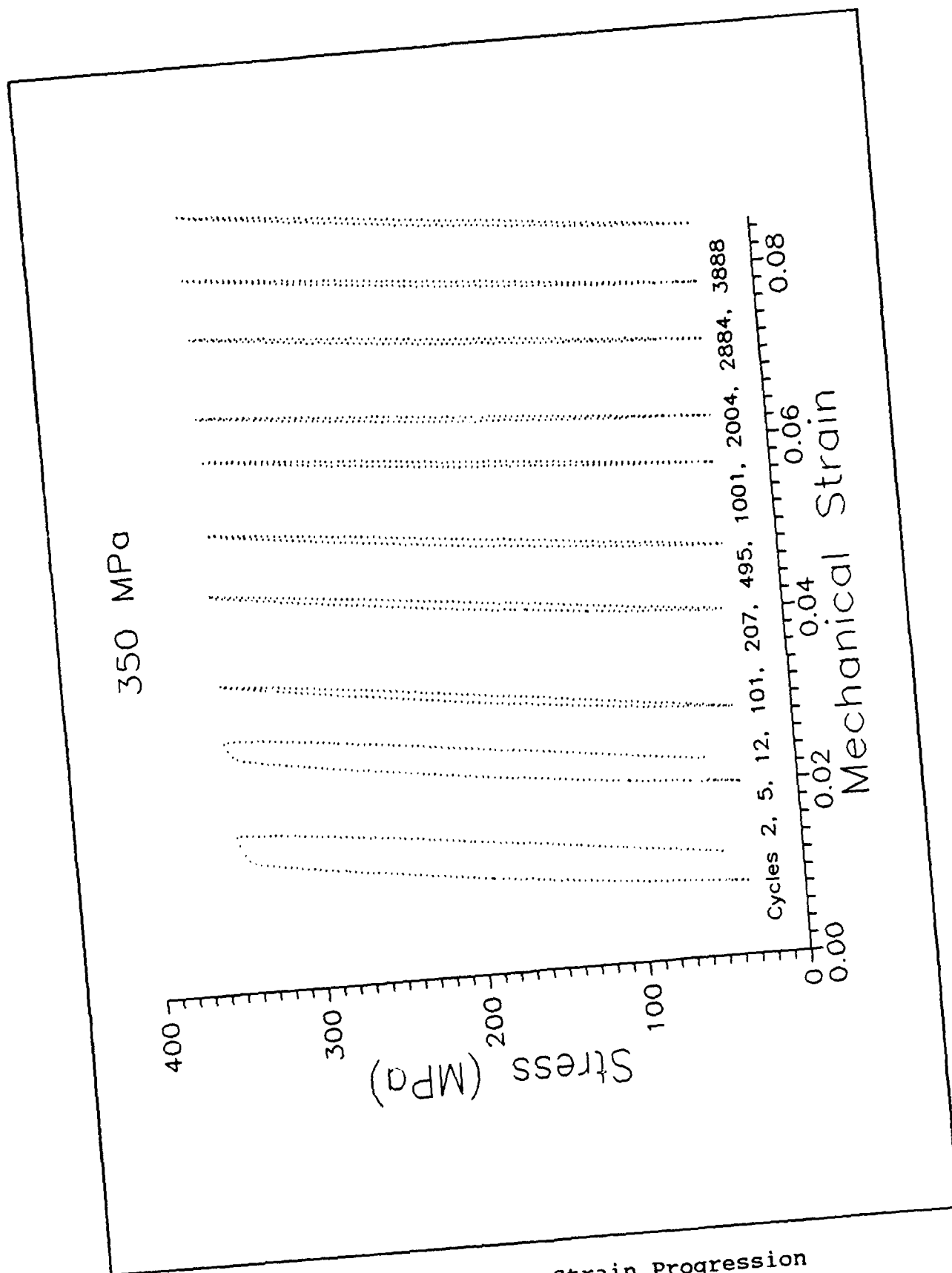


Figure 20. 350 MPa Strain Progression

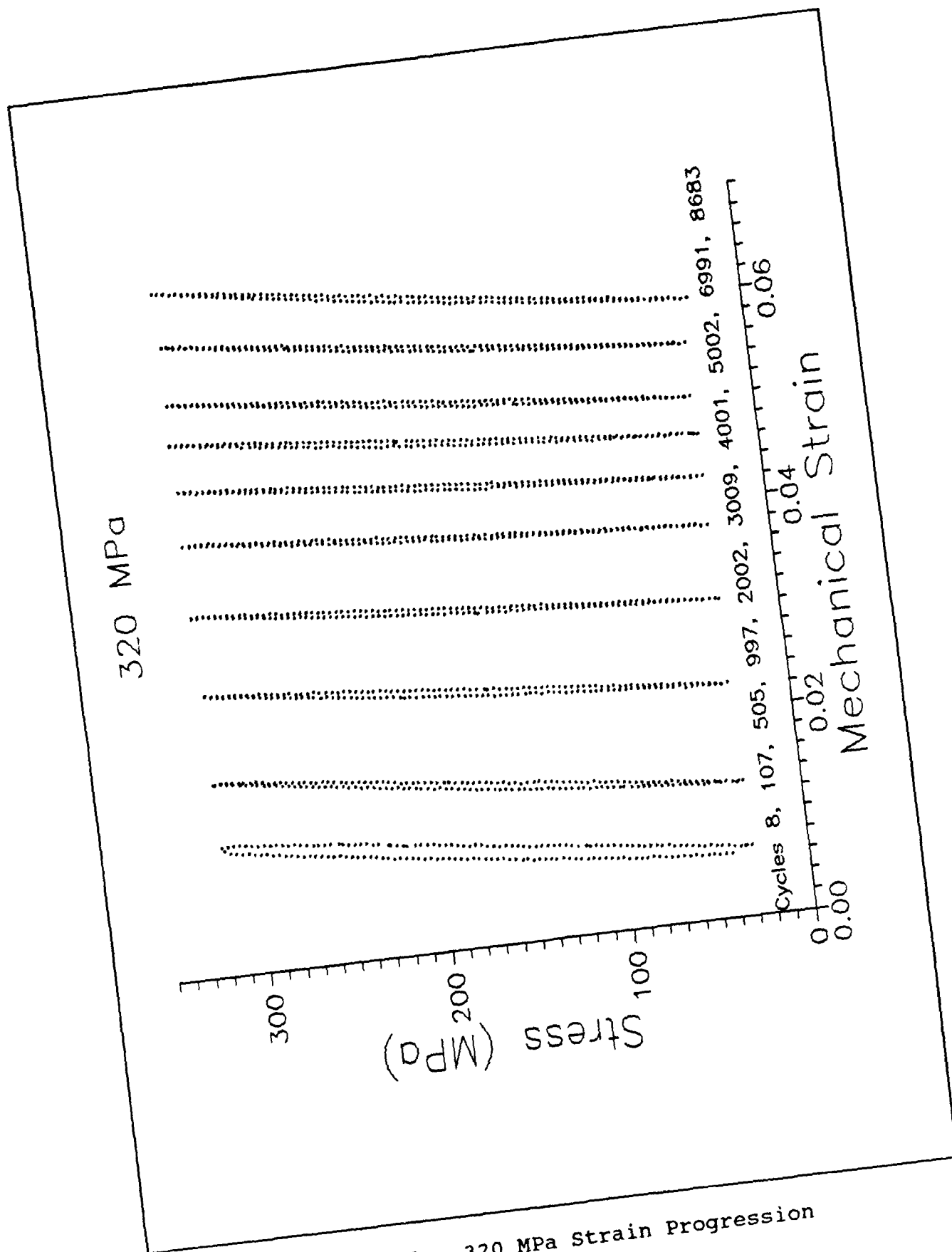


Figure 21. 320 MPa Strain Progression

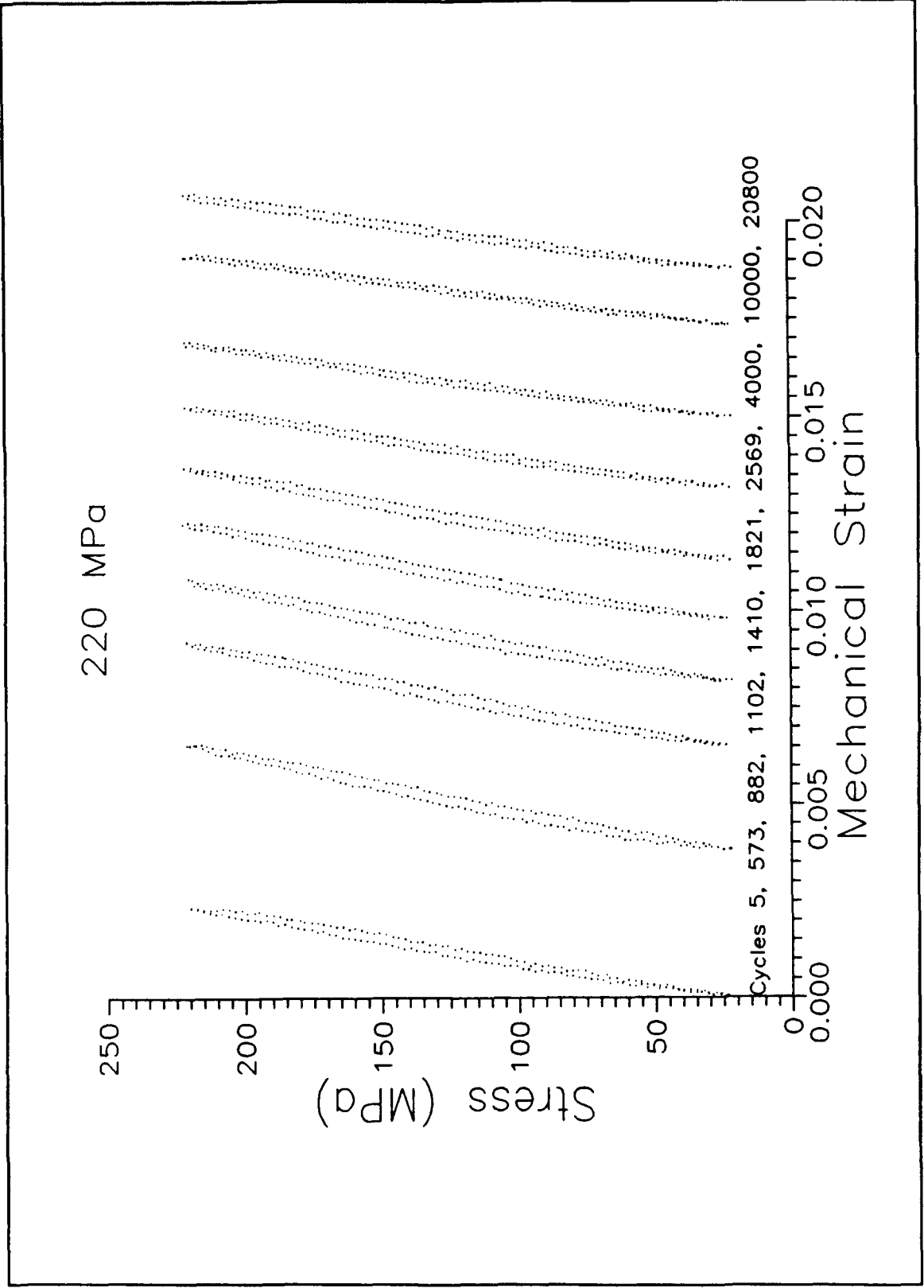


Figure 22. 220 MPa Strain Progression

cycle life. The stabilized hysteresis width is proportional to the applied cycle stress level. Though the hysteresis width was small for the 320 MPa and 220 MPa tests, it remained finite, which indicates irreversible deformation accumulating during the cycle.

To summarize, all specimens failed at total strains greater than six percent; the largest failure strain being 13 percent. The total failure strain was found to be proportional to the maximum applied cycle stress. All specimens exhibited rapid strain accumulation, stress-strain hysteresis and strain ratchetting to failure.

Modulii Measurements

The modulus of a material can be a useful parameter when attempting to quantify damage through a change in stiffness. Due to the bi-linear response of the composite used in this study and the constant stress-strain hysteresis, a single modulus does not fully describe the mechanical response of the laminate. Instead, three modulii were used to describe the stiffness loss related to the damage accumulation during cycling. Figure 23 is an idealized schematic of a typical stress-strain curve observed during TMF cycling. The three modulii used are shown in the schematic. E_1 is the initial loading modulus, E_2 is the secondary loading modulus and E_u is the unloading modulus. A knee upon unloading, corresponding to closure of fiber-matrix debonding, was occasionally observed. The stiffness,

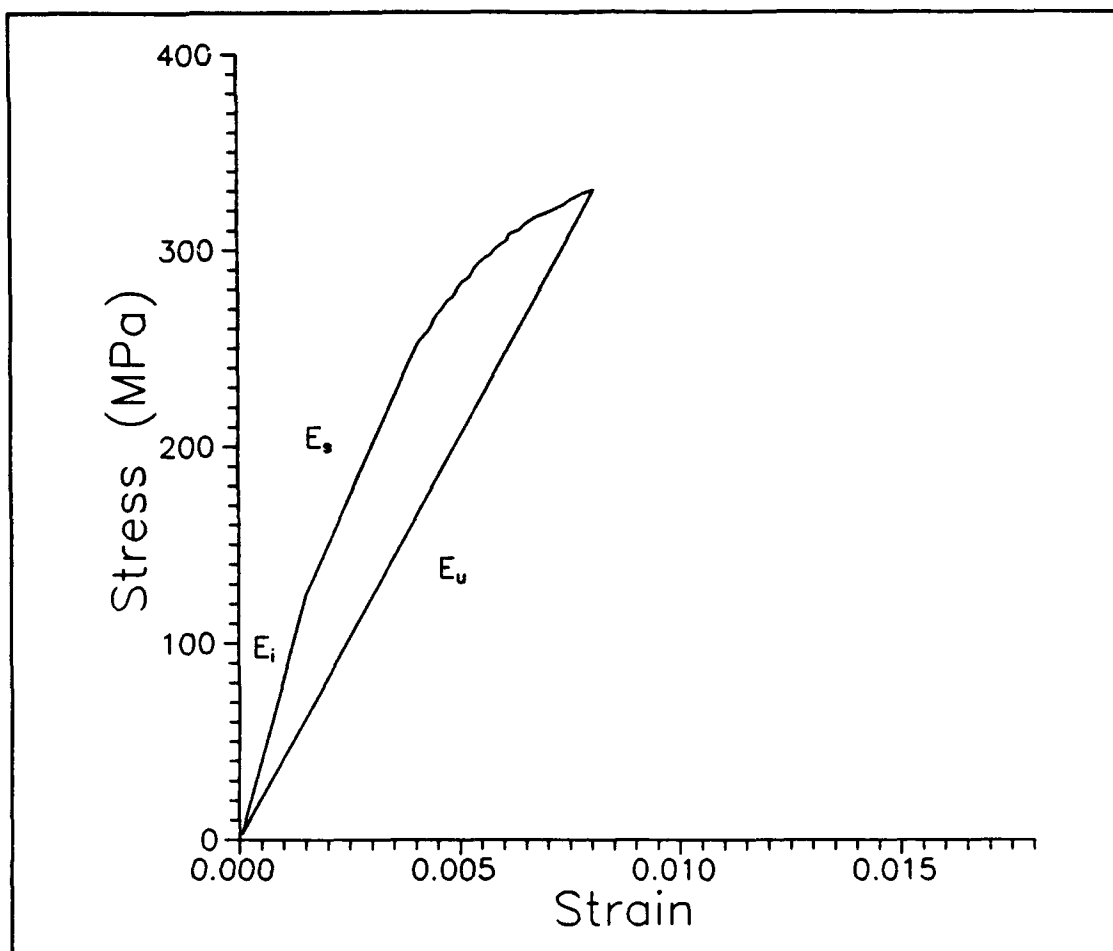


Figure 23. Idealized Schematic of a Typical Stress-Strain Curve

however, did not differ greatly between the two regions and E_u was effectively used as the slope for the entire unloading region.

Modulii for the TMF tests were calculated using a computer program (MATE233) which employed a least squares fit to the engineering stress and mechanical strain data recorded during cycling. Mechanical strains were calculated using Equation 5.

Isothermal Fatigue Test. Figure 24 presents the cycle stress-strain response for the isothermal fatigue test. Moduli were calculated for the three linear regions discussed previously. Table 6 lists the values for the moduli for each cycle.

Table 6. Isothermal Fatigue Cycle Moduli

Cycle (MPa)	E_1 (GPa)	E_s (GPa)	E_u (GPa)	Knee (MPa)
1	83.3	54.5	45.6	130
2	77.8	46.5	42.7	80
3	73	41.8	43.4	72
4	67	39.4	--	74

The calculated moduli show distinct trends from cycle to cycle. Both loading moduli, E_1 and E_s , decrease for each consecutive cycle, showing the effect of damage. The unloading modulus stabilizes after the first cycle and seems related to the secondary loading modulus. Though the unloading knee and bi-linear response are not obvious upon unloading, the physical phenomenon which causes this behavior is still occurring. This can be seen in the loading response during the subsequent cycle. The initial loading modulus is much higher than the unloading modulus from the previous cycle, yet after the knee, the secondary loading modulus equals the unloading modulus from the previous cycle. This implies that the fiber-matrix bond is being re-established during the unloading portion and subsequently relaxed during the loading portion of the next cycle. The

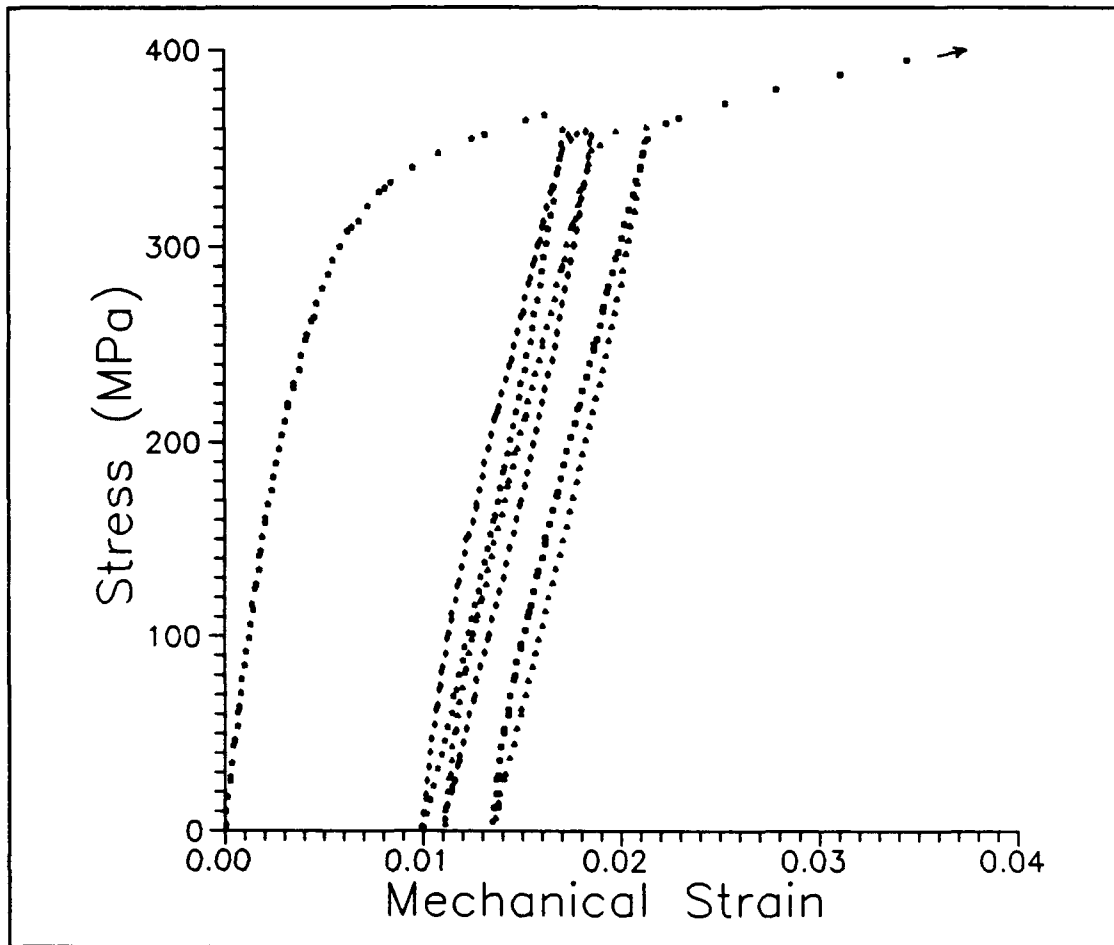


Figure 24. Stress-Strain Data for IF Test

stress level at which the loading knee occurs shows a significant drop after the first cycle, continues to decrease and then seems to stabilize. The difference between the initial knee level (130 MPa) and the stabilized knee level (73 MPa) may be a measure of the strength of the fiber-matrix bond.

In general, both loading moduli experienced significant losses in the first three cycles, the unloading modulus stabilized and corresponded with the secondary loading

modulus and the knee level decreased dramatically during the first cycle and then stabilized.

Thermomechanical Fatigue Tests. Moduli analysis for the five TMF specimens revealed similar trends as observed in the IF test. Figures 25 through 29 present the calculated moduli versus cycle life for each tested specimen. As seen in the IF test, the secondary loading modulus and the unloading modulus are very close in value and significantly less than the initial loading modulus. A stabilized loading knee between 80 and 100 MPa was common during each test, which remained throughout cycle life. The exception being the 450 MPa test which exhibited highly non-linear behavior during the loading portion.

Three distinct trends common to all moduli can be seen during cycle life (with the exception of the 450 MPa test). First, there is a sharp and dramatic decrease in the stiffness during the first 10 to 50 cycles. For the initial loading modulus, this corresponded to about a 20 percent drop from the uncycled value. The decrease in the other moduli was not as severe, but averaged between 10 to 15 percent. The second trend is a period of stable stiffness increase continuing for 1000 to 2000 cycles. This hardening period resulted in the initial loading modulus recovering most of the early losses and approaching the original uncycled value. The secondary loading modulus and the unloading modulus also experienced gains of similar magnitude. The 450 MPa test did not show this trend, though failure

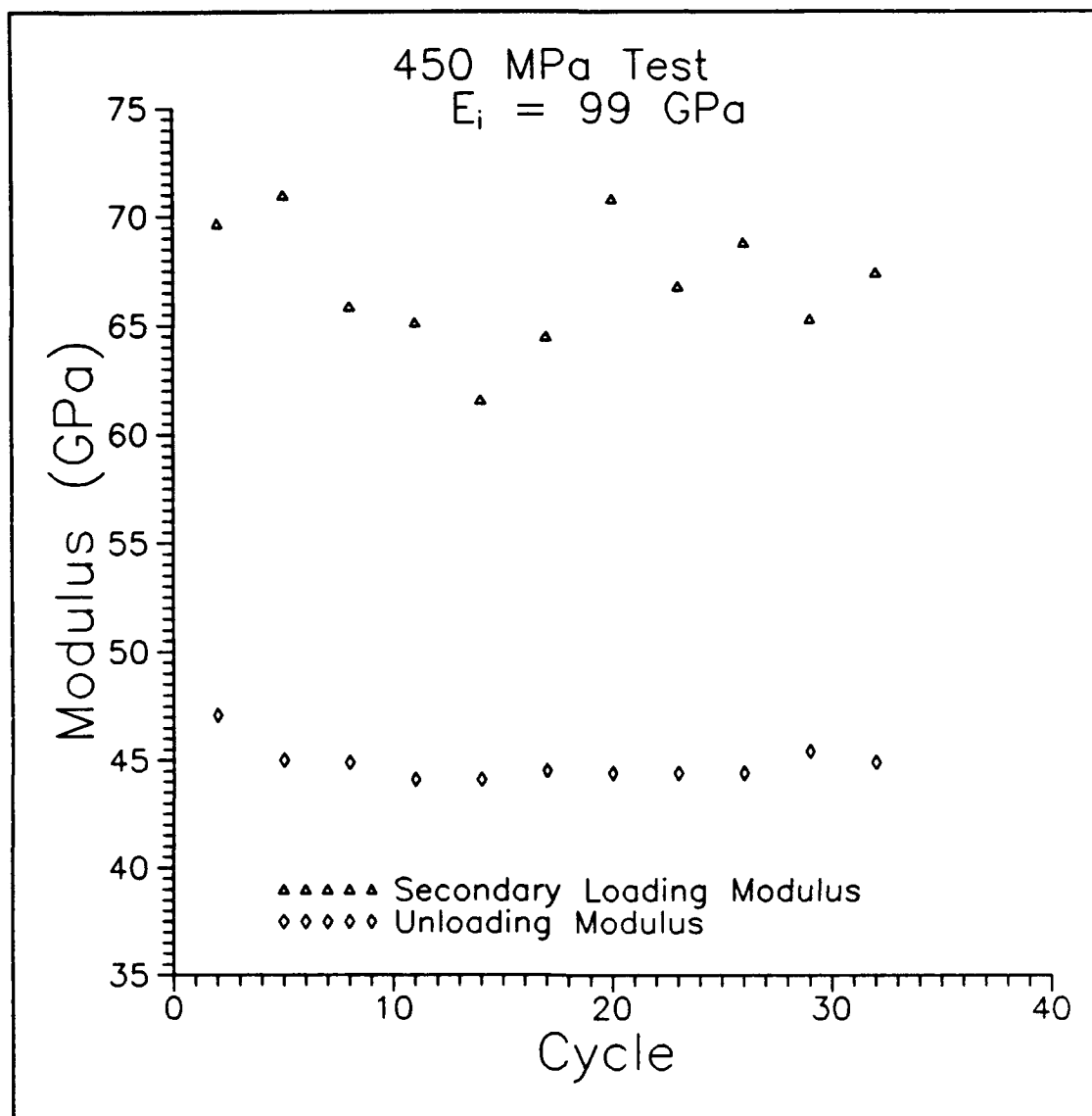


Figure 25. Modulii for 450 MPa Test

occurred after only 33 cycles. The 220 MPa test exhibited stiffness increase for 5000 cycles. In each test, the increase occurred in all modulii over the same period. This precludes the possibility of the increase being an effect caused by a poor linear fit and implies that the composite as a whole experienced a stiffness change. The last trend

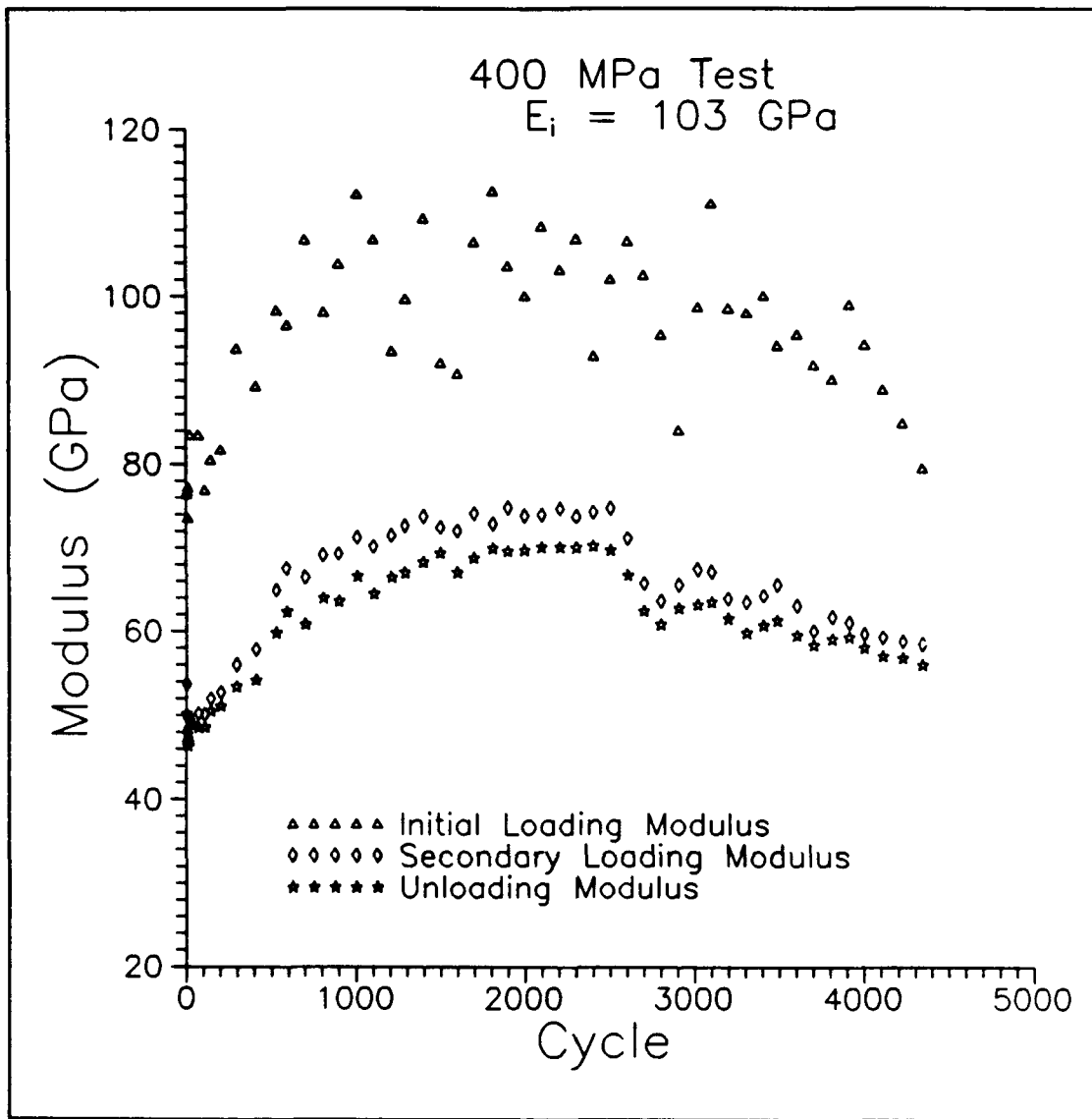


Figure 26. Modulii for 400 MPa Test

is a gradual decline in all three modulii until failure. Appendix A contains modulii plots on a logarithmic cycle axis which more clearly shows the early stiffness loss. The stiffness does not abruptly decline as failure approaches which indicates a sudden fracture. The 450 MPa test did not exhibit a gradual stiffness decrease after the hardening

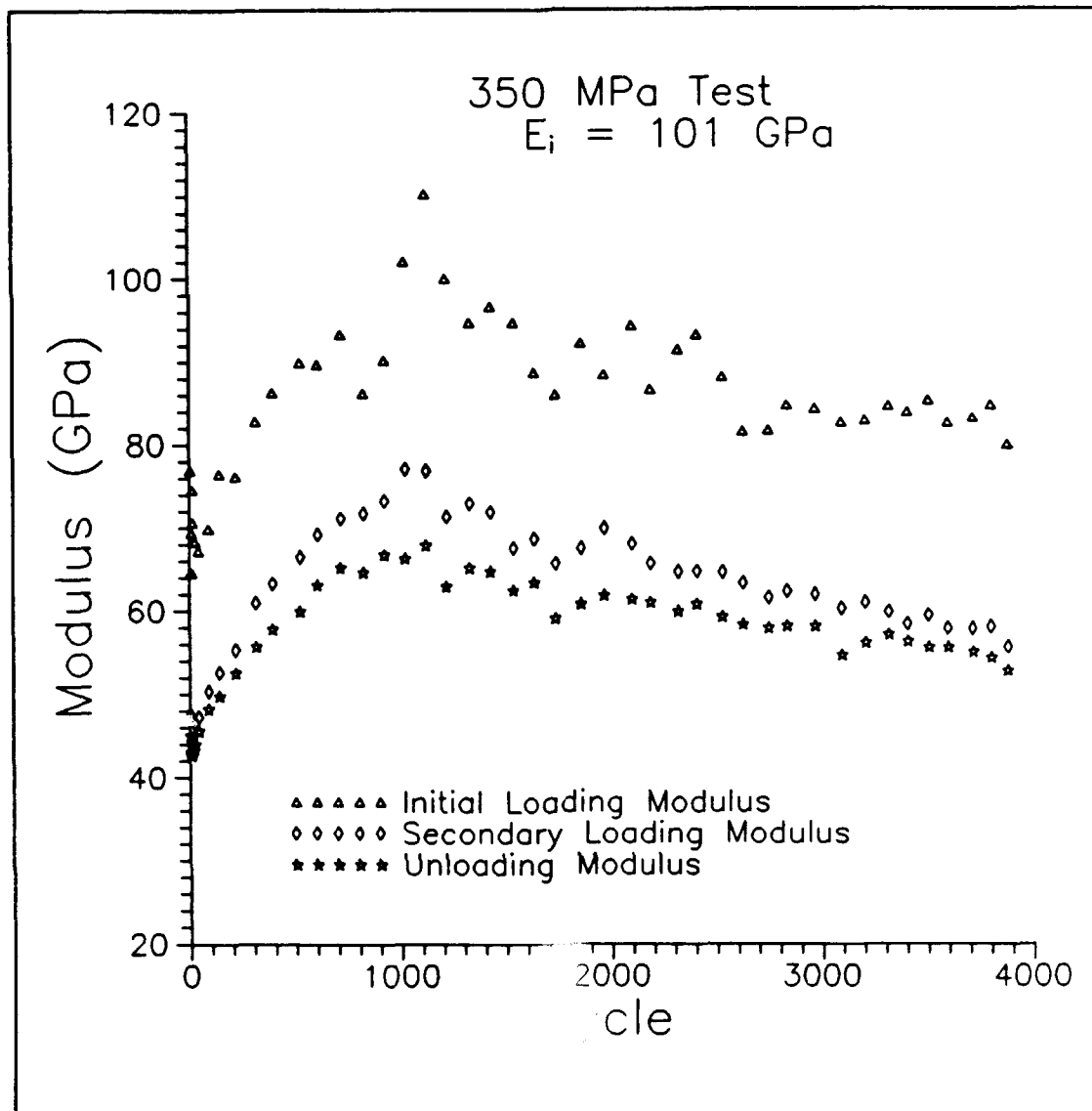


Figure 27. Moduli for 350 MPa Test

period, rather the specimen exhibited constant and steady unloading modulus behavior until failure. Due to the highly non-linear behavior, loading moduli could not be calculated reliably for this specimen.

This general trend of a drop in stiffness, followed by a rapid increase and then gradual decrease in stiffness was

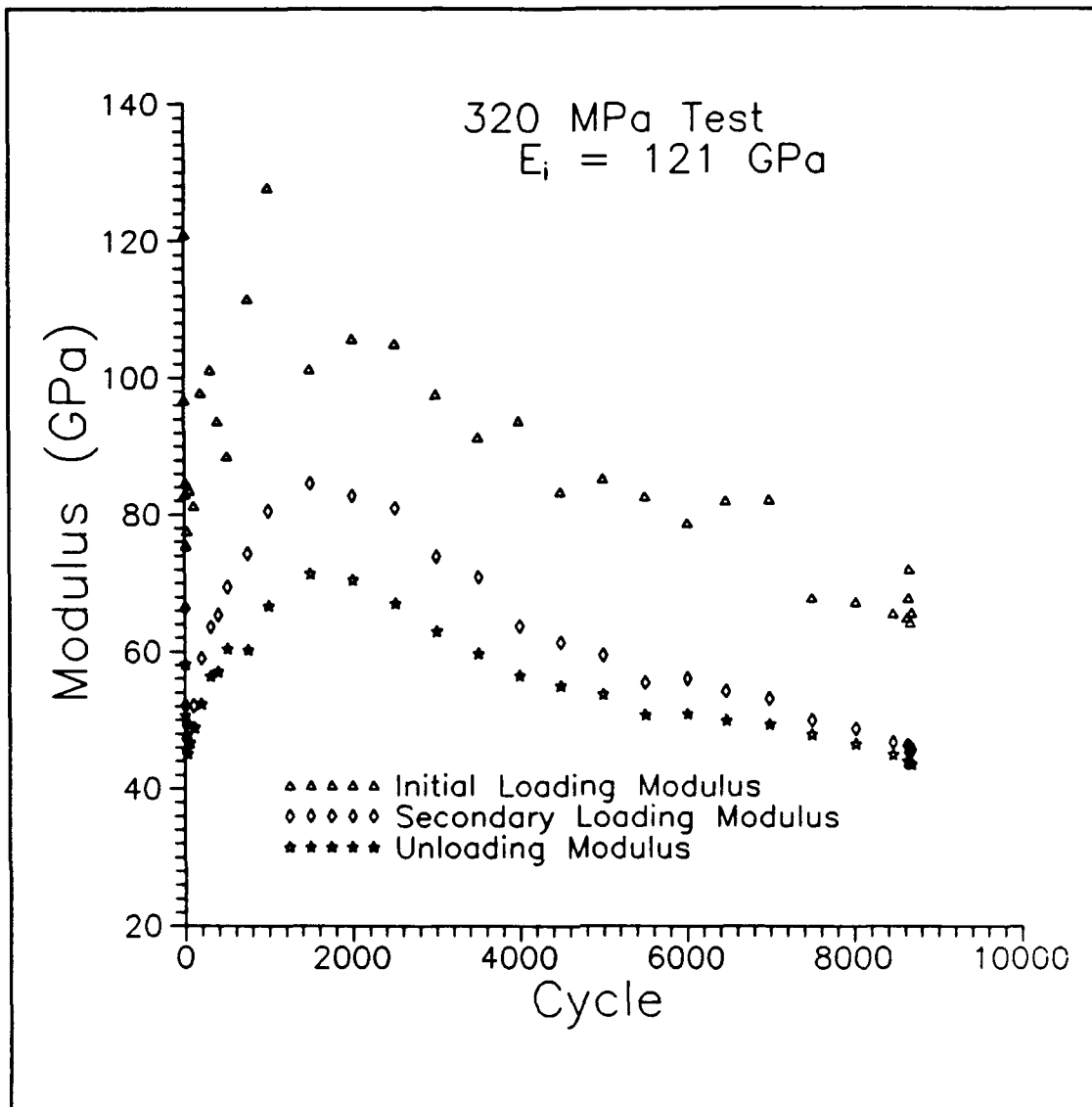


Figure 28. Modulii for 320 MPa Test

also observed by Schubbe in TMF characterization of an as-received SCS-6/Ti-15-3 $[0/90]_{2s}$ laminate (26:72-74). Schubbe attributed the stiffness change to the combined effects of plastic strain hardening and age hardening.

In each modulii plot, the initial loading modulus shows a large band of scatter with the modulus varying widely

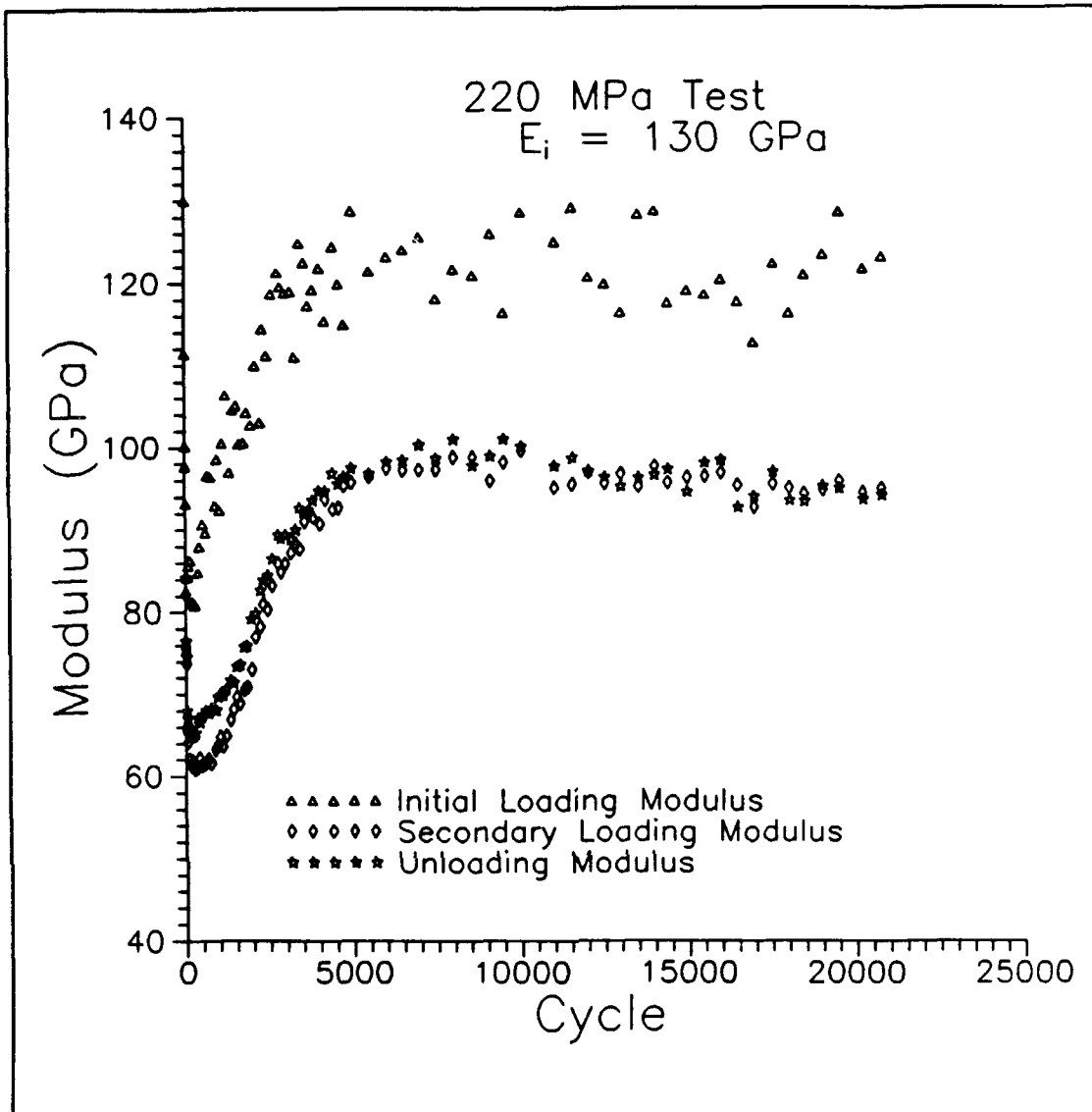


Figure 29. Modulii for 220 MPa Test

between cycles; the general trends, however, are preserved. The other two modulii, on the other hand, exhibit very few drastic fluctuations and tend to map a smoother curve. Because of their more consistent nature, the secondary loading modulus or the unloading modulus could be

effectively used to represent the material response to thermomechanical cycling.

Damage Analysis

Physical damage to the laminate was characterized using three methods. During TMF testing, edge replicas were taken from the 400 MPa, 350 MPa, 320 MPa and 220 MPa specimens. Edge replicating was not performed during the IF test or during the 450 MPa TMF test. After failure, specimen sections were examined using a metallograph and the fracture surfaces were examined using a scanning electron microscope (SEM).

Before specimens were prepared for fracture analysis, an X-ray was taken to reveal any fiber rotation which may have occurred during testing. Fiber rotation was a possibility due to the large longitudinal plastic strains and the related necking. Each failed specimen was then sectioned near the fracture surface into four pieces which could be individually examined. The fracture surface was cut off to a size suitable for the SEM and saved for later SEM examination. A transverse cut just behind the fracture surface and a longitudinal cut through the fracture surface was made. The longitudinal cut yielded two sections: one for through the thickness examination and the other for examination of the top face surface. Figure 30 shows a schematic of the section cuts. When the outer layer of matrix material was ground away from the face section, the entire length of the

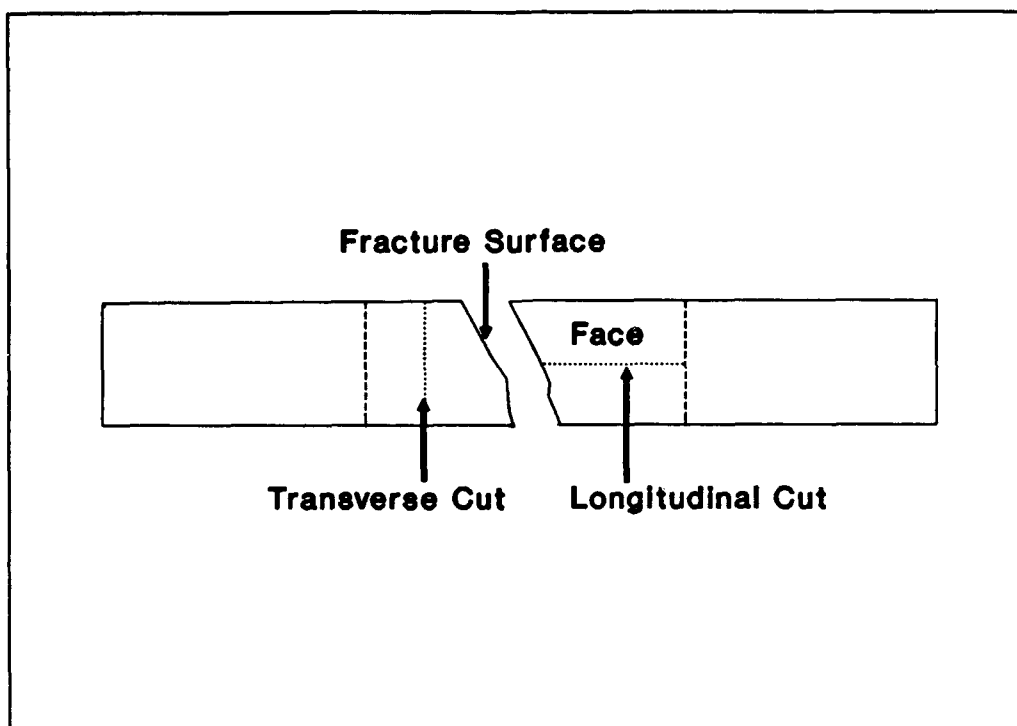


Figure 30. Schematic of Sectioned Specimen

fiber was exposed which could be examined for fiber cracks; the other cuts revealed only elliptical cross sections of the fiber. After cutting, this top surface section was further aged at 427 C in vacuum for 24 hours. This post-test heat treatment technique reported by Lerch (16) discontinuously precipitates fine particles on slip bands which are highlighted using a chemical etchant. Heretofore, slip bands were not easily revealed by chemical etchants. All specimens were mounted in a thermoplastic mounting compound and polished down to a half micron finish.

All specimens were carefully observed for matrix and fiber cracking, reaction zone changes and fiber-matrix debonding using a metallograph. Next, all specimens were

etched. The transverse and longitudinal thickness sections were etched in Kroll's, a weak nitric-acid-based etchant. The face section was etched in a 3 percent aqueous solution of ammonium bifluoride. Again, each section was examined on the metallograph for slip bands, α -phase precipitates and crack interaction along grain boundaries.

Isothermal Fatigue Test. The test specimen failed in the gauge length and experienced a ten percent reduction in cross sectional area at the fracture due to necking. The fracture surface was dull and dark and angled at approximately 45 degrees. An X-ray of the specimen revealed fiber rotation near the fracture surface averaging 6.5 degrees. Figure 31 is a photograph from the X-ray. The darker lines are the molybdenum crossweave. The amount of fiber rotation was determined by measuring the change in the angle between fibers in adjacent plies. The angle prior to testing for a $[\pm 45]_2$ laminate is 90 degrees. The lines of fibers intersecting near the fracture were extended onto paper using a straight edge and the angle from the horizontal measured. The change in the angle from 90 degrees corresponded to the fiber rotation. This method was performed several times and the results averaged for the final value of the fiber rotation.

Metallographic examination of the sectioned specimens revealed fiber-matrix interface failures and deformed matrix material around the debonded areas. Matrix cracking was prevalent near the fracture, but more fiber damage was



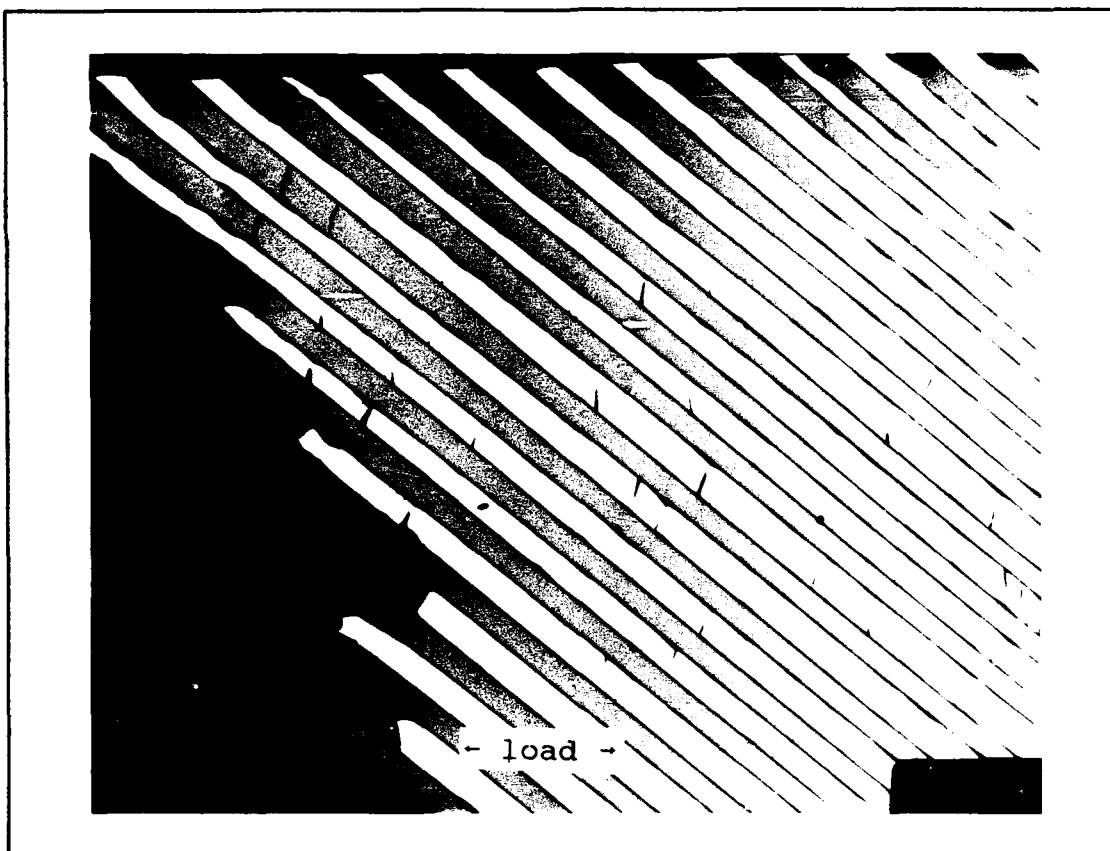


Figure 32. Face Section of the IF Test Specimen (32x)

associated with these areas, since the local stresses are high enough to cause yielding. Figure 33 shows the matrix necking and related cracking and debonding after fracture in greater detail. Etching of the top surface revealed slip bands in the matrix. Slip bands are conclusive evidence of plastic flow in the matrix. Intersecting slip bands, indicative of slip on multiple slip systems, are depicted in Figure 34.

SEM analysis of the fracture surface revealed a fracture surface dominated by ductile characteristics. Figure 35 shows a SEM photograph from the fracture surface. The

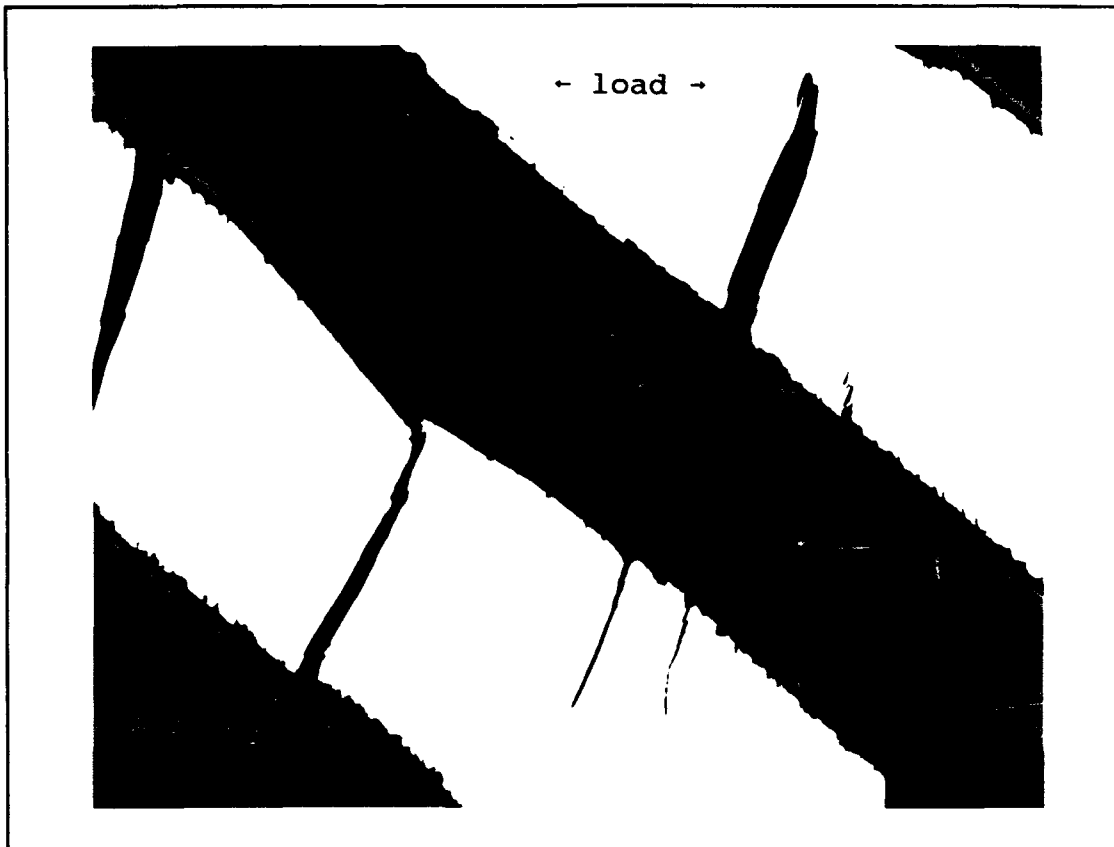


Figure 33. Matrix Cracking in the IF Test Specimen (300x)

matrix material around fibers is extensively deformed and shear lips have formed. The shear lips indicate continuous plastic stretching of the matrix until failure. Closer examination of the lips between fibers revealed a dimpled surface, a common characteristic of plastic flow. Extensive fiber pullout can also be observed.

The characteristics of high temperature tensile overload revealed by this test include fiber-matrix failure, matrix deformation around the debonded fiber, a small amount of matrix cracking, fiber rotation, slip bands in the matrix

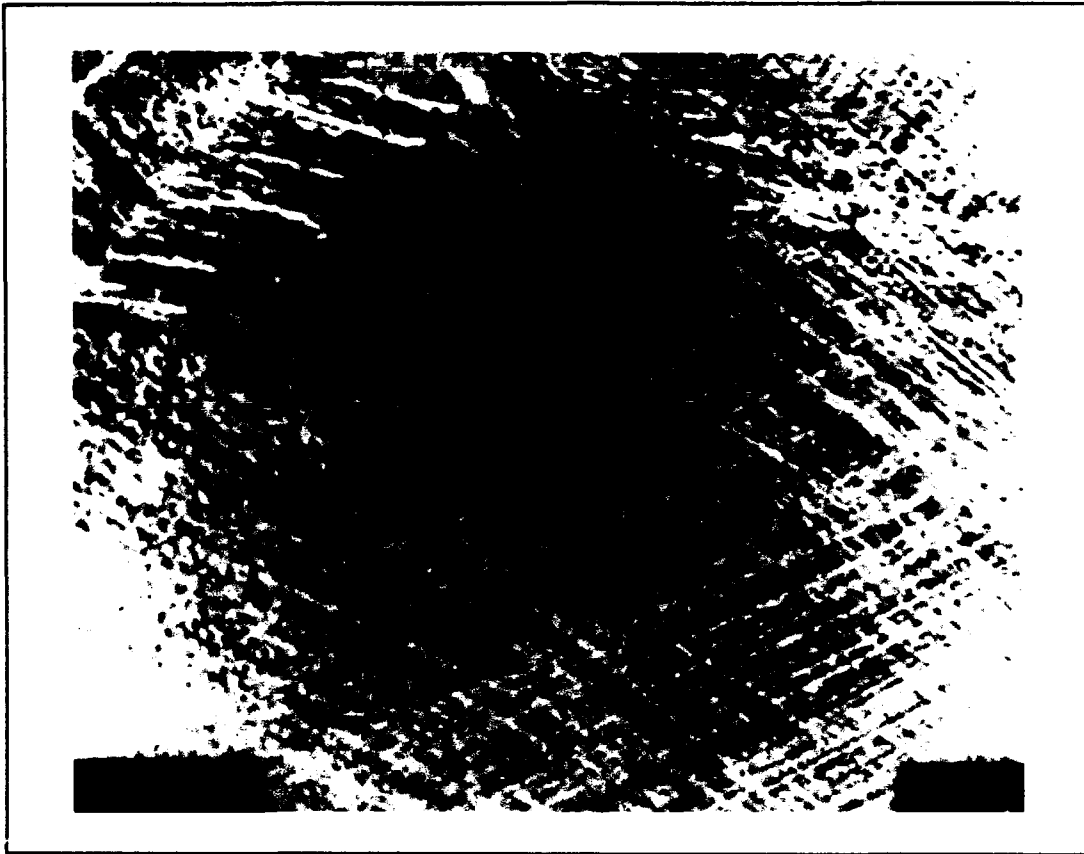


Figure 34. Intersecting Slip Bands in the IF Test Specimen (1500x)

and a fracture surface dominated by shear lips, matrix dimpling and fiber pullout.

Thermomechanical Fatigue Tests.

Edge Replicating. Edge replicas proved to be of limited value in attempting to correlate physical damage to the progression of fatigue in a specimen. As will be discussed later, fatigue damage appeared to initiate in the interior of the specimen and progress out toward the faces and edges. Replicas gave only detailed impressions of the surface at the edge. Nonetheless, the replicas did provide

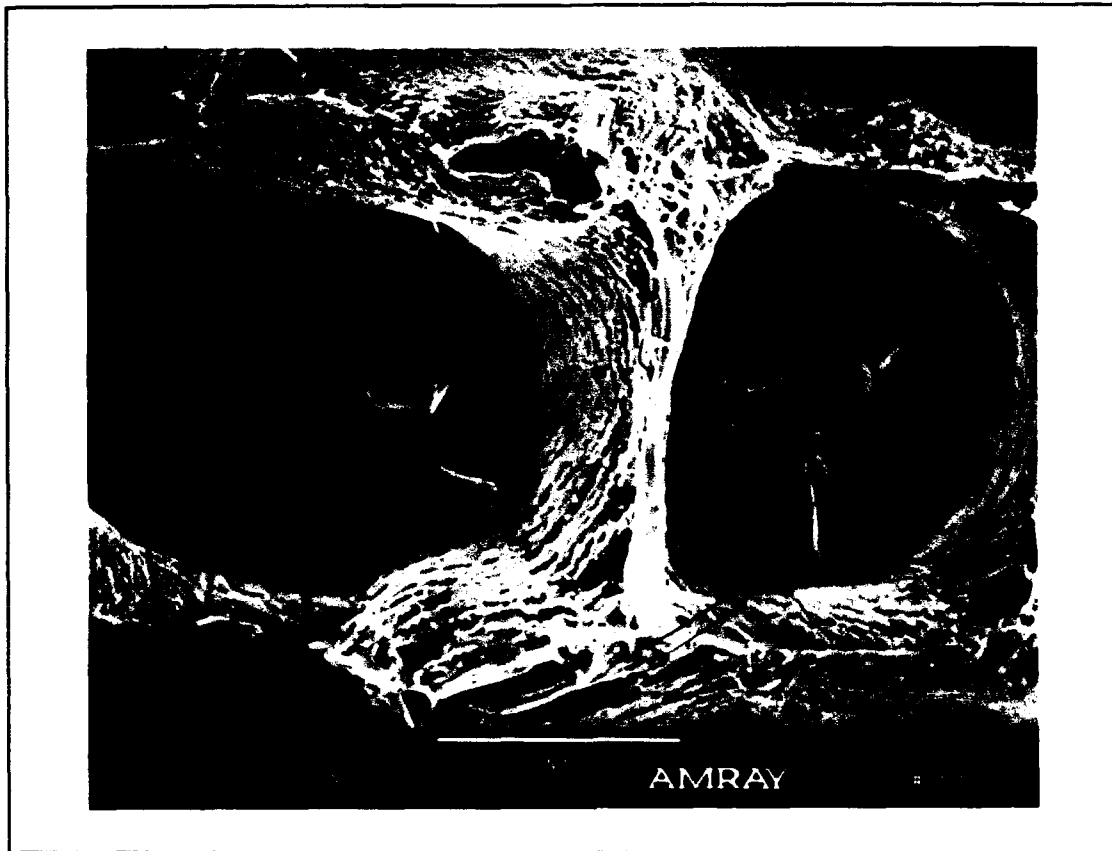


Figure 35. Ductile Fracture Surface of the IF Test Specimen

a record of the type of edge damage occurring at the different stress levels. A sequence of edge damage development common to all TMF specimens was revealed by the edge replicas.

Replicas taken after the first ten thermomechanical cycles revealed debonding between the fiber and matrix for all specimens. Depending on the applied stress level, the debonding was often accompanied by other types of damage (matrix deformation and cracking), but the fiber-matrix debonding seemed to be the initial sign of laminate damage.

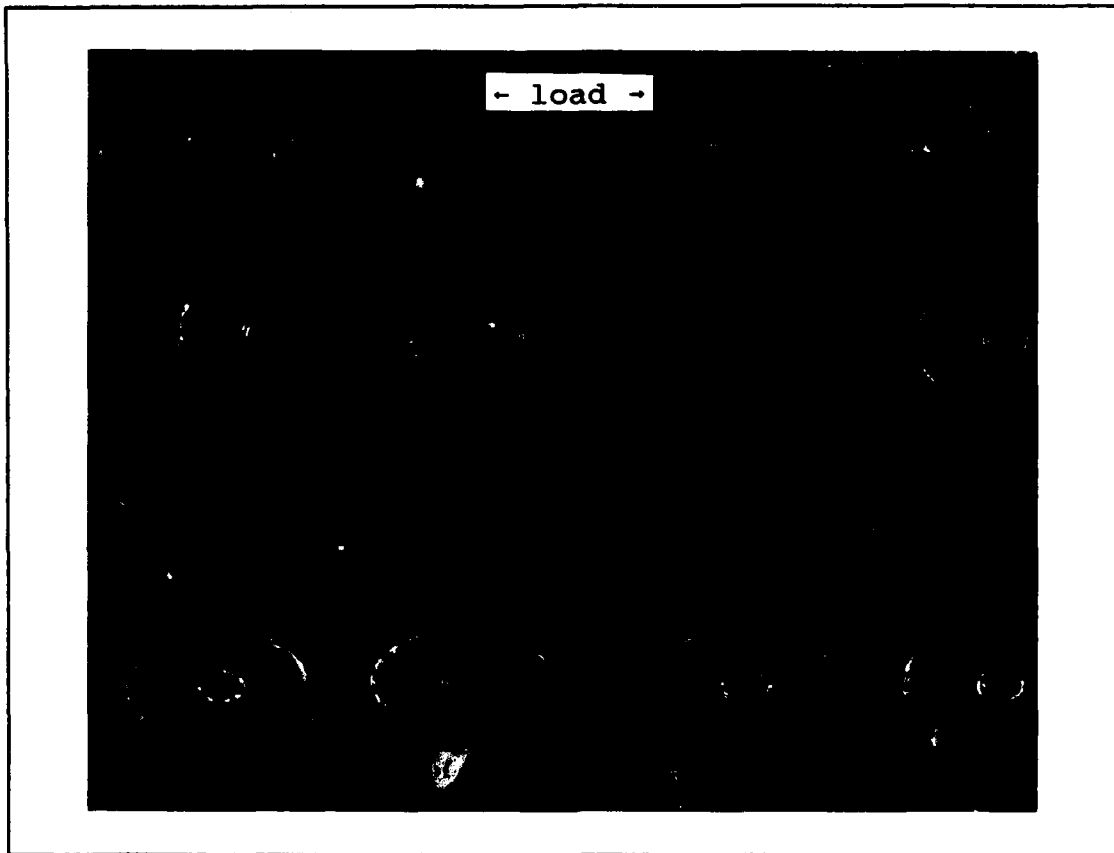


Figure 36. Edge Replica with Debonded Fibers

Figure 36 shows a replica photograph from the 320 MPa test after 11 cycles. Debonding is revealed by the light colored outline around the core of the fiber and around the fiber-matrix interface; no matrix cracking is visible. It can safely be assumed that debonding occurred throughout the laminate and not just at the edges. After additional cycling, further damage was evidenced by elongation of the matrix around the fiber in the load direction and very small radial cracks emanating from the reaction zone transverse to the load. Fiber rotation evidence was also seen after debonding. Figure 37 shows fibers in a single ply in the

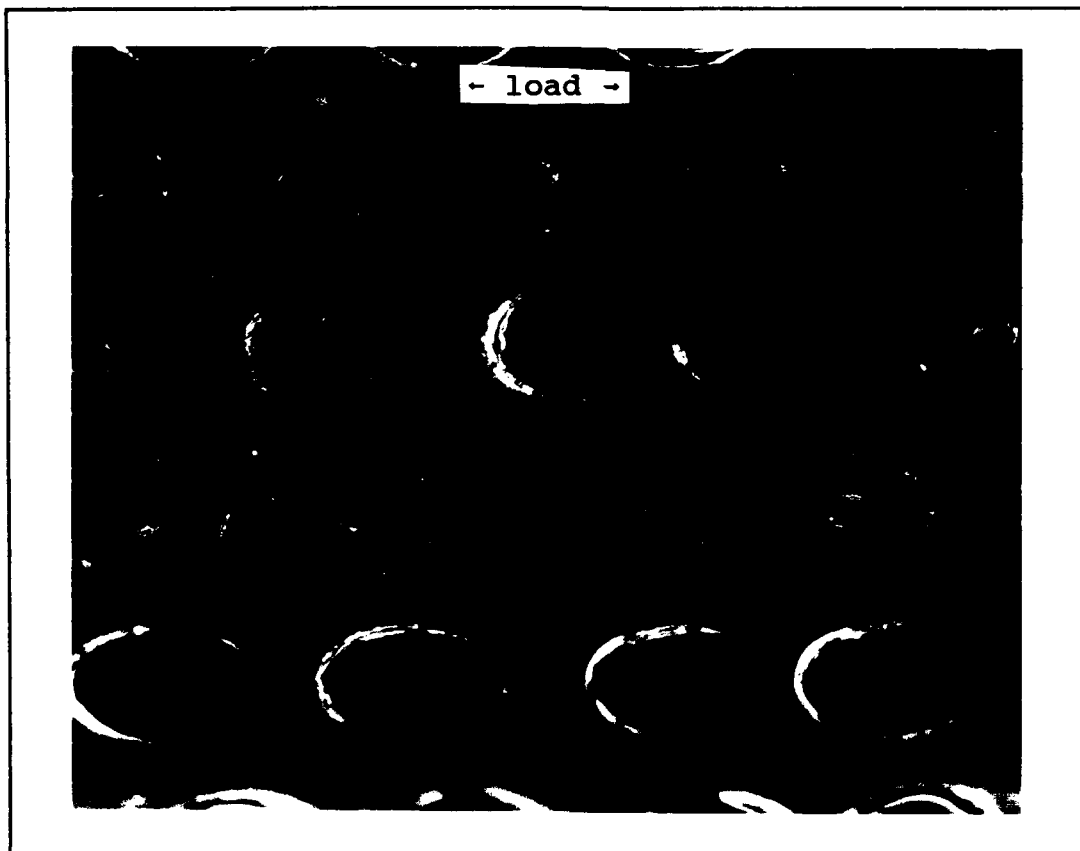


Figure 37. Edge Replica with Recessed Fibers in a Ply

320 Mpa specimen after 380 cycles which have recessed into the laminate due to fiber rotation as discussed earlier. The resulting hole at the surface shows up as a bubble on the replica. Further cycling results in more fiber recession and growth of the transverse micro-cracks in the matrix. The cracks grow radially from the reaction zone, coalesce and interact with microcracks growing from other fibers in adjacent plies. Figure 38 shows transverse micro-cracks growing from the fiber-matrix reaction zone in the 350 MPa specimen after only ten cycles. Extensive transverse cracking between plies was visible over the entire

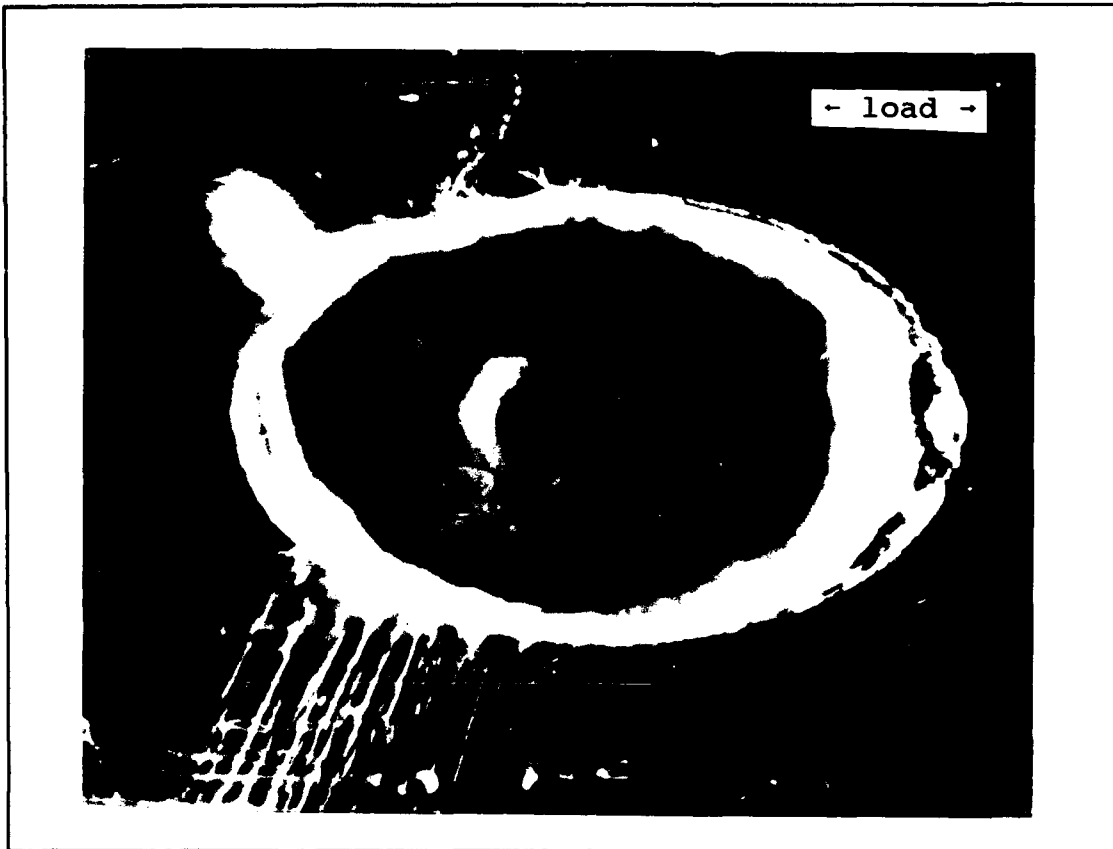


Figure 38. Edge Replica with Transverse Matrix Cracking

gauge length of all specimens which failed. Conversely, edge replicas from the 220 MPa test stopped at 21,000 cycles revealed only slight longitudinal cracks along ply boundaries; no transverse cracking between fibers was visible. Figure 39 shows longitudinal cracking between two fibers in the 220 MPa test after 5600 cycles.

Edge replicas reveal that fiber-matrix interface failures were the first damage to occur, followed by transverse microcracking initiating at the reaction zone and matrix deformation around debonded fibers. Evidence of fiber

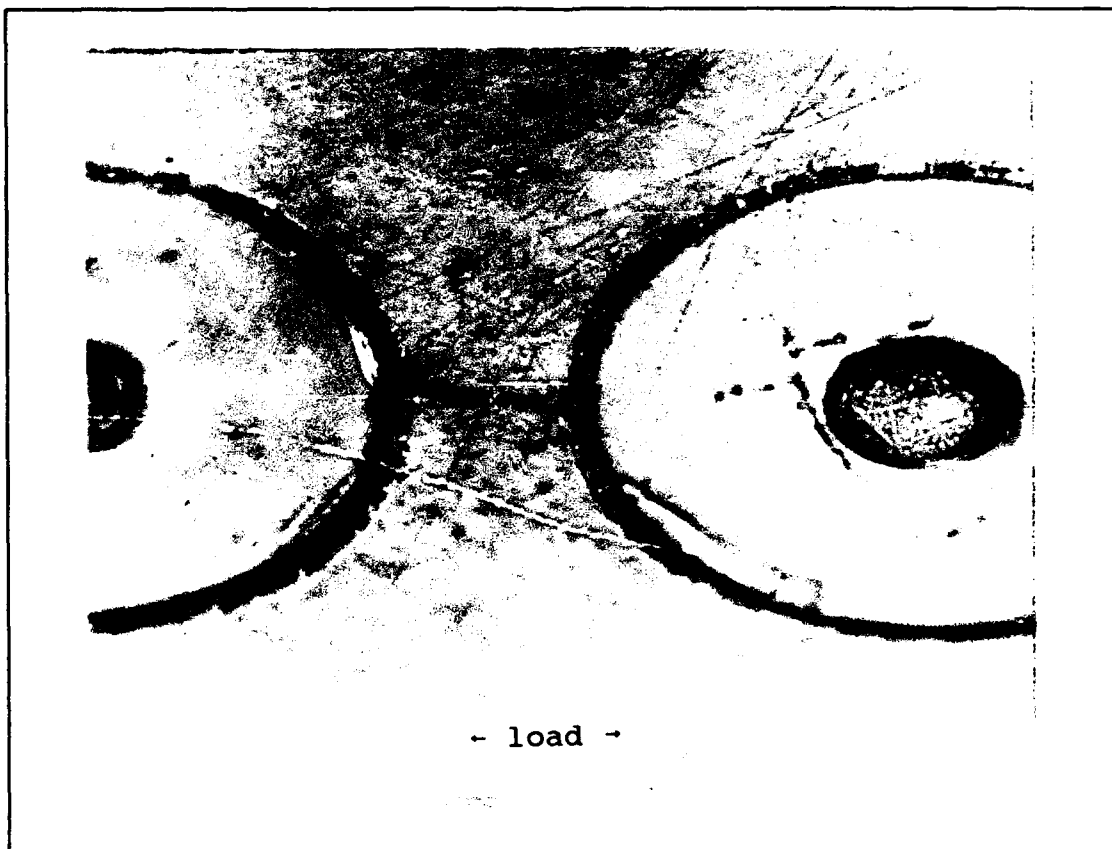


Figure 39. Edge Replica with Longitudinal Matrix Crack

rotation suggests that rotational effects are not uniform throughout the laminate but may vary between individual plies. Edge replicas provide only a limited description of the fatigue damage and additional analysis must be used to understand the progression of damage.

Fracture Analysis. Metallographic and SEM analysis was performed on each TMF test specimen as described earlier. The failed specimens possessed common characteristics which indicated that the same mechanisms dominated failure regardless of applied stress.

All specimens failed in the gauge length except the 400 MPa specimen which failed well outside the heat zone. The fracture surfaces of the 450 MPa and 320 MPa test specimens were relatively flat through the mid-section and angled at the edges. The 400 MPa and 350 MPa test fractures were angled over the entire surface. All fracture surfaces, except the 320 MPa specimen, contained two distinctly colored regions. At the edges the fracture surface was dark and dull in color (like the IF specimen), while the middle was noticeable brighter. Fiber rotation was present in all specimens and averaged between five and six degrees for the failed specimens at the fracture. Fiber rotation in the 220 MPa test averaged only two to three degrees in the gauge length. Obvious necking and surface cracks were also common in the gauge length for all failed specimens.

Metallographic examination revealed extensive debonding and deformation at the fiber-matrix interface. The reaction zone between the fiber and matrix increased noticeably during testing and often experienced cracking and deterioration. Figure 40 shows the degraded reaction zone around a fiber after failure from the 350 MPa test. This embrittled region was the initiation site of the majority of the matrix cracks. Similar to the cracks seen in edge replicas, transverse matrix cracks often extend from fiber to fiber, bridging adjacent plies. In general, fiber damage was minimal, except for debonding of the carbon core and fiber cracking confined to the regions close to the fracture surface.

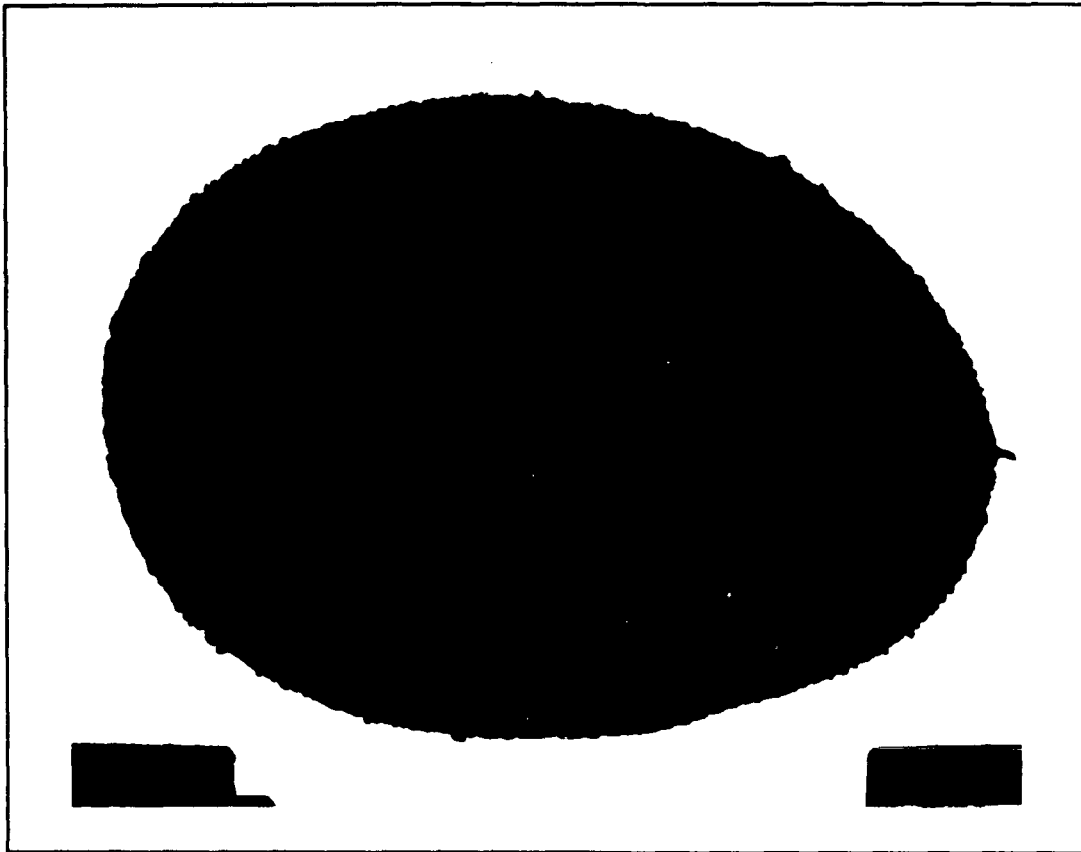


Figure 40. Degraded Reaction Zone (500x)

Fiber rotation was evidenced in all test specimens from the fibers pulling into the laminate away from the edge. The dominant form of damage in all failed specimens was transverse matrix cracking initiating at the fiber-matrix interface. Matrix cracking occurred throughout the gauge length and seemed confined to the interior of the specimen; there was no evidence of fatigue matrix cracking at the edges and faces.

Figure 41 shows the extensive matrix damage in the 350 MPa test specimen typical of all specimens at failure.

Figure 42 shows in detail transverse cracks growing from

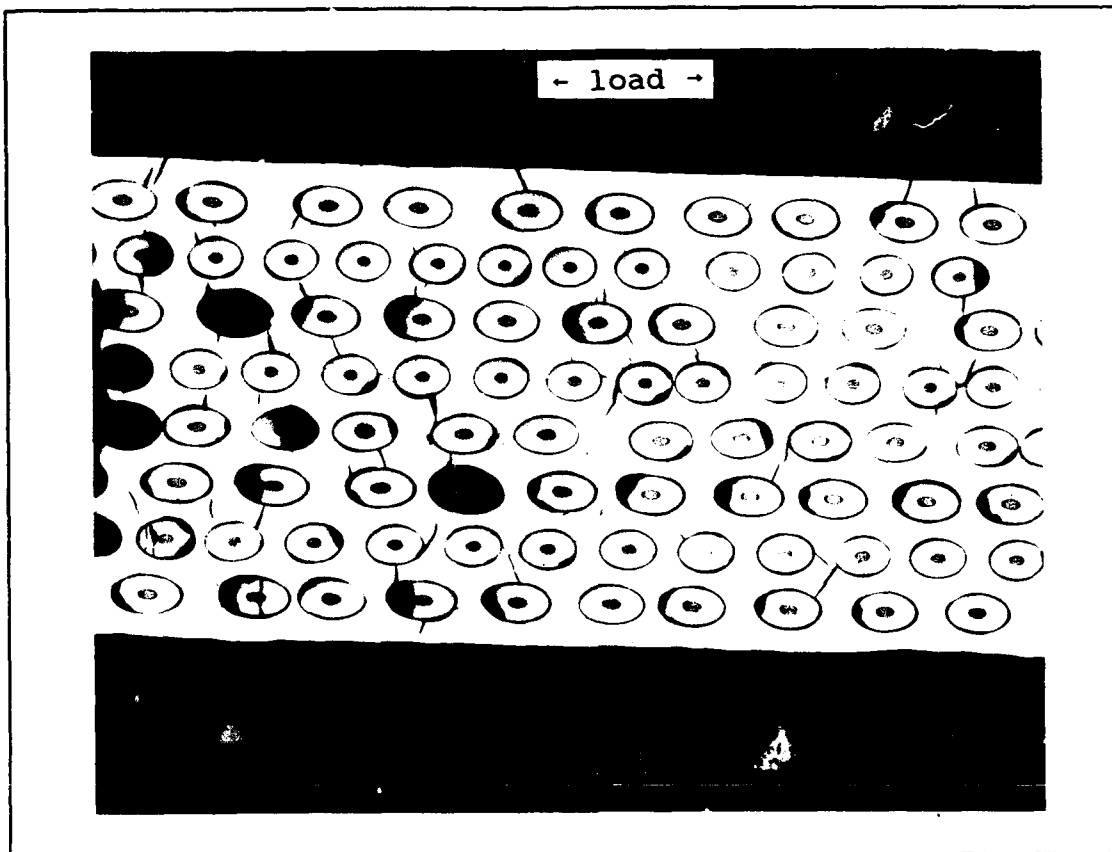


Figure 41. Typical Transverse Matrix Cracking (32x)

fiber reaction zones in the 320 MPa specimen. Though transverse matrix cracking was dominant, evidence of small longitudinal cracks on the edge, emanating radially from reaction zones along ply boundaries, was found in the low stress TMF tests (320 MPa and 220 MPa). Figure 43 shows typical longitudinal cracking from the 320 MPa test specimen.

The sectioned face specimens ground down to expose the first ply fibers revealed damage similar to that seen in the IF specimen. Fiber cracking was prevalent near the fracture surface but decreased away from the fracture. Matrix necking and cracking was not confined to the fracture, but was

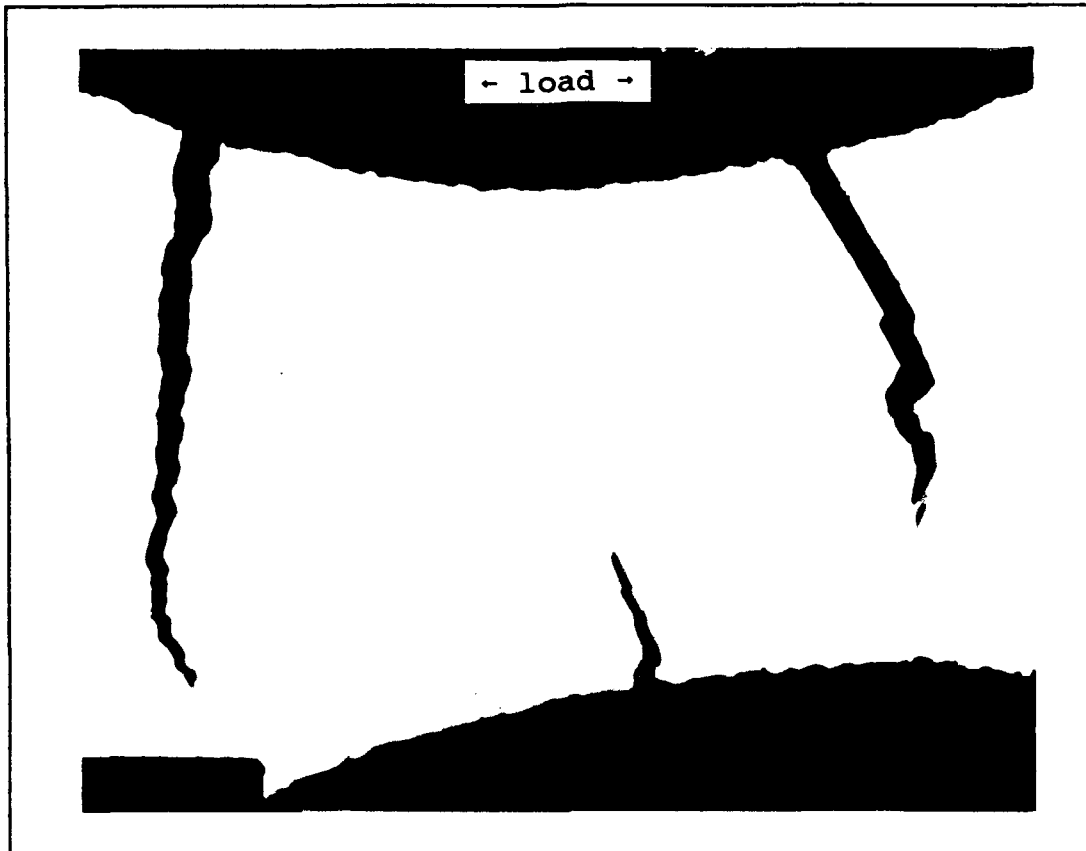


Figure 42. Typical Transverse Matrix Cracks Emanating from Damaged Reaction Zones (1000x)

common throughout the gauge length. Figure 44 shows typical fiber cracking from the 400 MPa test specimen near the fracture. Matrix necking where debonding and high stresses led to matrix plasticity, is seen between every fiber. The fibers pulling into the laminate along the edge is also shown in the figure. Figure 45 shows the matrix necking and debonding and an associated fiber crack near the fracture in greater detail. Notice that the crack occurs along the molybdenum crossweave line and that deformation in the matrix is restricted by the crossweave next to the fiber.

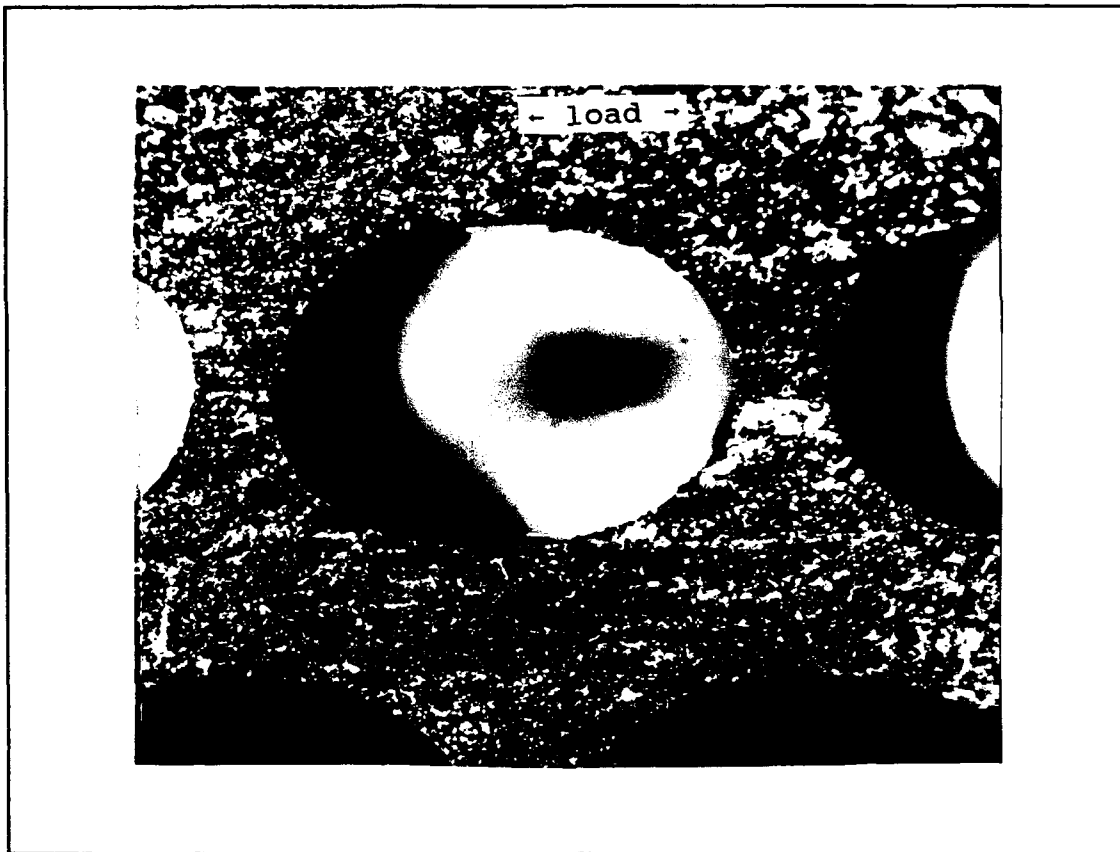


Figure 43. Typical Longitudinal Matrix Cracking along a Ply Boundary (300x)

As expected from the large amounts of plastic deformation, slip bands were easily found in all specimens. In the 450 MPa test specimen, very dense concentrations of slip bands were found in the matrix. In the 400 and 350 MPa test specimens, numerous intersecting slip bands were observed but not in dense concentrations as in the 450 MPa specimen. Figure 46 shows intersecting slip bands from the 350 MPa test. The bands run along a 45 degree angle from the loading axis where the shear stress is maximum and are contained within the grain boundary. The 320 MPa specimen exhibited

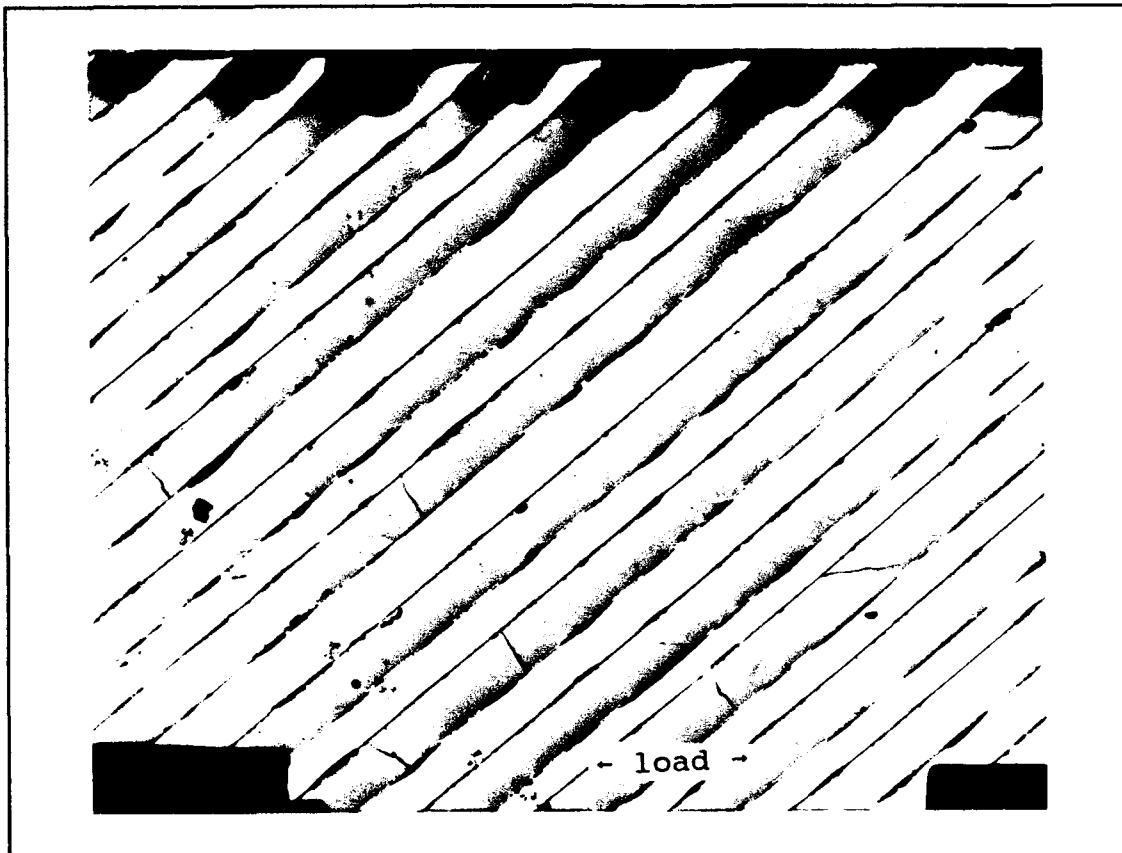


Figure 44. Typical Fiber Cracking (50x)

small slip bands confined to the matrix region very near the reaction zone. Figure 47 shows the small slip bands in the matrix directed perpendicular to the fiber.

SEM analysis of the fracture surface revealed distinct fracture regions which corresponded to the dull and bright regions on the surface. The 450 MPa, 400 MPa and 350 MPa specimens contained these two regions. For these specimens, the outer edges were dull, similar to the IF fracture surface. SEM examination revealed fracture characteristics identical to those seen for tensile overload in the IF specimen. Fiber pullout and dimpled shear lips between

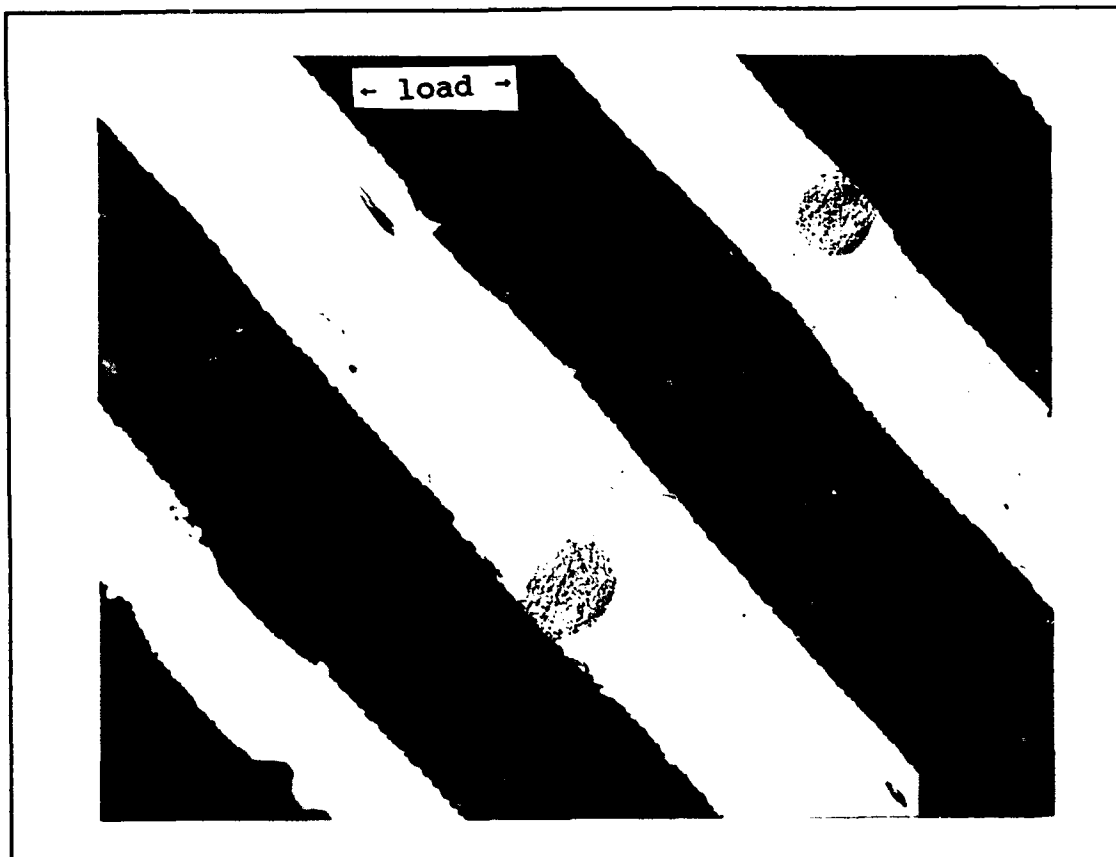


Figure 45. Typical Matrix Necking along Debonded Fibers
(200x)

fibers characterize the ductile failure in this region. Figure 48 shows typical ductile regions in the 450 MPa and 400 MPa specimens. The bright mid-region made up the majority of the fracture surface for these three specimens. The fracture here is drastically different than the ductile fracture on the edges. The surface is characterized by a crystallographic cleavage fracture between fibers. Cleavage occurs due to breaking of atomic bonds along a preferred crystallographic plane and is associated with a brittle fracture containing relatively flat and reflective surfaces.



Figure 46. Intersecting Slip Bands within a Grain in the 320 MPa Test Specimen (1000x)

There are no shear lips or indications of plastic dimpling. on the fracture surface. This indicates a brittle fracture likely caused by fatigue crack growth. Figure 49 shows typical cleavage fracture regions in the 450 MPa and the 320 MPa specimens. Fiber pullout is seen, but not to the extent as occurred in the ductile regions. Debonding, deformation of the matrix around fibers and degradation of the fiber carbon coating was also observed. The two fracture regions in the 450 MPa, 400 MPa and 350 MPa specimens were very distinct and there was no mixing of brittle and ductile

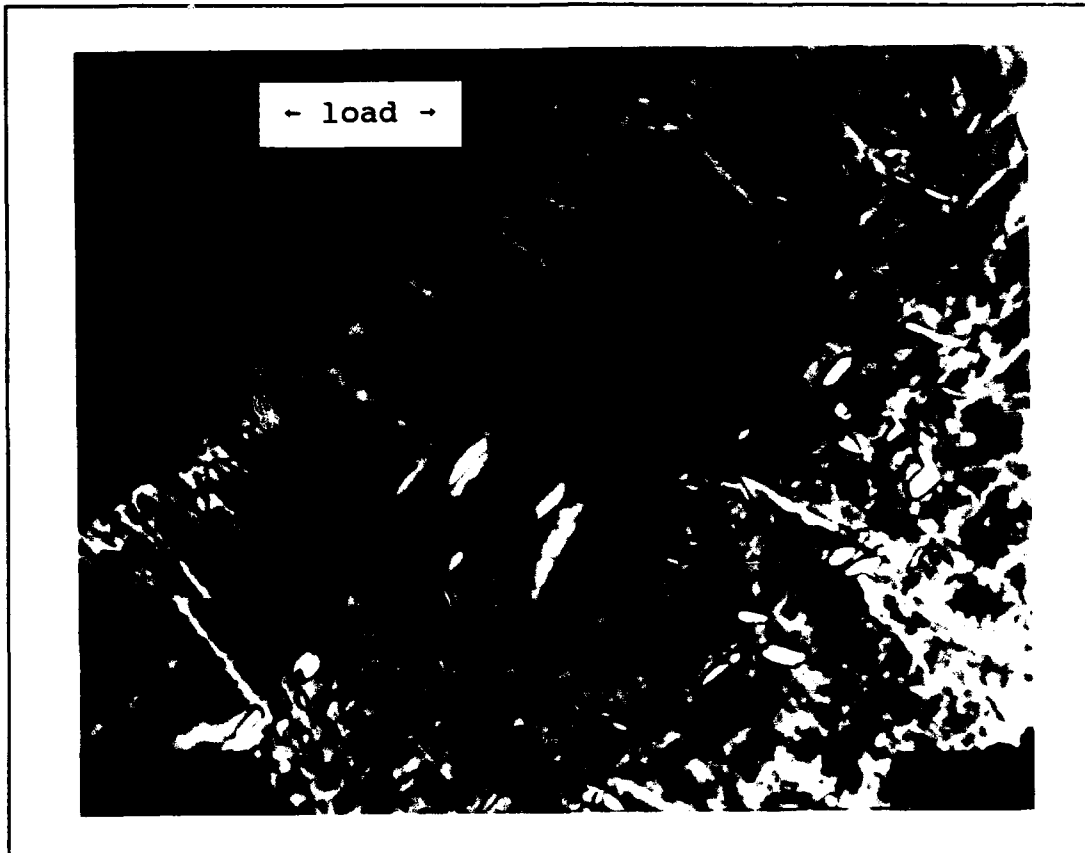


Figure 47. Slip Bands in the 320 MPa Test Specimen (1500x)

modes. The 320 MPa specimen, however, did show mixed regions of both ductile and brittle fracture. The fracture surface was dominated by cleavage fracture and did not exhibit a distinct tensile overload region. This specimen had the longest fatigue life and consequently its fracture surface exhibited the most fatigue crack growth damage. Figure 50 shows the mixed ductile and brittle regions in this specimen.

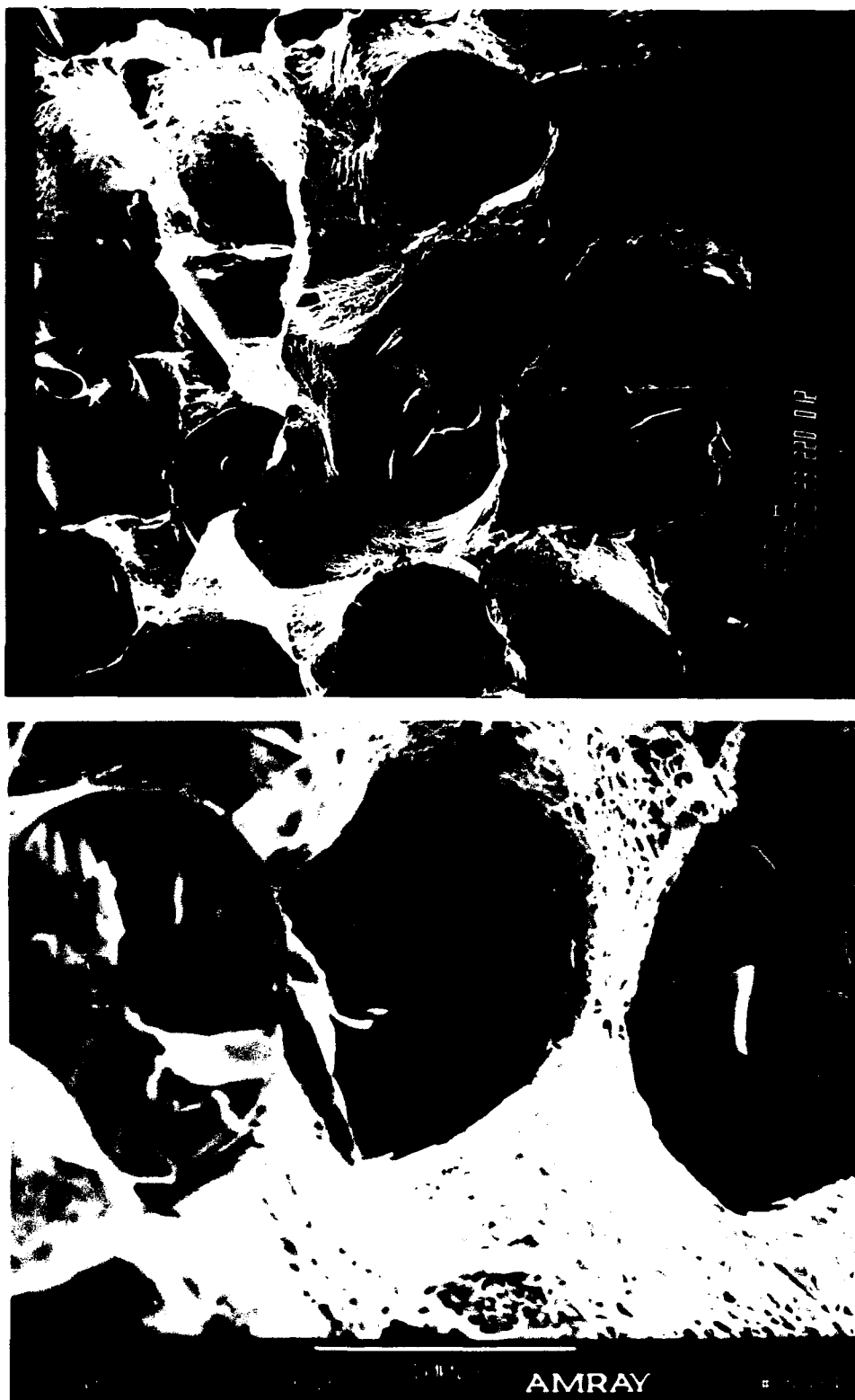


Figure 48. Typical Ductile Fracture Surfaces from the 450 MPa (top) and 400 MPa (bottom) Test Specimens

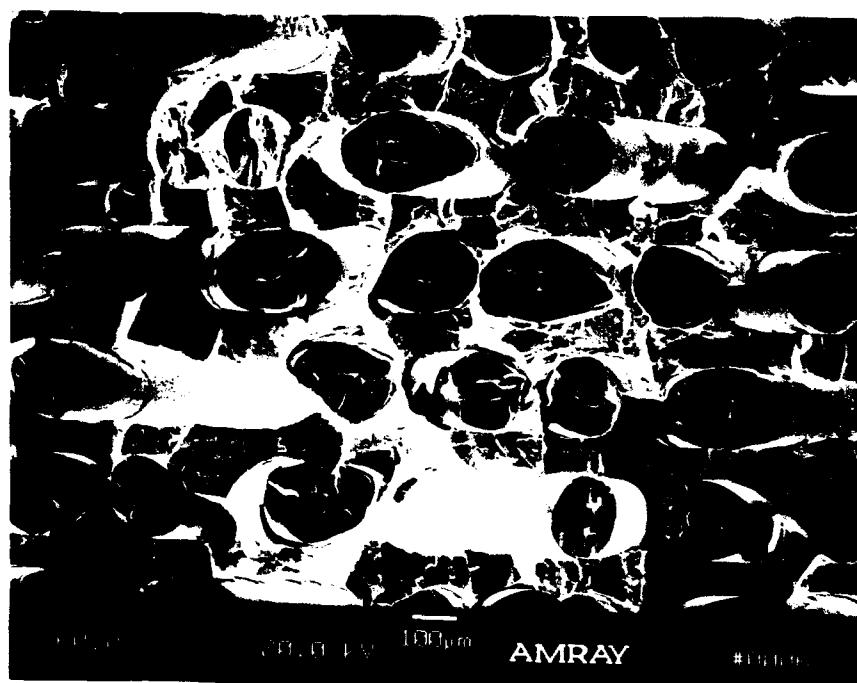


Figure 49. Typical Cleavage Fracture Surfaces from the 450 MPa (top) and 320 MPa (bottom) Test Specimens

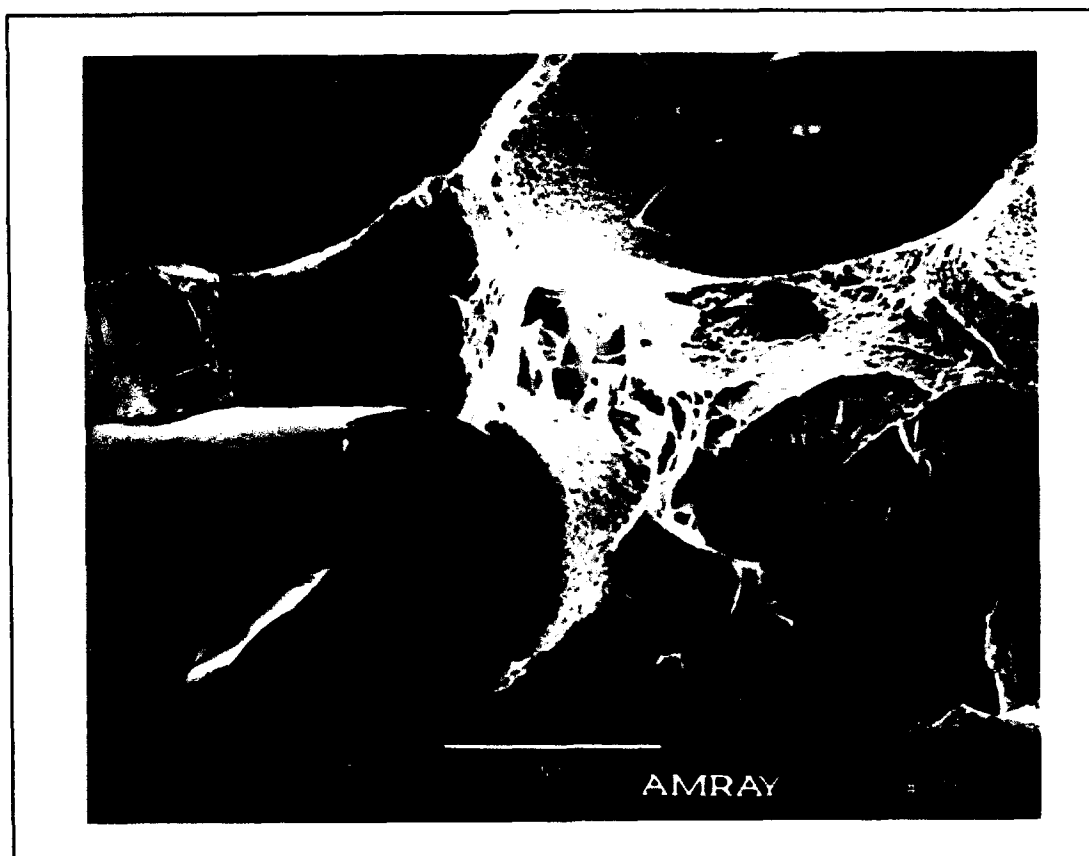


Figure 50. Fracture Surface with Mixed Brittle and Ductile Failure Regions

Composite Microstructure. The microstructure of the matrix was revealed by etching polished sections. As discussed earlier, Ti-15-3 is a metastable beta alloy which precipitates the more stable α -phase during heat treatment. Needle-like α -precipitates are common for the heat treatment used in this study. Metallographic examination of etched specimens revealed an apparent difference in microstructures between untested and tested sections. After aging, large needle precipitates of α -Ti were distributed evenly throughout the matrix, except for precipitate lean zones

immediately surrounding the fibers and between fibers spaced too closely together. A different and more numerous type of precipitate was observed in the tested specimens. Besides the large α -Ti needles, a finer precipitate also seemed to be present. The small precipitate was especially common along ply boundaries between closely spaced fibers. The apparent finer precipitates suggested continued beta transformation during testing due to the cycling stress or temperature, or some combined effect. Figure 51 shows the microstructure after etching between two fibers in the 320 MPa test specimen after failure; note the precipitate lean zones surrounding the fibers and the slip bands in the matrix. It was not clear, however, if the precipitates were present before testing, were merely an optical illusion caused by pitting of the matrix by the etchant or were indeed additional precipitates. To further investigate the precipitation phenomenon and mechanisms, an additional experiment was conducted during which a specimen was thermally fatigued for 3200 cycles. The modulus increase observed in TMF test specimens occurred over the same range of cycles. The test conditions were identical to the TMF cycle except the tensile load was held constant at five Newtons. The objective was to determine if any stiffening of the laminate occurred during thermal cycling due to continued β -transformation. Schubbe observed an increase in modulus in an as-received $[0/90]_{2s}$ SCS-6/Ti-15-3 laminate after 10,000 thermal cycles (26:52). During thermal cycling

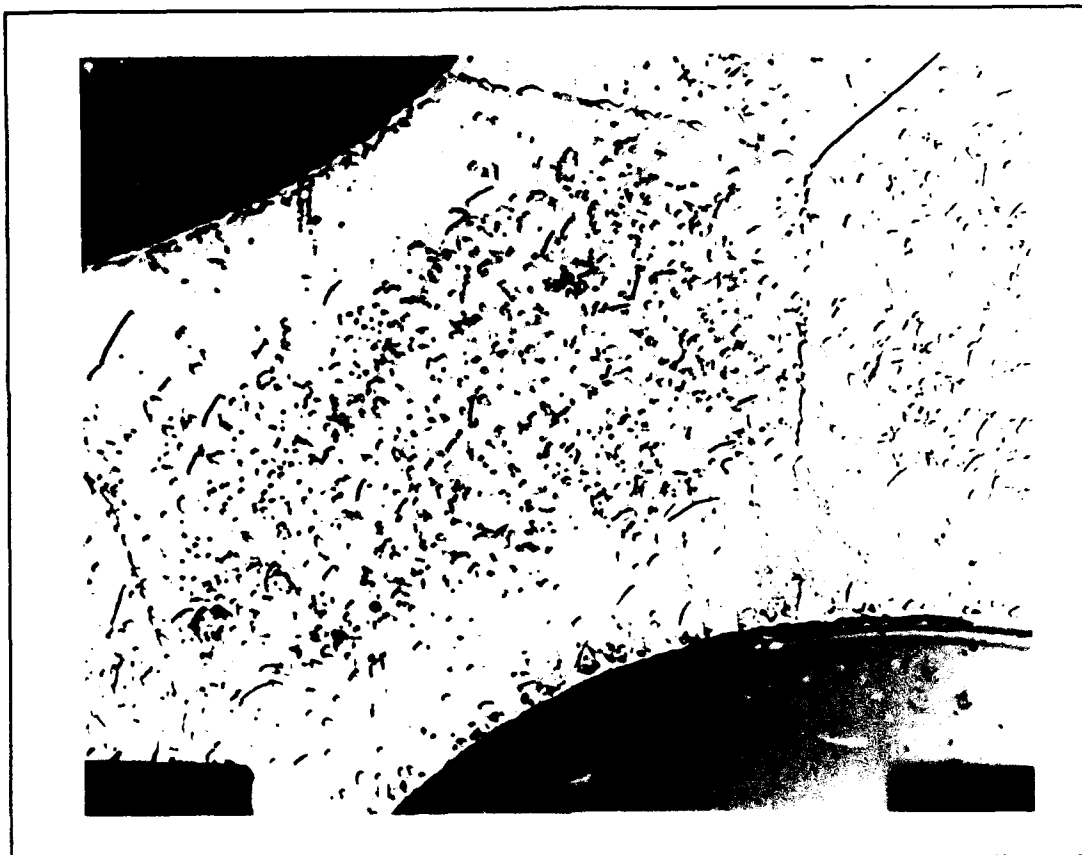


Figure 51. Matrix Microstructure after TMF Testing
(750x)

the initial room temperature loading modulus was calculated after 100, 500, 1000 and 3200 cycles. No significant change occurred in the value of the modulus during testing. After thermal cycling, an untested section cut before testing was compared to a thermally cycled section and a previously tested TMF specimen using backscatter SEM techniques. This technique allowed observation of precipitates without etching by contrasting the matrix and the precipitates based on atomic weight. Composition chemistry of uncycled matrix

metal was analyzed using wavelength dispersive spectroscopy (WDS) and is included in Appendix B.

The microstructure of the thermally fatigued specimen did not reveal any dramatic differences from the untested section. Figure 52 shows the microstructure of the untested and thermally cycled specimens near an outer edge. Both show the characteristic α -Ti needles and smaller precipitates. The smaller precipitates are probably α -Ti needles oriented such that only the cross section is visible or just a more coarse α -precipitate. The thermally cycled specimen appears to have a denser distribution of precipitates than the uncycled specimen, but the amount and type of precipitates are comparable to that typically reported for the composite (15:3). The SEM analysis did not reveal the excessive precipitates along ply boundaries between fibers typically seen after etching. This infers that the matrix near the ply boundary was pitted due to etching which appeared very similar to precipitates through an optical microscope. The TMF specimen also failed to reveal any additional or different precipitates which could be attributed to the thermomechanical cycling.

No conclusive evidence of a change in the microstructure resulting from thermal or thermomechanical cycling was found in any of the three specimens observed using backscatter SEM techniques. The amount and type of precipitates appeared to remain essentially the same after thermal and thermomechanical testing as were present after aging.

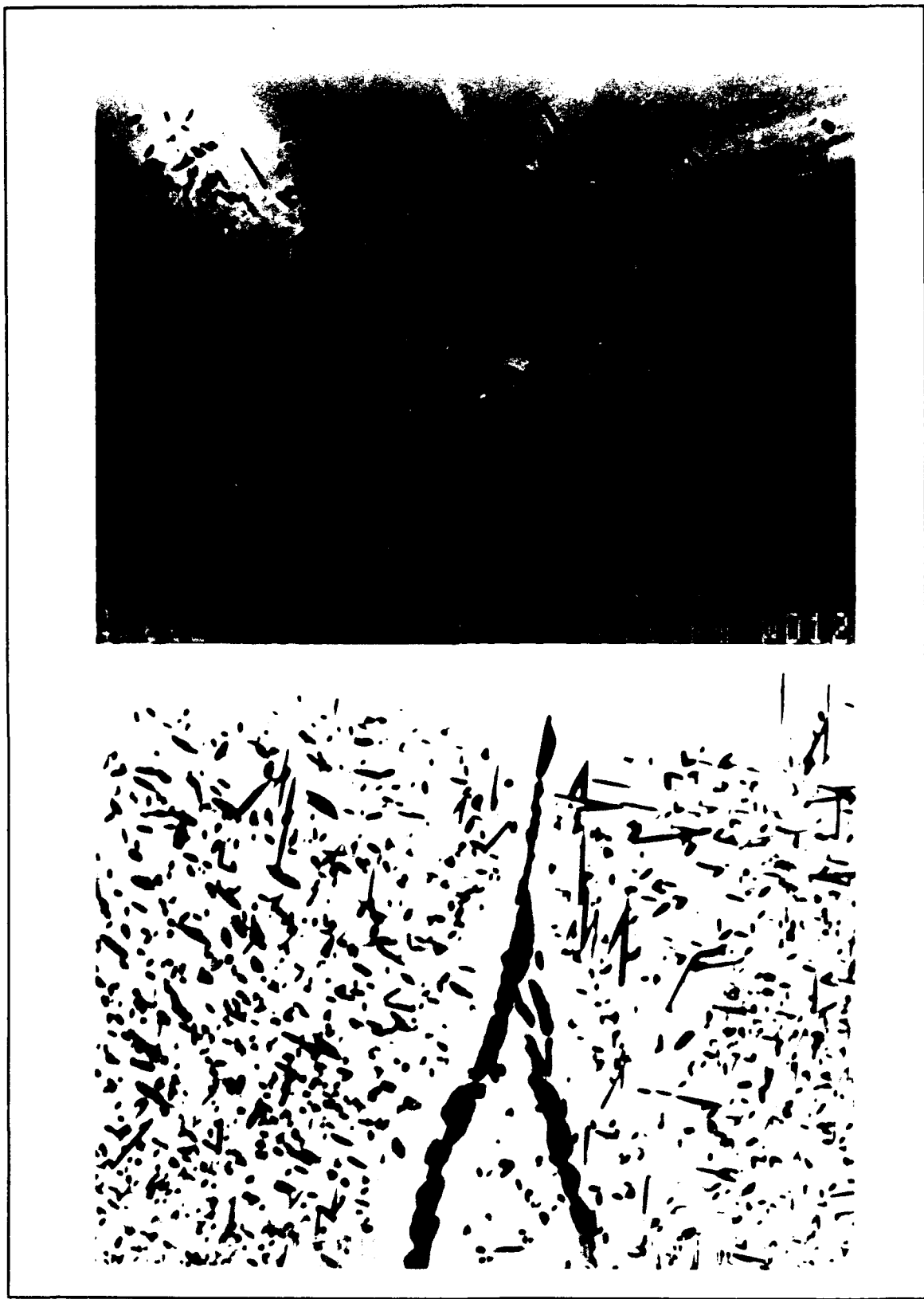


Figure 52. Matrix Microstructure after Heat Treatment (top) and after Thermal Cycling (bottom) (1500x)

V. Discussion and Analysis

The strain and moduli measurements and damage analysis from the five TMF tests provide a picture of the progression to failure for the $[\pm 45]_2$ laminate. The laminate fatigue response is dominated by the fiber-matrix interface and the matrix material. The fibers seem to play only an insignificant role during cycling. Laminate behavior can be divided into three periods during thermomechanical cycling. The first is interface dominated and the other two are matrix dominated. During the early cycles, damage to the interfaces and gross matrix plasticity render the fibers ineffective in carrying the load and the laminate stiffness drastically decreases. The stress can no longer be effectively transferred to the fibers and the matrix becomes the primary load carrying constituent. The inability of the matrix to transfer stress across the interfaces leads to the next two phases of fatigue life characterized wholly by the matrix response. The second phase is a matrix stiffening period when damage begins to accumulate at the interfaces but does not appreciably degrade the matrix. The last period is marked by the damage in the matrix slowly accumulating and coalescing to cause a gradual reduction in failure. This last phase leads to failure.

Before fatigue cycling, the bonds between the fibers and the matrix are assumed perfect and the reaction zone

intact. During the first period of fatigue life, a component of the stress is transferred through the reaction zone to the fiber, as long as the fiber/matrix bond remains intact. When the applied stress exceeds the strength of the bond, the interface fails. The laminate still responds in a linear manner, albeit with reduced stiffness. Continued loading causes non-linear behavior followed by a nearly perfectly plastic region. Unreinforced Ti-15-3 responds in a similar elastic-perfectly plastic manner, while the SCS-6 fibers are elastic until fracture. The near perfectly plastic region in the laminate corresponds to the gross plastic deformations occurring in the matrix during the first cycle. The stress in the matrix surrounding the fibers, very near yield due to the processing residual stresses (19:1), increases rapidly to degrade the reaction zone and deform the matrix around the fiber hole. Upon unloading the laminate responds linearly and the compressive residual stresses are recovered around the fiber. Continued cycling during the first fatigue period further degrades the interface and deforms the matrix around the fiber.

During the early cycles, the reaction zone and fiber-matrix interface are extensively damaged which causes a severe drop in the stiffness as seen in the moduli graphs. Replicas taken during the initial cycles show debonding and matrix deformation around fibers. If excessive plastic deformation occurs due to the applied stress and the fiber-matrix bond fails, fibers in a ply begin to rotate and slide

away from the edge. The fiber rotation appears to be a gradual process which occurs independently in every ply. One ply may show fibers recessing into the laminate after 300 cycles, while an adjacent ply may not fully recess after 1000 cycles. Fibers sliding into the laminate fully illustrate that there is no constraint on the fiber by the interface. Likewise, if there is no physical constraint on the fiber by the matrix, stress transfer between the two is minimal. In such areas where the fibers are ineffective in carrying load, the laminate can be considered as only matrix material with holes. The primary damage impact of the first period is breakdown of the interface and deformation of the matrix around the fibers causing an effective transfer of the load to the matrix.

During the second phase of fatigue life, the laminate is physically a different material than before testing. The matrix is supporting the majority of the load and is severely degraded and deformed at the fiber-matrix interfaces. During this second period, the strain continues to accumulate rapidly but the laminate begins to recover stiffness. This suggests a hardening of the matrix. Simultaneously, the effects of thermal cycling cause enlarging and embrittling of damaged reaction zones. Transverse matrix cracks, as seen from edge replicas, begin to grow radially from these weakened zones. These cracks continue to accumulate and extend across ply boundaries where they coalesce with other radial cracks. It is likely that a similar crack

growth mechanism is responsible for the brittle fatigue growth seen in the middle of fracture surfaces. The transverse matrix cracking grows throughout the laminate from the fiber reaction zones, bridging each ply with cracks. The accumulated damage eventually overcomes the hardening trend of the matrix and a gradual loss of stiffness ensues.

The third phase of the fatigue life is damage dominated. It begins when the accumulated matrix damage impairs the ability of the laminate to support the applied load. The result is a continual drop in stiffness until failure. The accumulation of strain continues at a much slower rate than seen in the second fatigue period. Fatigue cracking appears to start in the middle of the specimen at several initiation sites, coalesces and works out toward the specimen edges and faces. Failure occurs when the fatigue cracking in the middle encompasses a majority of the surface such that the remaining matrix material at the edges and faces cannot support the applied load. The remaining regions then fail due to tensile overload.

Stiffness Analysis

The second period of the fatigue life is characterized by stiffer laminate response to the applied load even though the fiber-matrix interfaces have been degraded. This is an unexpected response to fatigue cycling. The increase in stiffness is even more confusing because it occurs as matrix cracking becomes more prevalent throughout the laminate.

Schubbe reported similar modulus trends during in-phase and out-of-phase TMF tests of a cross ply MMC (26:72). Three potential mechanisms could be affecting the stiffness during testing: fiber rotation, age hardening or work hardening.

Fiber rotation was observed in the isothermal fatigue test and in all of the TMF tests. Among failed specimens, the fiber orientation changed from $[\pm 45]$ to approximately $[\pm 39]$ at the fracture where extensive necking occurred. The TMF test stopped at 21,000 cycles, averaged 2.5 degrees change in fiber orientation. The fiber rotation was due to the failure of the fiber-matrix bond, the large amounts of plastic deformation and a component of the load effectively pulling the fiber toward the loading axis. It can be thought of as a scissoring effect between plies.

The computer program AGLPLY was used to quantify the effect on room temperature initial loading stiffness due to incremental changes in the fiber orientation. This analysis did not attempt to model the plasticity or the dynamics of fibers sliding and rotating in the matrix. Rather, the objective was to examine the magnitude of stiffness change in a perfect laminate due to changing fiber orientation. Though AGLPLY cannot model an interface zone or interface damage, it can be used to accurately measure the ambient stiffness for the laminate used in this study. Lerch and Saltsman (17) achieved excellent agreement between AGLPLY predicted bi-linear stress-strain response and experimental stress-strain response for a $[\pm 45]_2$ SCS-6/Ti-15-3 laminate.

The AGLPLY predicted change in modulus is summarized in Table 7.

Table 7. AGLPLY Predicted Modulus Change		
<u>Fiber Angle (degrees)</u>	<u>Predicted E (GPa)</u>	<u>Percent Change</u>
45	130.1	0
44	131.2	.8
43	132.4	1.8
42	133.7	2.8
41	135.1	3.8
40	136.5	4.9
39	138.0	6.1
38	139.6	7.3

In general, the AGLPLY analysis shows a 6 percent increase in room temperature stiffness for a six degree change in fiber orientation. The average percent change in the initial loading modulus during cycling for all TMF tests is 45 percent. It is probable that fiber rotation does not affect the laminate stiffness since the magnitude of the increase during cycling is much larger than what could be reasonably expected due fiber rotation alone. Further evidence supporting this is found in the 220 MPa test data. During that test the initial loading modulus increased by 46 percent (similar to the other tests), yet the measured fiber rotation was only approximately 2.5 degrees. Since the stiffness is a measure of how the laminate as a whole is responding to the applied loading, the matrix must then account for the stiffening of the laminate. The results

further support the assertion that during the second period of fatigue life, the transfer of stress to the fibers is minimal and that the matrix is carrying the load and, hence, dominating the laminate response. A matrix hardening mechanism is the probable cause of the stiffening laminate response.

Age hardening of as-received Ti-15-3 can result in wide changes in its mechanical properties. Aging causes the more stable α -phase to precipitate from the β -phase. The α -phase is the primary hardening phase of Ti-15-3 and reportedly has a 16 percent higher modulus than β -Ti (15:10). Lerch and others have investigated in detail the effects of various heat treatments on the SCS-6/Ti-15-3 system (15). Their results suggested that exposure of the material to a temperature that is different than the aging temperature causes some change in the microstructure and the mechanical properties (15:8). All specimens in this study were aged at 700 C in vacuum for 24 hours and tested over a 149 C to 427 C temperature range. It is possible, then, that further precipitation of the α -phase during testing could result in a change in the matrix stiffness. Lerch and others noted, however, that aging of the matrix in vacuum at 700 C for 24 hours resulted in an overaged structure (15:3). In addition, the SEM backscatter analysis performed in this study did not reveal any noticeable differences between the microstructure of an aged specimen and a thermally fatigued specimen. It is probable, then, that TMF testing in air over

the temperature range used in this study did not alter the microstructure of the matrix to cause a dramatic increase in stiffness.

Work hardening in a metal can result in changes to its physical and mechanical properties. Plastic deformation in a metal occurring at temperatures low relative to its melting point is known as cold working. Cold working increases the strength and hardness of a material due to elongation of its grains. Since extreme plastic deformations occur over a temperature range much lower than the matrix melting point, cyclic cold working is a plausible factor in explaining the rise in laminate stiffness. The cold working phenomenon is a function of both the applied stress and temperature. Schubbe also noted the possible role of cold working in explaining modulus increase.

The stiffness increase during the 400 MPa, 350 MPa and 320 MPa test generally occurred over the first 1000-2000 cycles which would indicate a dependence on the time at temperature during testing. The 220 MPa test, however, experienced a similar stiffness increase over the first 7500 cycles. There also seems to be little correlation between the strains at which the stiffness increase occurred. For the 400 MPa test, the stiffness increase occurred between seven and eleven percent, while the stiffness increase for the 220 MPa test occurred between .5 and 1.9 percent. There appears to be no consistent common factor for predicting the duration or magnitude of the increase in stiffness or an

obvious explanation of its cause. Work hardening, though, in the form of cold working of the matrix may significantly contribute to the overall increase in the laminate stiffness.

Fatigue Life

Figure 53 presents the stress range versus cycles to failure data generated by this study compared to similar data for isothermal fatigue at 427 C of an identical laminate reported by Lerch (14). In general, in-phase thermomechanical fatigue should show a shorter fatigue life for a given stress range than isothermal fatigue due to the additional strains caused by thermal cycling. Figure 53 displays such a trend for high stress ranges but not in the middle to low stress ranges. The difference in test cycle frequencies may explain the crossover in the lower stress ranges.

Prediction of fatigue life for composite materials can be very difficult. Residual strength degradation and modulus degradation approaches have recently been used in an attempt to predict fatigue life of composites (27:1). The moduli data generated by this study are difficult to explain and seemingly impossible to predict. Hence, the moduli as obtained from the cycle stress-strain curves do not appear to be useful as a parameter in reliably predicting fatigue life for the $[\pm 45]$ layup. Schubbe attempted to use the secant modulus as a damage parameter in a cumulative damage model to predict TMF life of a $[0/90]_2$, SCS-6/Ti-15-3

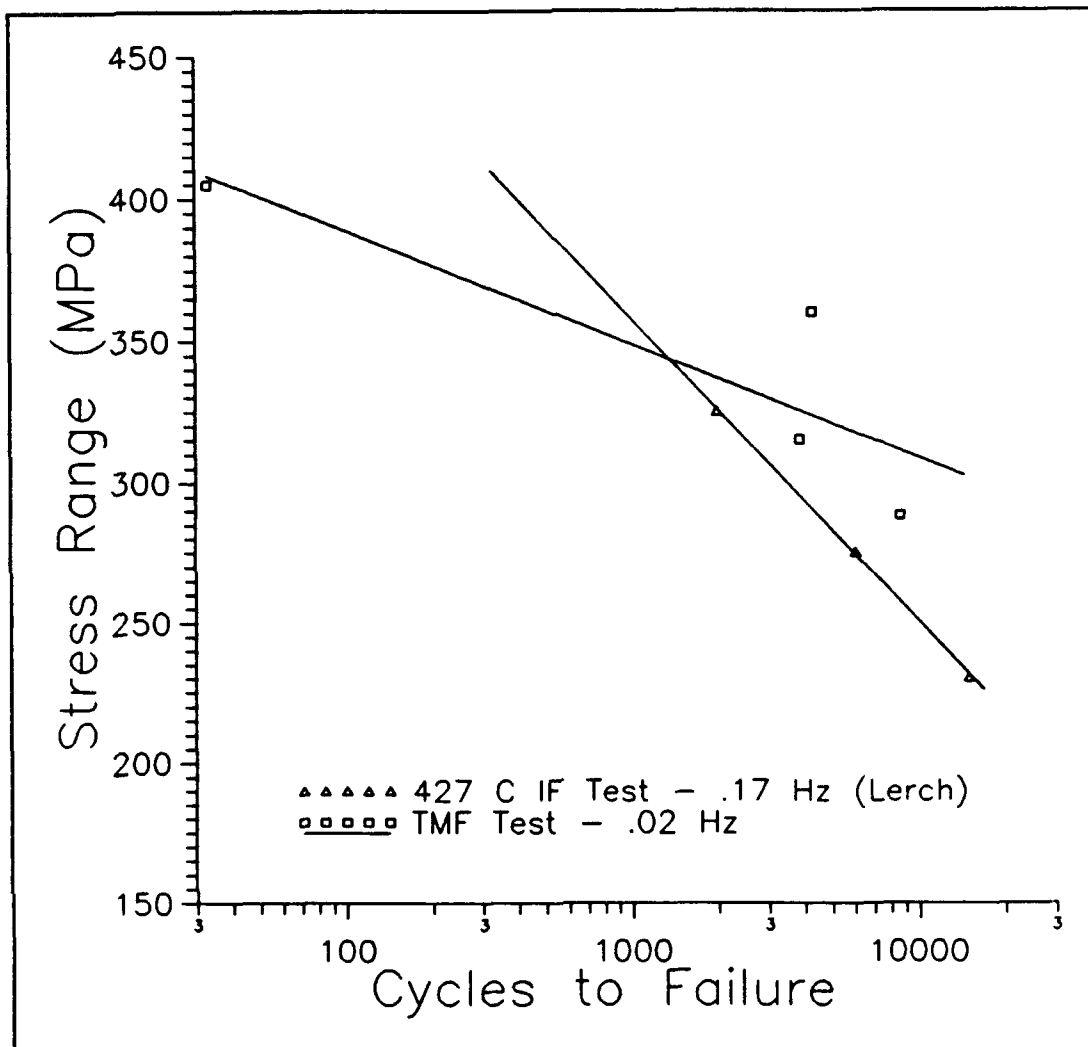


Figure 51. Fatigue Life Comparison between TMF Test and IF Test

laminate (26:109). Reasonable damage curves were obtained by not considering the work hardening period of the fatigue life. This work hardening period, though, may have an important impact on the fatigue life during thermomechanical cycling for metal matrix composites, especially for laminates containing plies oriented other than 0 and 90 degrees. The complex behavior exhibited by SCS-6/Ti-15-3 laminates

during TMF testing makes accurate fatigue life predictions impossible without further understanding all mechanisms involved.

VI. Conclusions and Recommendations

This study investigated the TMF response of an angle ply $[\pm 45]_{2s}$ SCS-6/Ti-15-3 metal matrix composite. A computer-controlled test system was used to record stress and strain data during in-phase TMF testing. Three separate cycle loading moduli were calculated to describe the laminate fatigue response and to quantify the laminate damage.

Conclusions that can be drawn from the results of this study are summarized below.

1) The current TMF test system and software proved capable of conducting accurate and well-controlled in-phase TMF tests.

2) Replicating during testing quantified progressive edge damage, but did not necessarily indicate the extent of internal fatigue damage.

3) Edge replicating revealed debonding and deformation of the matrix around the fiber-matrix interface, reaction zone growth, transverse matrix cracking in the matrix originating at the damaged reaction zone and fiber sliding in the matrix which indicated total failure of the interface and fiber rotation.

4) All specimens exhibited open stress and strain hysteresis throughout testing and ratcheted to failure.

5) Total failure strains were found to be proportional to the maximum applied cycle stress.

6) Internal transverse matrix cracking originating at damaged reaction zones was the primary mechanism of fatigue damage growth in all specimens.

7) Fatigue behavior during all tests was dominated by the matrix material response; fibers played only an insignificant role in laminate fatigue response.

8) Three phases of fatigue life were identified: 1) a fiber-matrix interface damage phase, 2) a matrix hardening phase and 3) a matrix damage phase.

9) Matrix hardening was thought to be caused by cold working of the matrix during the second phase of fatigue life. Additional α -precipitation in the matrix during testing also may contribute to the hardening effect.

10) The calculated moduli could not be used as a consistent damage parameter to predict fatigue life since it did not consistently and accurately describe the damage accumulated during fatigue life.

Recommendations for future efforts are summarized below.

1) The active air cooling system should be modified to eliminate the initial steep cooling slope and the test software should be updated to acquire data continuously during the first ten test cycles.

2) Complete isothermal fatigue and out-of-phase TMF tests over the same temperature range and cycle frequency should be conducted to fully characterize the fatigue response of the $[\pm 45]$ angle ply laminate.

3) TMF investigations of unreinforced Ti-15-3 should be conducted to further understand the dominant role of the matrix and to isolate the matrix hardening mechanisms.

4) Further investigations to study the causes and effects of fiber rotation during testing should be conducted using non-destructive testing techniques.

Appendix A: Logarithmic Modulii Plots

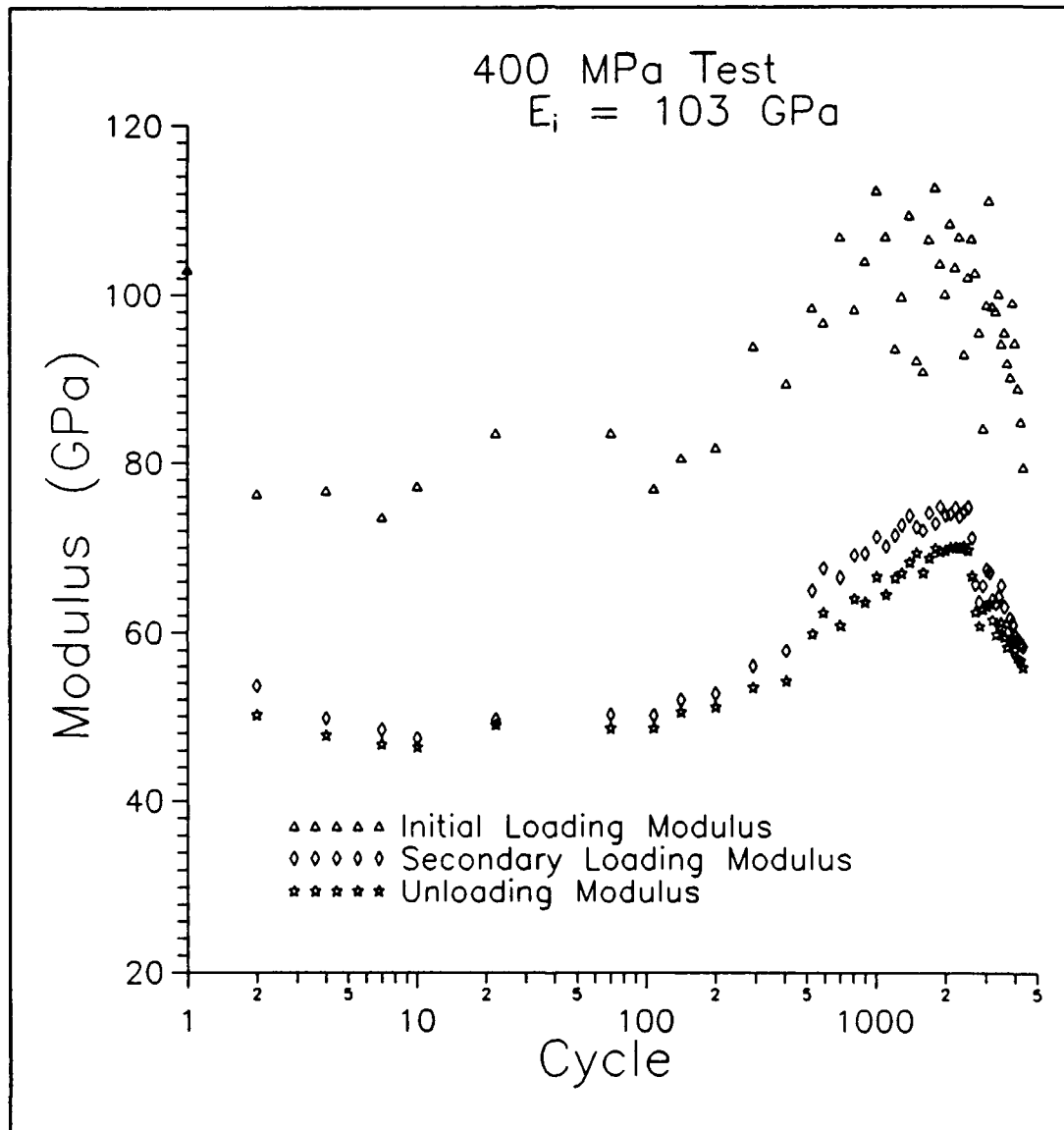


Figure 54. Modulii with Logarithmic Cycle Axis for 400 MPa Test

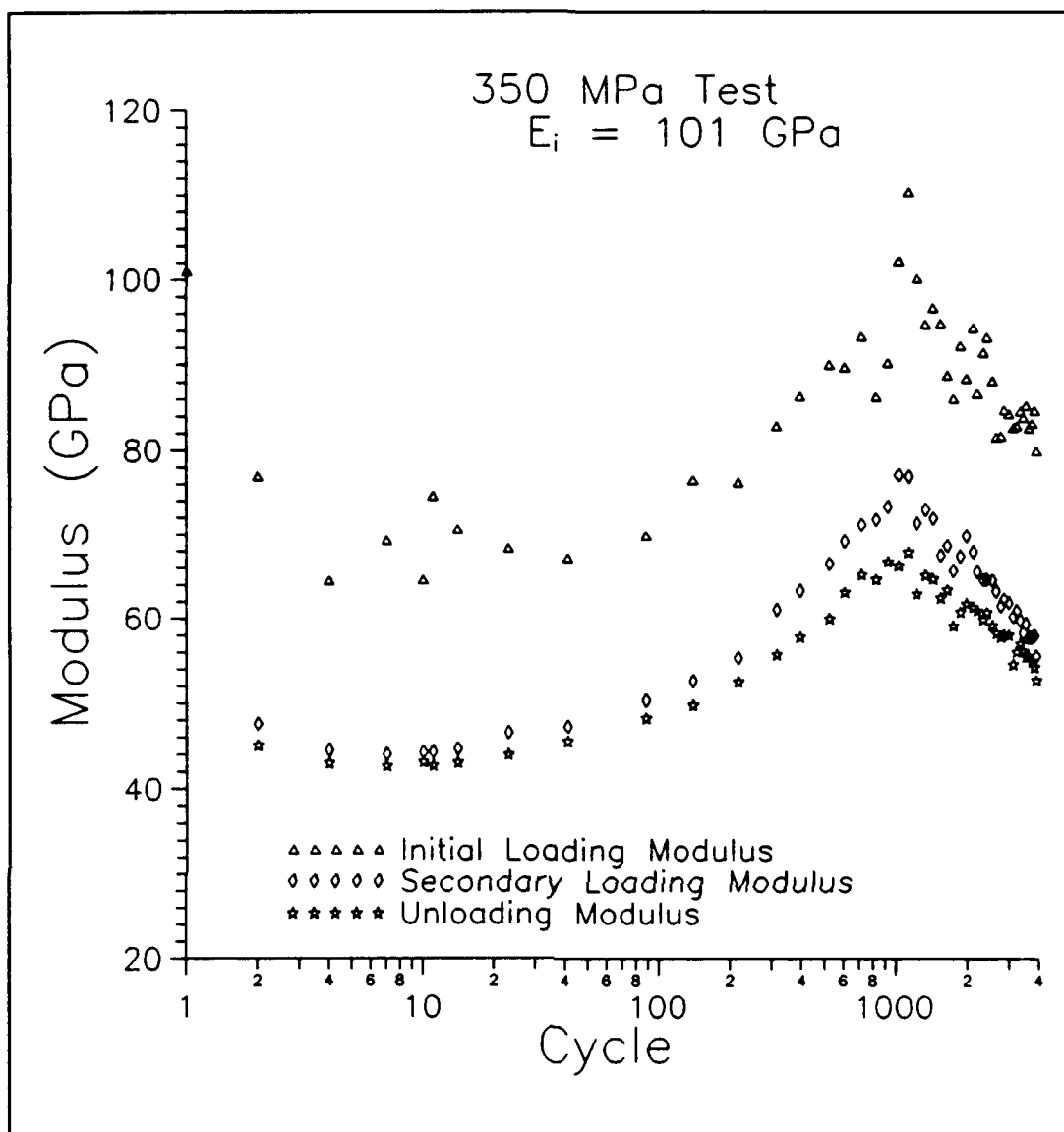


Figure 55. Moduli with Logarithmic Cycle Axis for 350 MPa Test

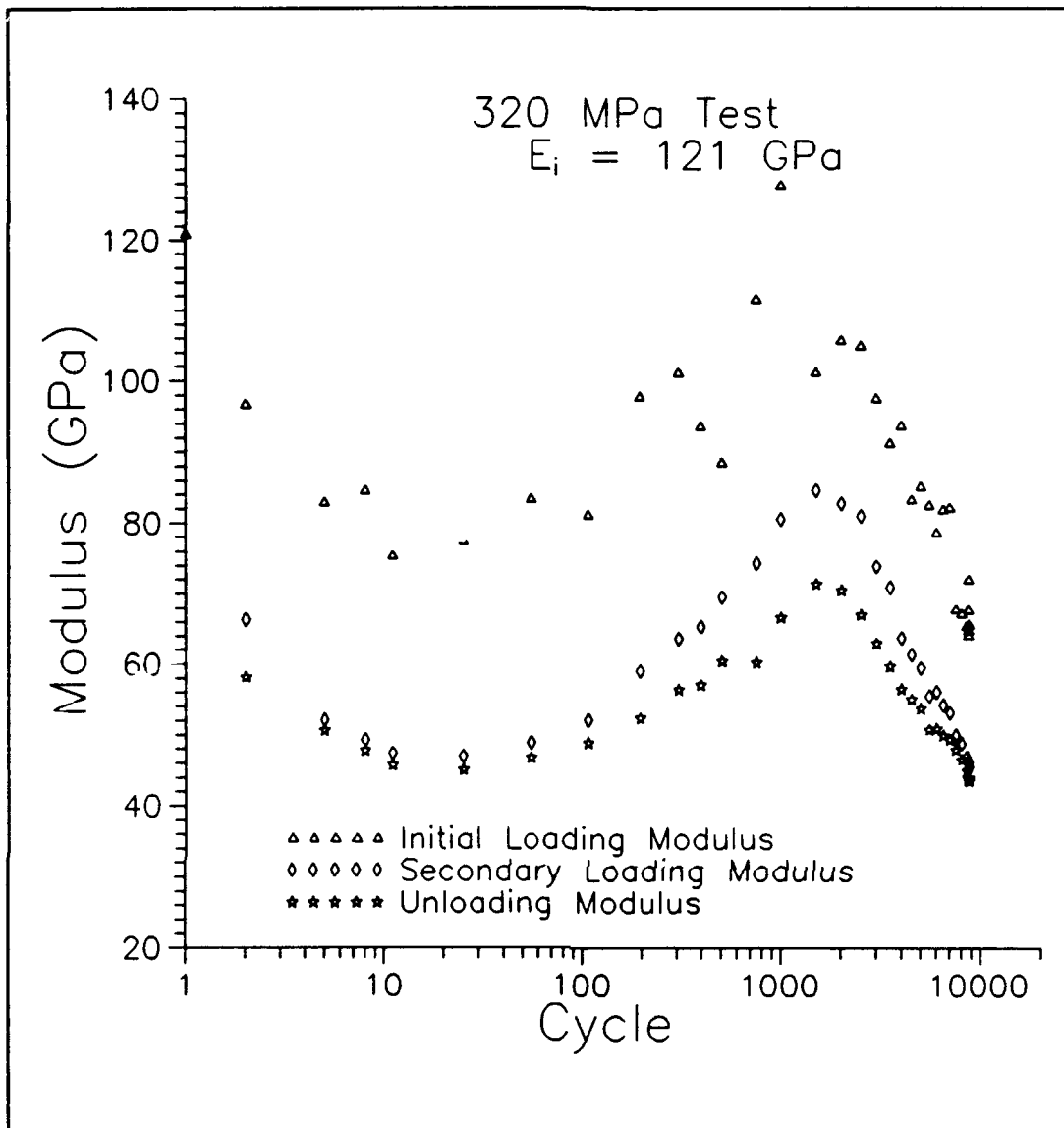


Figure 56. Moduli with Logarithmic Cycle Axis for 320 MPa Test

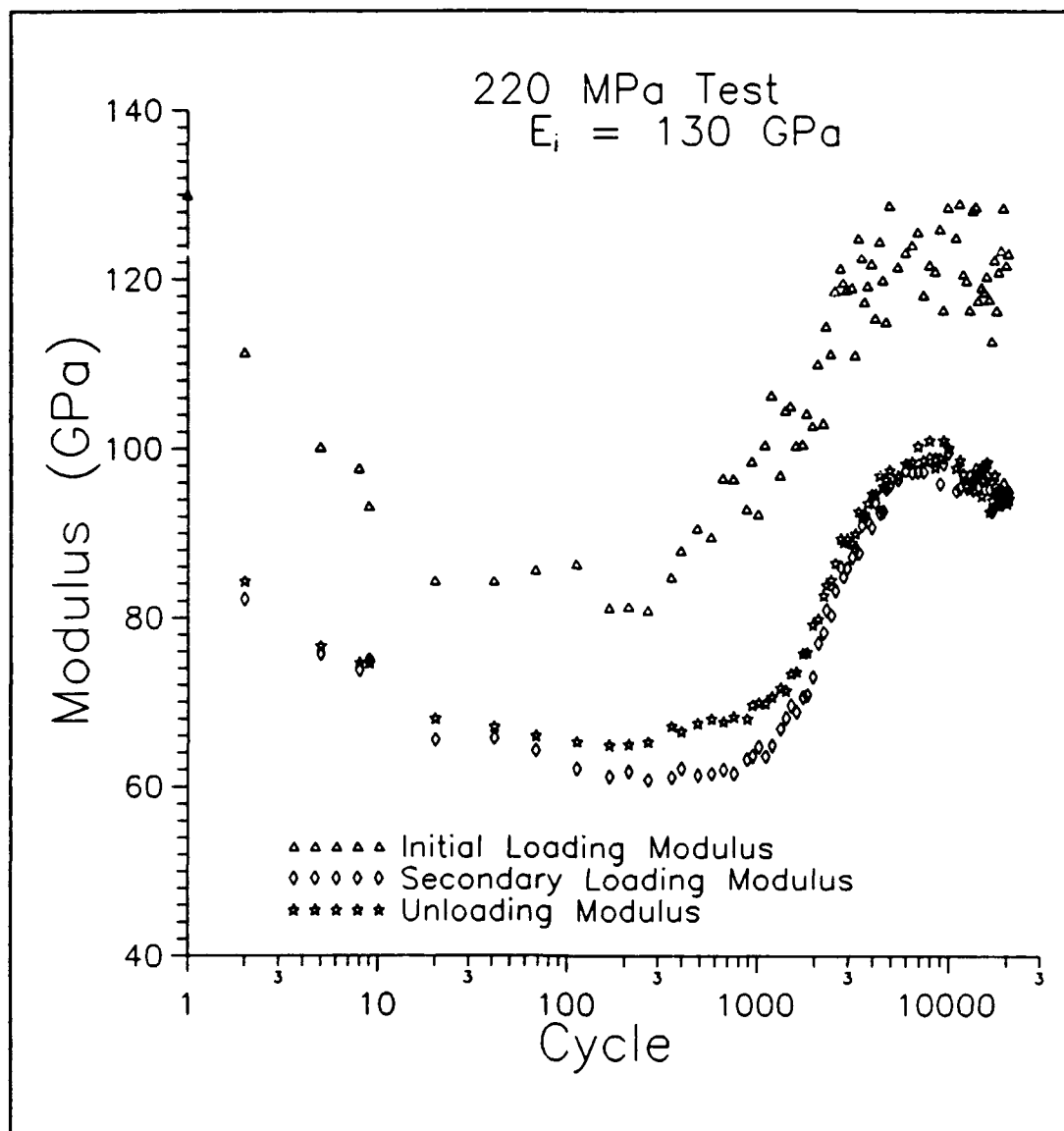


Figure 57. Moduli with Logarithmic Cycle Axis for 220 MPa Test

Appendix B: WDS Analysis

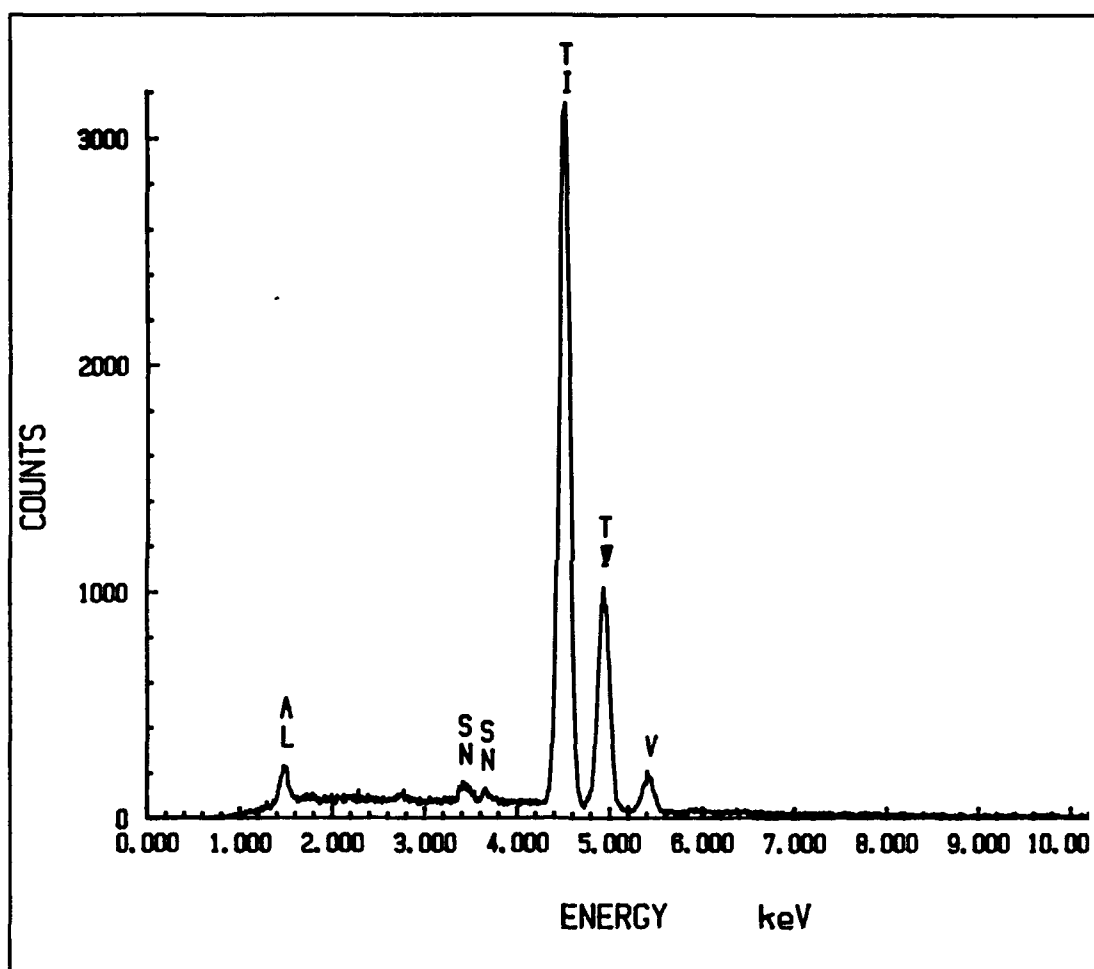


Figure 58. WDS Analysis of Uncycled Ti-15-3

Bibliography

1. Bigelow, C.A. and others. "A Comparison of Various Micro-mechanics Models for Metal Matrix Composites," Mechanics of Composite Materials and Structures, edited by J.N. Reddy and J.L. Teply, American Society of Mechanical Engineers, H00464:21-23 (1989).
2. Castelli, M.G. and others. "Thermomechanical Testing Techniques of High Temperature Composites: TMF Behavior of SiC (SCS-6)/Ti-15-3," NASA TM-103171, August, 1990.
3. Ermer, Captain Paul G. Investigation of the Failure Modes in a Metal Matrix Composite Under Thermal Cycling. MS Thesis, AFIT/GAE/ENY/89D-07. School of Engineering, Air Force Institute of Technology (AU), Wright-Patterson AFB, OH, December 1989.
4. Gayda, J. and others. "The Effect of Environment on the Fatigue Life of SiC/Ti-15-3 Composite." Presented at Thermomechanical Fatigue Workshop, NASA Lewis Research Center, Cleveland, OH, June 5, 1991.
5. ----- and T.P. Gabb. "Effect of Heating Mode and Specimen Geometry on Fatigue Properties of a Metal Matrix Composite," NASA Lewis Research Center, Cleveland, OH, Unpublished.
6. Grady, J.E. and B.A. Lerch. "Evaluation of Thermomechanical Damage in SiC/Titanium Composites," NASA Lewis Research Center, Cleveland, OH, Unpublished.
7. Halford, G.R. "Low-Cycle Thermal Fatigue" NASA TM-87225, February, 1986.
8. Johnson, W.S. and others. "Fatigue Damage Growth Mechanisms in Continuous Fiber Reinforced Titanium Matrix Composites," NASA TM-102594, January, 1990.
9. Johnson, W.S. "Fatigue Testing and Damage Development in Continuous Fiber Reinforced Metal Matrix Composites," NASA TM-100628, June, 1988.
10. ----- and others. "Mechanical Characterization of Unnotched SCS₆/Ti-15-3 Metal Matrix Composites at Room Temperature," NASP TM-1014, April, 1988.

11. Khobaib, M. "Creep Behavior of SCS-6/Ti-24Al-11Nb Composite." Proceedings from Titanium Aluminide Composite Workshop, Orlando, FL, May 1990. Titanium Aluminide Composites, edited by P.R. Smith and others. WL-TR-91-4020, Wright-Patterson AFB, OH. 450-466. February, 1991.
12. Kortyna, B.R. and N.E. Ashbaugh. "Fatigue Characteristics of a Titanium Aluminide Composite." Proceedings from Titanium Aluminide Composite Workshop, Orlando, FL, May 1990. Titanium Aluminide Composites, edited by P.R. Smith and others. WL-TR-91-4020, Wright-Patterson AFB, OH. 467-483. February, 1991.
13. Lerch, B.A. and D.R. Hull. "As-Received Microstructure of a SiC/Ti-15-3 Composite," NASA TM-100938, August, 1988.
14. Lerch, B.A. "Fatigue Behavior of SiC/Ti-15-3 Laminates," NASA Lewis Research Center, Cleveland, OH, Unpublished.
15. ----- and others. "Heat Treatment Study of the SiC/Ti-15-3 Composite System," NASA TP-2970, January, 1990.
16. Lerch, B.A. "Matrix Plasticity in SiC/Ti-15-3 Composite," NASA Lewis Research Center, Cleveland, OH, Unpublished.
17. ----- and J.F. Saltsman. "Tensile Deformation in SiC Reinforced Ti-15V-3Cr-3Al-3Sn." NASA TM-103620, April, 1991.
18. MacKay, R.A. "Effect of Fiber Spacing on Interfacial Damage in a Metal Matrix Composite," Scripta Metall. et Mater., 24:167-172 (1990).
19. Majumdar, B.S. and G.M. Newaz. "Inelastic Deformation of Metal Matrix Composites: Plasticity and Damage Mechanisms," Battelle Memorial Institute, Columbus, OH. Submitted to Philosophical Magazine, June, 1991.
20. ----- . "Thermomechanical Fatigue Response and Damage in an Angle-Ply Metal Matrix Composite," Battelle Memorial Institute, Columbus, OH. Submitted to The Journal of Engineering Materials and Technology - ASME, October, 1989.
21. Mirdamadi, M. and others. "Analysis of Thermomechanical Fatigue of Unidirectional Titanium Metal Matrix Composites," NASA Langley Research Center, Hampton, VA, Unpublished. Presented at Thermomechanical Fatigue Workshop, NASA Lewis Research Center, Cleveland, OH, June 5, 1991.

22. Newaz, G. M. and B.S. Majumdar. "Deformation and Failure Mechanisms in Metal Matrix Composites," Battelle Memorial Institute, Columbus, OH. Presented at ASME Winter Annual Meeting, Atlanta, GA, December 1991.
23. Revelos, W.C. and P.R. Smith. "Effect of Environment on the Thermal Fatigue Response of a Ti-24Al-11Nb/SCS-6 Composite." Proceedings from Titanium Aluminide Composite Workshop, Orlando, FL, May 1990. Titanium Aluminide Composites, edited by P.R. Smith and others. WL-TR-91-4020, Wright-Patterson AFB, OH. 399-415. February, 1991.
24. Rogacki, J. and M. Tuttle. "Thermoviscoplastic Behavior of SCS₆/Ti Metal Matrix Composites," University of Washington, Seattle, WA, Unpublished.
25. Russ, S.M. and T. Nicholas. "Thermal and Mechanical Fatigue of Titanium Aluminide Metal Matrix Composites." Proceedings from Titanium Aluminide Composite Workshop, Orlando, FL, May 1990. Titanium Aluminide Composites, edited by P.R. Smith and others. WL-TR-91-4020, Wright-Patterson AFB, OH. 431-449. February 1991.
26. Schubbe, Captain Joel J. Investigation of Damage Mechanisms in a Cross-Ply Metal Matrix Composite Under Thermo-Mechanical Loading. MS Thesis, AFIT/GAE/ENY/90D-26. School of Engineering, Air Force Institute of Technology (AU), Wright-Patterson AFB OH, December, 1990.
27. WoonBong Hwang and K.S. Han. "Fatigue of Composite Materials - Damage Model and Life Prediction," Composite Materials: Fatigue and Fracture, Second Volume ASTM STP 1012: 87-102.

REPORT DOCUMENTATION PAGE			Form Approved OMB No. 0704-0188	
Public reporting burden for this collection of information is estimated to average 1 hour per response, including the time for reviewing instructions, searching existing data sources, gathering and maintaining the data needed, and completing and reviewing the collection of information. Send comments regarding this burden estimate or any other aspect of this collection of information, including suggestions for reducing this burden, to Washington Headquarters Services, Directorate for Information Operations and Reports, 1215 Jefferson Davis Highway, Suite 1204, Arlington, VA 22202-4302, and to the Office of Management and Budget, Paperwork Reduction Project (0704-0188), Washington, DC 20503.				
1. AGENCY USE ONLY (Leave blank)	2. REPORT DATE DEC 91	3. REPORT TYPE AND DATES COVERED Master's Thesis		
4. TITLE AND SUBTITLE Thermomechanical Fatigue Characterization of an Angle Ply Metal Matrix Composite		5. FUNDING NUMBERS		
6. AUTHOR(S) Wade H. Vaught, 1st Lt., USAF				
7. PERFORMING ORGANIZATION NAME(S) AND ADDRESS(ES) Air Force Institute of Technology, WPAFB OH 45433-6583		8. PERFORMING ORGANIZATION REPORT NUMBER AFIT/GAE/ENY/91D-21		
9. SPONSORING / MONITORING AGENCY NAME(S) AND ADDRESS(ES) Ted Fecke W/L HE /POTC Wright-Patterson AFB OH 45433		10. SPONSORING / MONITORING AGENCY REPORT NUMBER		
11. SUPPLEMENTARY NOTES				
12a. DISTRIBUTION / AVAILABILITY STATEMENT APPROVED FOR PUBLIC RELEASE; DISTRIBUTION UNLIMITED [+ - - 45](25)		12b. DISTRIBUTION CODE		
13. ABSTRACT (Maximum 200 words) An investigation was conducted to study the thermomechanical fatigue (TMF) response of a [± 45] _{2s} angle ply SCS-6/Ti-15-3 metal matrix composite (MMC). Load controlled in-phase TMF experiments were performed over the temperature range 149-427 C, with a cycle frequency of 1.02 Hz. Test equipment included a high temperature extensometer, quartz lamp radiative heaters controlled by a Micricon thermal control unit and TMF test control software, MATE263. Stress and strain hysteresis, total strain and stiffness were monitored to characterize material behavior. Large plastic deformations were observed in all specimens, with total failure strains ranging from 7 to 13 percent. It was observed that the total strain to failure was proportional to the maximum applied cycle stress. Damage mechanisms, studied using edge replication and optical and scanning electron microscopy, showed transverse microcracks originating at the fiber-matrix interface and slip bands and fiber sliding in the matrix. Three phases during fatigue life were observed in the tested specimens: (1) interface damage; (2) matrix hardening; and (3) matrix damage. Cold working of the matrix was a probable factor in the matrix hardening. The fibers did not affect the fatigue behavior which was dominated by matrix response.				
14. SUBJECT TERMS Metal Matrix Composites, Fiber-Reinforced Composites, SCS/Ti-15-3, Silicon Carbide, Titanium, Thermomechanical Fatigue, Heat Resistant Materials, Composite Materials			15. NUMBER OF PAGES 131	
			16. PRICE CODE	
17. SECURITY CLASSIFICATION OF REPORT Unclassified	18. SECURITY CLASSIFICATION OF THIS PAGE Unclassified	19. SECURITY CLASSIFICATION OF ABSTRACT Unclassified	20. LIMITATION OF ABSTRACT UL	